DESIGN, FABRICATION AND EXPERIMENTAL CHARACTERIZATION OF A PDMS-BASED AWG SPECTROMETER

KEE JACK SHENG

School of Electrical & Electronic Engineering

A thesis submitted to the Nanyang Technological University
in fulfillment of the requirement for the degree of
Doctor of Philosophy

2011

ACKNOWLEDGEMENT

Firstly, I would like to thank Assoc. Prof. Daniel Puiu Poenar for being a helpful research supervisor. He made my postgraduate studies enjoyable with many learning opportunities. He has also provided me with lots of academic guidance and direction during the course of my studies. One of the important things that he has taught me is research project management. He insisted that careful planning and timely execution is necessary to achieve the goals of the research. These management skills are very useful more than the scientific knowledge and skills learned during the studies.

I would like to thank Dr. Levent Yobaş for being my co-supervisor. He has trained me to be persistent and diligent in pursuing research. He has also taught me about professionalism in presenting my work, in both writing and oral presentation with clarity and truth. I am indebted to Dr. Pavel Neužil who has been very helpful in my experimental works. He has provided me with useful advice and practical solutions to overcome various issues and problems. I would also like to thank Dr. Chen Yu for providing me with the necessary assistance to complete my project.

My research has been more enjoyable and productive with lab mates, Wong Chee Chung, Chaitanya Kantak, Jeffrey Soon and Ong Wee Liat. Having these fine researchers work with me led to many valuable discussions and assistance in necessary work.

I am grateful to the staffs of Institute of Microelectronics, Agency for Science and Technology Singapore. The staffs from SPT Cleanroom 2 have

assisted me in the fabrication of the SU-8 master mold and also the staff from MEMS lab for helping me with the optical setup and characterization. The staffs in Photonics Labs and Microelectronics center has extended their assistance for usage of equipments, instruments and the necessary software for simulations.

And last but not least I would like to thank my family for supporting and encouraging me of my endeavours. I am very grateful to my wife, Elaine for her love and support throughout my graduate studies.

TABLE OF CONTENT

SUMMARY

Conventional spectroscopy used in the life sciences and analytical chemistry is performed by spectrophotometer – bench top equipment which is expensive, bulky and demanding large volume of sample and reagents. Miniaturization of spectrometer and sample preparation cuvette calls for a micro-total-analysis system (μTAS) or lab-on-a-chip (LOC) which integrates spectrometer capabilities and microfluidics into a single platform. Such LOC can benefit from various optical microcomponents capable of focusing, dispersing, guiding light to the desired point in order to achieve a highly sensitive and robust spectroscopy measurement at a low cost as well as reducing reagent usage. Poly(dimethylsiloxane) (PDMS) has been widely used for the fabrication of microfluidics and LOC devices due to unique characteristic such as biocompatibility, low cost, and rapid prototyping capability by soft lithography.

In this thesis, PDMS-based AWG microspectrometer for LOC application was demonstrated by foremost developing planar waveguide in PDMS material. The development of planar waveguide focused primarily in design and fabrication of novel PDMS waveguide with single-mode propagation as the basic building block for complex devices. By selecting the appropriate geometrical parameters, single-mode propagation can be generated even in a large cross section PDMS rib waveguide (> 5 μm). The fabrication of PDMS single-mode waveguide involved precise controlled of the slab and rib height to the accuracy of ±0.1 μm as well as the modification of the refractive index from 1.408 to 1.429. The characterization

of the PDMS waveguide corroborated single-mode propagation at the wavelength of 635 nm with the propagation loss measured to be 0.48 dB/cm for low refractive index contrast waveguides (Δ=0.07%) and 0.2 dB/cm for high refractive index contrast waveguides (Δ=1.18%).

Based on the proven PDMS single-mode waveguide, the PDMS AWG was designed and implemented as the wavelength dispersive element for operation in the visible light (400–700 nm). Such visible light PDMS AWG is essential because a large portion of the spectroscopical signature lies in this range. Two types of PDMS AWG were designed to meet the requirements of high resolution and large *FSR* for a microspectrometer. The first conventional PDMS AWG has been designed and met the desired resolution of 1 nm. The second non-conventional PDMS AWG with an S-shaped arrayed waveguides has been realized with an *FSR* of 275 nm. Both types of AWG were fabricated and tested for transmission loss, polarization dependency, channel uniformity and channel crosstalk. The conventional PDMS AWG has shown an insertion loss of 11.4 dB at 641 nm transmission peak and adjacent crosstalk of > 15dB with channel loss uniformity well within 0.6 dB.

The integration of these PDMS microphotonic devices with microfluidic was further investigated. Various sensing configurations which comprised of curved waveguide with microfluidic, multi-total internal reflection (MTIR) and evanescent wave sensing for the improvement of the absorption spectroscopy were proposed and examined. The sensitivity has been increased from 1.14×10^{-3} to 2.36

$\times 10^{-3}$ AU/μM by curved waveguides which reduced the stray light and increased by 18 times with MTIR.

In conclusion, the design, fabrication and experiment of PDMS-based AWG spectrometer consist of three main sections which are PDMS single-mode waveguide, PDMS-based AWG and integration of waveguide with microfluidic. Such monolithic integration of PDMS-based planar waveguide devices and microfluidics for spectroscopy facilitates the development of low cost, robust and portable system for LOC spectroscopy application.

LIST OF FIGURES

LIST OF TABLES

CHAPTER 1

INTRODUCTION

1.1 Motivation

Optical spectroscopy involves qualitative and quantitative analytical methods based on the interaction of light with matters which includes living organism and non-living matter. It has been widely used in science, industry, medicine and predominantly in chemistry and biology because it is highly specific and able to both distinguish a substance from its spectral characteristic and determine its concentration.

The advantages of optical spectroscopy are as follows [1]:

1. It is label-free, non-destructive and non-invasive.
2. It is equally applicable to transparent, turbid and opaque samples of liquids, solids, and gases.
3. Remote sensing is possible. Spectroscopy easily measures hazardous and inaccessible samples because it does not need to come into contact with the sample.
4. Fast reactions can be measured with ultrafast laser spectroscopy which reveals the kinetic properties of the processes.
5. Infinitesimal amount of samples in low concentrations can be detected using a highly sensitive detector such as single photon counting devices.
6. Radioactive markers for the investigation of biochemical and molecular processes can be replaced by luminescence markers which are cheaper and easy to use and no posing radiation hazards.

In life sciences and analytical chemistry, spectroscopy is an important tool for clinical, pharmaceutical and health monitoring applications. Recent advances of spectroscopy have found clinical and pre-clinical applications to measure tissue properties for diagnosis and prognosis of various cancers [2]. The optical spectra measured from the tissue reveal the information of vascular volume, oxygenation, extracellular matrix extent, metabolic redox states, and cellular proliferation in cancer cells. In pharmaceutical analysis, large sample populations have to be analyzed in a short amount of time for the discovery of new drugs and quality control of drugs in production. Together with flow injection, spectroscopy has found important roles for the rapid determination of active pharmaceutical ingredients in an automated environment [3]. The advancement of micro-nano-fabrication techniques which can also be used to implement optical components together with other structures to perform various on-chip analytical functions has led to the development of more non-invasive portable sensors for monitoring micronutrients (iron, vitamin A, iodine and folate) and substances (environmental hazards, e.g. lead) critical for overall health assessment [4]. Such sensor systems have the potential to improve significantly the quality of life for patients, such as monitoring of glucose level of diabetic patients.

The first commercialized UV-visible spectrophotometer, optical spectrometer or in short, spectrometer was introduced in 1941 by Cary and Beckman and was given the name Beckman DU [5]. It was originally invented to measure vitamins A & D from various sources [6]. Today, every UV-visible spectrometer can trace its origin to the Beckman DU. Conventional UV-visible spectrometers are bench-top machines which are expensive, bulky and limited

to usage in the laboratory. For the past two decades, there have been massive efforts to miniaturize the components in the optical spectrometer system to bring about smaller size, light weight and result in portable miniature spectrometers for many applications, including in life sciences and chemistry [7]. The products realized by the company "Ocean Optics" are one of the best known examples in this respect [8].

The quest of further shrinking the spectrometer has led to the miniaturization of lenses, gratings, mirrors and prisms to micrometer size to achieve a microchip-based spectrometer, i.e. a microspectrometer [9, 10]. Such a microspectrometer has the benefits of reducing sample volume, providing a higher degree of integration for automation, shortening the response time to improve analytical performance, improving laboratory safety and lowering cost [11]. The monolithic integration of the microspectrometer with components for sample preparation and manipulation calls for the integration of both microfluidics and optical microcomponents (i.e. wavelength discriminating and focusing) into a single lab-on-a-chip (LOC) platform [12]. LOC microsystems are only one category of the larger set of so-called micro total analysis systems (μTAS), that benefit from integrating both the microfluidics components [13] as well as the optical microcomponents onto the same platform, sometimes together with electronic and mechanic components [14]. In addition, LOCs are built upon the technologies developed over the years from microfabrication and bonding techniques in the well-established microelectronics field.

Microfluidics offers a number of capabilities for liquid sample processing. Due to the smaller scales involved, it enables the use small quantities of sample and reagents, and to perform separation and detection with high resolution and

sensitivity, rapid analysis, low cost and small footprints for the devices [15]. Earlier microfluidic realisations were fabricated using silicon because of the thriving silicon microelectronics and microelectromechanical systems (MEMS) technologies. However, it is usually unnecessary or inappropriate to use silicon because silicon is expensive compared to much cheaper alternatives that are suitable for implementation of microfluidics, such as polymers. Moreover, silicon is not an optimal material to realize (micro)optical components for the visible and ultraviolet light since it is opaque for these wavelengths. For example, microfluidic devices have been carried out in a polymer – poly(dimethylsiloxane) (PDMS) which has a different sets of properties from silicon [16]. PDMS is optically transparent, elastic, flexible surface chemistry, low permeability to water, and low electrical conductivity [17]. A myriad of microfluidic components has been demonstrated in PDMS such as a passive chaotic mixer, pneumatically actuated switches and valves, magnetic filter, and functional membranes [18].

Cost reduction, ease of prototyping and increased integration capability in a single PDMS chip have also motivated the demonstration of a range of microoptical components such as microlenses [19], gratings [20], prism [21], dye-doped long pass filters [22] and other elements for optical detection in a LOC platform [23]. In addition, simple PDMS waveguides have exhibited efficient light focusing and guiding to achieve a highly sensitive and robust detection at a low cost [24]. However, none of these PDMS optical microcomponents have the wavelength discrimination capabilities and often require the addition of either off-chip filters or a spectrometer for spectroscopic detection. Therefore, the complete monolithic integration of a spectrometer

together with microfluidics in PDMS promises to provide both the spectroscopic analytical capabilities and sample handling microfluidics at a low cost and with an easy fabrication.

1.2 Objectives

The main objective of this thesis is to realize a PDMS-based microspectrometer which would be used later as a component of future LOC microsystems for absorption spectroscopy applications in the visible light range. The focus of this work can be categorized into three broad areas: the advancement of PDMS planar waveguide technology as the basic building block for complex microoptical components, the realization of PDMS wavelength discrimination components and the investigation of microoptical components integrated with microfluidics for subsequent enhanced detection performance. The detailed goals resulted from or associated with the main objective are listed below:

- To examine theoretically the structure and optical performances of PDMS waveguides in terms of mode propagation, various losses, dependence of their performance on material and geometrical parameters for planar waveguide technology.
- To design single-mode PDMS rib waveguides as a basic building block for complex microphotonics devices.
- To explore unprecedented PDMS fabrication techniques for the construction of single-mode and multi-mode waveguides with improved optical performance as well as complicated shapes and geometry.
- To demonstrate a single-mode PDMS rib waveguide as the basic structure for building complex microphotonics devices such as Y-branch power splitter and arrayed waveguide grating (AWG).

- To study the principles of the AWG and its efficiency when implemented as a PDMS-based highly dispersive element for a microspectrometer. Ideally, the targeted PDMS-based AWG should operate with high resolution throughout the entire visible light range (400 – 800 nm). Operation in visible light range is important for most biochemical spectroscopy applications; at the same time, previously reported AWG realizations have severe limitations and fundamental structural differences from our design.
- To design PDMS-based AWGs for high resolution (1 nm) and large free spectral range (>300 nm) based on the limitations, properties and fabrication method of PDMS materials. Conventional and non-conventional AWG layouts will be explored to meet the necessary specifications.
- To study the optical performance of the fabricated PDMS-based AWGs in terms wavelength separation, spectral range, insertion loss, polarization dependency and cross talk.
- To investigate the fabrication-related errors and deviations of the optical characteristics between simulated and fabricated PDMS AWGs.
- To study and explore various integration schemes of PDMS planar waveguides together with microfluidics for absorption spectroscopy sensing. Planar waveguides as part of the microspectrometer provides the sensor platform for analytes.
- To characterize the absorbance measurement performance of the integrated PDMS systems i.e. which combines both waveguides and

microfluidics in terms of sensitivity, limit of detection and signal-to-noise ratio.

- To enhance the optical detection limit by novel configurations and methods leveraging on the PDMS material properties as the device scales down. The optical detection performances are adversely affected when the size/dimensions of the microoptical components shrinks together with the microfluidic channel.
- To propose a complete integration of both microspectrometer and microfluidic structures for visible light absorption spectroscopy in a LOC platform which – in the future – could also integrate in a single chip the photodetectors and signal processing circuits.

1.3 Major contribution of the thesis

1. The design, fabrication and experiments of single-mode poly(dimethylsiloxane) (PDMS) rib waveguides were demonstrated for the first time. Based on geometrical parameters optimizations, the fundamental mode was designed to propagate with high confinement and low propagation whereas higher order modes were designed to couple into the slab waveguide region and propagate in a leaky mode.
2. Three methods of modifying the refractive index contrast Δn between the core and cladding of the waveguide were studied. The first two methods were achieved by modifying the properties by adding either hexane or silicone oil solvents in the same PDMS base material. Lastly, a higher refractive index contrast was obtained by using PDMS materials from two different manufacturers.
3. The fabrication of small core size PDMS rib waveguides (<8 μm) by soft lithography with high fidelity and low sidewall roughness. Optimization was performed for the soft lithography fabrication, particularly for the realization of the master mold as well as for the two step curing process of the core and cladding layers.
4. The measurement of the rib waveguide mode profile characteristics and corroborated the fundamental mode propagation in the waveguide by the comparison between simulated and measurement results.
5. The insertion losses of multi-mode PDMS waveguides in both straight and curved shapes waveguides that were measured in terms of propagation loss, transition loss and radiation loss. The PDMS multimode waveguides with a

high refractive index contrast obtained by using the third refractive index modification technique has shown improved propagation loss.

6. The successful demonstration of PDMS single-mode rib waveguides as basic building block for subsequent more complex microphotonics devices, such as Y-branch splitter.
7. The design, fabrication and experimental testing of two types of PDMS AWG as the wavelength discrimination element for a microspectrometer were demonstrated for the first-time. The first type is a conventional layout PDMS AWG for operation in the visible light wavelength range from 639 to 644 nm with four-channel outputs with 1 nm channel spacing. The purpose is to demonstrate nanometer resolution wavelength discrimination in PDMS AWG. The second type is a non-conventional PDMS AWG (an S-shape AWG) targeted to cover the whole visible light wavelength range with red, green and blue (RGB) outputs. The purpose is to demonstrate large free spectral range in PDMS AWG.
8. The measured insertion loss for the conventional AWG is 11.4 dB at the peak transmission spectrum and the adjacent crosstalk is less than -16 dB for the conventional layout PDMS AWG. The polarization dependency of the PDMS AWG is low and negligible provided that the single-mode rib is properly designed with respect to its geometrical parameters. Simulation studies of the dependence of the rib waveguides performance on geometrical and material properties were performed to analyze the fabrication-related performance errors of the PDMS AWG.

9. Modal images from the fabricated S-shape non-conventional PDMS AWG were taken and characterized, showing that the AWG exhibited large free spectral range (> 200 nm) and operated at a very low diffraction order of 2.
10. The direct integration of PDMS microfluidics with straight and curved multi-mode waveguides was achieved for absorbance measurements of fluorescein. The characterization of the optical detection performance of the microfluidic integrated with waveguides in PDMS was carried out to gauge the sensitivity, limit of detection and signal-to-noise ratio. The real-time measurement of fluorescein was demonstrated and it revealed the microfluidic system performance in terms of flow rates, stability and repeatability.
11. The sensitivity of the system was increased by reducing the stray light in the system by unique integration of PDMS curved waveguides with the microfluidic channel. Additionally, multiple total internal reflection (MTIR) in PDMS was produced in the channel to lengthen the optical path-length for increased sensitivity. The sensitivity of the absorbance measurement increased by 18 fold as light reflected four times in the PDMS microfluidic channel.
12. The evanescent field absorption spectroscopy was realized on small core size PDMS single-mode waveguide. It has successfully circumvented the diffraction loss problem caused by the small beam diameter of light traversing across the microfluidic channel. Successful immobilization of oligonucleotide was accomplished on the waveguide by sequential pumping of reagents and was subsequently utilized for evanescent field absorption spectroscopy.

1.4 Organization of thesis

This work focuses on the design, fabrication and characterization of PDMS-based microspectrometer optical systems. It first explores and investigates PDMS planar waveguides that allow the construction of complex microphotonics devices such as arrayed waveguide grating for spectrometers. The PDMS-microspectrometer of interest must be able to be integrated with microfluidics to achieve a lab-on-a-chip (LOC) spectrometer.

Chapter 2 of this thesis begins with the basic principles of spectroscopy and its common instrument setup. The design considerations essential for the spectrometer's performance, such as resolution, throughput and free spectral range, are explained and compared for different types of spectrometers. Next, the basic principles of planar waveguides are introduced followed by explaining how they can be utilized for the construction of a microspectrometer. A review of existing microspectrometers is presented together with some examples of such reported realizations with lab-on-a-chip systems. Finally, a survey of monolithic integration of PDMS-based microoptical components and microfluidics for spectrometry is presented.

Chapters 3, 4 and 5 cover our novel PDMS microspectrometer for LOC architecture. This device is constructed from the basic PDMS planar waveguides. Single-mode PDMS rib-shaped waveguides were designed and implemented for the construction of both an arrayed waveguide grating as a wavelength discrimination device and an evanescent sensor for absorption spectroscopy.

Chapter 3 will present the theory, design and fabrication of PDMS rib waveguide for both single-mode and multi-mode propagation. The theory and

physics of the waveguide is presented and various simulation methods are explained. The design of single-mode PDMS rib waveguides is detailed. This chapter will also cover the characterization of the PDMS rib waveguides in Chapters 4 and 5.

In chapter 4, the theory, design and fabrication of a PDMS AWG based on the single-mode rib waveguide will be covered. Two types of PDMS AWG, with a conventional and an S-shaped layout, respectively, will be presented for meeting the two key design specifications of high resolution and large free spectral range. The characterization of the PDMS AWGs in terms of insertion loss, polarization dependency, cross talk and channel uniformity will be shown. In addition, the issues of practical implementation of such PDMS AWGs are discussed.

Chapter 5 will cover the monolithic integration of the planar waveguides with microfluidics for the realization of a LOC microspectrometer. Free space sensing and evanescent field sensing schemes are investigated based on the limitations of the multi-mode and single-mode waveguides. The performance of such optical systems based on PDMS waveguides will be presented and discussed.

In conclusion, we will discuss how PDMS-based microspectrometers are designed and tested as well as how they perform compared to other existing microspectrometers. We will then propose some future work for the application of a PDMS-based microspectrometer in a LOC system.

CHAPTER 2

LITERATURE SURVEY

The objective of this chapter is to present a detailed literature survey on the basics of spectroscopy and the important tool used for this task – the spectrometer. After establishing the fundamentals of spectrometry, the theoretical considerations necessary for the design of a miniaturized spectrometer or microspectrometer are described, with specific focus on the two most important types of physical instruments used as key spectral discriminations in such machines, the diffraction grating and the Fabry-Pèrot interferometer.

Next, the principles of planar waveguide technology are introduced as the basis for building a planar microspectrometer that could be integrated and used within a LOC system. The structure and design of our proposed type of planar microspectrometer, namely the implementation of an arrayed waveguide grating (AWG) as a wavelength discrimination device, is then explained further.

We will review the existing microspectrometers fabricated in different materials and substrates, from silicon to polymer materials, using either diffraction grating or a Fabry-Pèrot inteferometer. The variations and different types of these two categories of microspectrometers will be presented as well as other important similar devices, such as the AWG and the linear variable filter. The focus of the review will be on microspectrometers which operate in the visible light range.

Several examples of improved optical detection in LOC by co-integration of planar waveguide technology with microfluidics are reviewed. Finally, a review of the PDMS as the material of choice for the fabrication of the microspectrometer and its associated microfluidics is illustrated with explanations of the design and fabrication of PDMS waveguides.

2.1 Basic principles of spectroscopy and spectrometer

The optical spectrometer aims to detect and analyze the spectral intensity distribution of an optical signal originating from the sample of interest e.g. reflection or absorption. The spectroscopic measurement (or spectroscopy) is related to the molecular composition and structure of the biochemical species. A typical spectroscopy involves the following steps. Light at a certain wavelength is used to irradiate a sample of interest. This step is called "excitation". In the next step, some of the properties of the light that emerges from the sample are measured and analyzed.

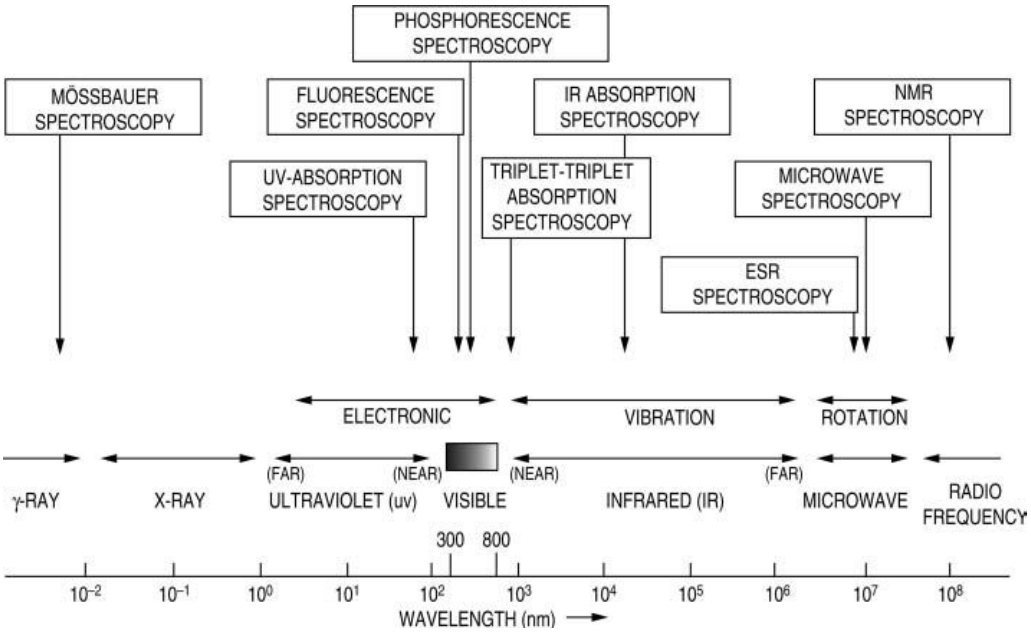

Figure 1: Various types of spectroscopies and related spectral range in the electromagnetic spectrum [25].

It can be divided into three categories;

1) Absorption spectroscopy deals with the fraction of the incident light being absorbed by the sample which is termed absorption spectroscopy and can be categorized according to the wavelength of light such as ultraviolet (UV), visible, and infrared (IR) absorption spectroscopy.

2) Scattering (elastic and inelastic) spectroscopy involves analyzing the radiation dissipated (absorbed and re-emitted) from the samples at the same wavelength as the excitation beam (elastic scattering techniques)

3) Emission spectroscopy deals with the light emitted and scattered by the sample but measured at a different wavelength than the excitation wavelength, e.g. fluorescence, phosphorescence and inelastic scattering (Raman scattering).

A very broad range of wavelengths is used in spectroscopy to study biological molecules, as it is shown in Figure 1 [25].

The main components of an optical spectrometer are:

1. An excitation light source
2. A wavelength discrimination element (dispersive or interference-based e.g. optical filters, monochromators, polychromators)
3. A sample (in a compartment or holder)
4. An optical system to focus light (with entrance aperture and exit aperture)
5. A photodetector (equipped with read-out devices)

The basic components of the spectrometer must be configured according to the various types of spectroscopic measurement. Figure 2 shows the component setups for the three main types of spectroscopy measurements for biochemical

species: absorption, scattering and emission spectroscopy. The setup for absorption spectroscopy consists of a collimated output beam from a light source, focused to the entrance slit of a dispersive element for wavelength scanning. The output from the dispersive element is directed to the sample. Transmitted light from the sample is focused to the photodetector by an optical system. A simple single beam spectrometer can be modified into a double beam instrument by adding a reference beam to correct any spectral fluctuations in the lamp.

For scattering spectroscopy, typically the backscattering of the broadband light source is detected rather than a transmission arrangement. The detected light is measured at a different wavelength from the excitation wavelength. Therefore, two dispersive elements are required. For emission spectroscopy, the requirement includes a high intensity light source such as a laser or a xenon arc lamp for the excitation. The excitation beam and the emission beam are usually arranged in a right angle setup to reduce the interference from scattered light.

The three major factors to consider when selecting and designing an optical spectrometer are the excitation light source, the resolution and throughput, and the wavelength sensitivity of the photodetectors. Although a high intensity light source is often desirable for the excitation, the cost-benefit has to be taken into consideration. Fluorescence spectroscopy at room temperature does not need excessively high resolution because the bandwidth of fluorescence spectra is usually larger than 5 nm. However, very high resolution (less than 1 nm) is needed for absorption spectroscopy to resolve the narrower electronic bands or the vibrational bands of the molecular structure.

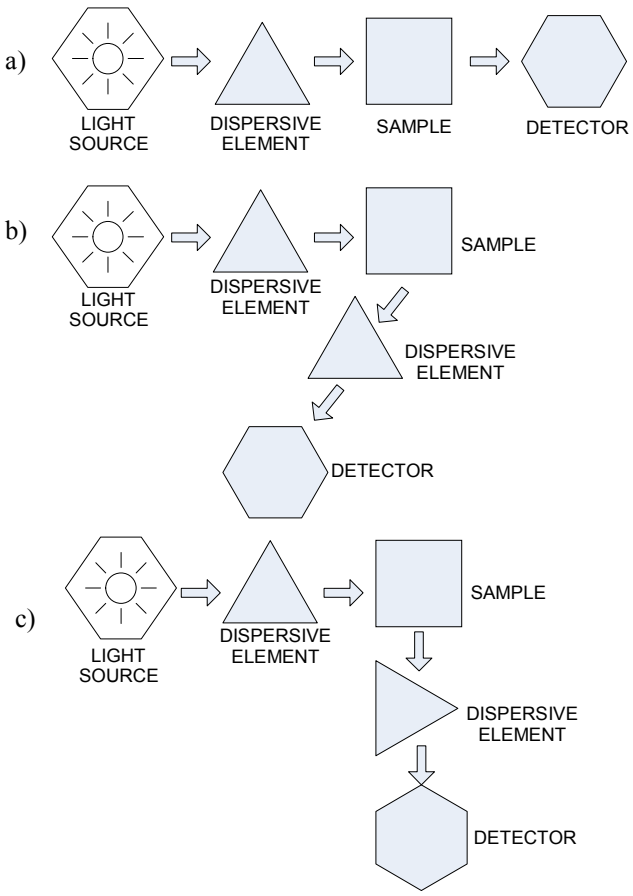

Figure 2: Various instrument setup for: a) absorption, b) scattering and c) emission spectroscopy, respectively.

2.1.1 Microspectrometer for lab-on-a-chip

Three important theoretical and design considerations for the optical microspectrometer are resolution, throughput and operating wavelength range.

The resolution of a spectrometer is the ability of the spectrometer to separate adjacent wavelength and is expressed as

$$R = \frac{\lambda}{\Delta\lambda} \tag{1}$$

where λ is the center wavelength, and $\Delta\lambda$ is the smallest wavelength spacing between two unique wavelengths that can be discriminated.

The throughput, or étendue, of a spectrometer is the light gathering power of a spectrometer. The term reveals the amount of light that passes from the source through the spectrometer to the detector. Generally, the throughput depends on the cross sectional area of the entrance aperture and the solid angle extended by the entrance aperture of the optical element or dispersive element, and is expressed as

$$\Phi = \text{area of aperture} \times \text{solid angle of the aperture} \quad (2)$$

The operating wavelength range is the wavelength range in which the spectrometer works and is constrained by the detector wavelength response, optical microcomponents and the free spectral range (FSR) of the device.

For LOC applications of a microspectrometer, additional considerations to be taken into account are the ease of integration, the complexity of the fabrication technique and the material cost of the chip. In addition, this work focuses on the realization of a microspectrometer for visible light absorption spectroscopy.

2.1.2 Types of microspectrometers

2.1.2.1 Diffraction grating-based (micro)spectrometers

Two major types of physical mechanisms are typically employed for the wavelength discrimination necessary in a microspectrometer, namely diffraction or interference. A third mechanism, dispersion due to material properties dependence on wavelength, has also been used in the past, particularly in old spectrometers (late 19^{th} and early 20^{th} century), when diffraction gratings were inexistent or difficult to make and expensive. This method, employing a (glass) prism, sometimes is still used today in a few high performance spectrometers. Both diffraction and dispersion separate the

wavelengths spatially so that a detector array placed at some distance from the dispersive element (prism or diffraction grating) detects each individual wavelength at different locations. On the other hand, interference works by splitting the light into two or more beams and a phase difference is introduced into one of these beams. Subsequently, the beams are combined and as interference occurs between these beams the resultant produced light has a wavelength dependence characteristic.

The most common (micro)spectrometer employs a diffraction grating as the dispersive element. The general optical setup of such a grating-based spectrometer is shown in Figure 3. Light from a broadband source is passed through an input aperture and collimated by the lens onto the grating. The periodic structure on the grating creates individual wavelets source and the emerging wavefront contains periodic variations and tilts according to its wavelength. For a particular wavelength, constructive interference of the wavefront produces maxima intensity at a specific location. For a grating with period d and incoming light at an incident angle θ_i, the basic governing equation to determine the transmitted/reflected angle after diffraction is given by [26]

$$d(\sin\theta + \sin\theta_i) = m\lambda \tag{3}$$

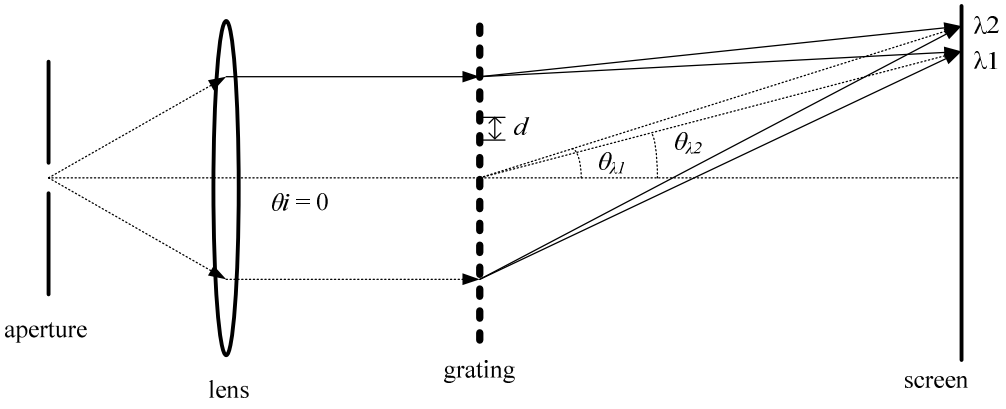

Figure 3: The basic configuration of a grating spectrometer.

where m is the diffraction order and λ is the wavelength.

Thus, the angular dispersion can be expressed as

$$\frac{d\theta}{d\lambda} = \frac{m}{d\cos\theta} \tag{4}$$

For a grating with a number N of illuminated lines, the resolution is given by

$$R = mN \tag{5}$$

The free spectral range FSR is the largest wavelength range for a given order m that does not overlap the same range in an adjacent order. If the $(m+1)^{th}$ order of λ and $(m)^{th}$ order of $(\lambda + \Delta\lambda)$ lie at the same angle, then $\Delta\lambda$ is the FSR and given by

$$FSR = \frac{\lambda}{m} \tag{6}$$

The throughput of the grating is given by [26]

$$\Phi = \frac{\beta\lambda}{R} A \frac{\sin\theta + \sin\theta_0}{\lambda} \tag{7}$$

where A is the area of the grating, and β is the angular height of the aperture.

2.1.2.2 Inteference-based (micro)spectrometers

The Fabry-Pèrot interferometer as shown in Figure 4 is the most often used device for wavelength separation in (micro)spectrometers and consists of a dielectric with two parallel planes which are partially reflective and separated by a distance, d.

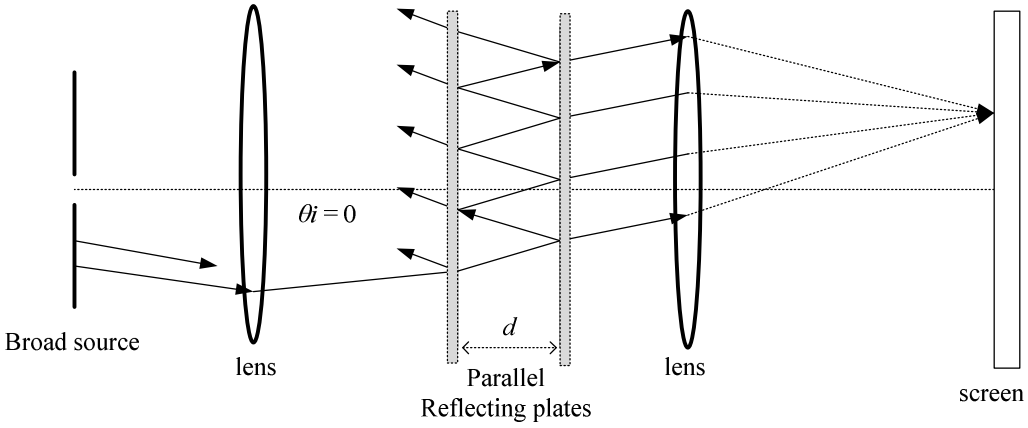

Figure 4: Basic configuration of the Fabry-Pèrot interferometer.

It is termed an interferometer if the distance d is movable (e.g. an adjustable air gap) and an ètalon if the distance is fixed. As the light ray enters the dielectric, it is reflected multiple times between the partially reflecting plates. At a certain dielectric thickness (gap distance), constructive light occurs for a particular wavelength and passes through the Fabry-Pèrot filter with a strong intensity. The governing equation for the transmission of light through a Fabry-Pèrot is expressed as [26]

$$T = \left[1 - \frac{A}{(1-R)}\right] \frac{1}{1 + F \sin^2\left(\frac{\delta}{2}\right)} \tag{8}$$

where A is the absorption of the cavity, R is the reflectance of the two surfaces, and F is defined as

$$F = \frac{4R}{(1-R)^2} \tag{9}$$

while δ is the phase difference between two successively transmitted waves and is defined as

$$\delta = \frac{4\pi n_f}{\lambda_0} d \cos\theta_t + 2\phi \tag{10}$$

where n_f is the index of the material between the plates, λ_0 is the wavelength in air, θ_t is the transmitted angle and φ is the phase shift from the reflecting plates. The resolution is expressed as

$$R = \Im m \tag{11}$$

where m is the order and $\Im$ is the finesse of the cavity defined as the separation of adjacent maxima to the full-width-half-maximum of one peak and given as

$$\Im = \frac{\pi\sqrt{F}}{2} \tag{12}$$

The throughput of the Fabry-Pèrot spectrometer is expressed by [26]:

$$\Phi = \frac{\pi}{R} A \tag{13}$$

where A is the area of the Fabry-Pèrot interferomer illuminated by the incident beam.

The free spectral range of the Fabry-Pèrot is given by

$$FSR = \frac{\lambda^2}{2d} \tag{14}$$

2.2 The Planar waveguide

The basic function of a planar waveguide is to guide light. A planar waveguide consists of a central core layer sandwiched between two cladding layers whose refractive indices must be lower than that of the core layer. The planar waveguide is fabricated by depositing the core layer over a substrate which acts as the bottom cladding layer. A top cladding is deposited on the core layer or is sometimes absent and air acts as the top cladding. Planar waveguides can be fabricated using several types of materials and has found a variety of applications. For instance, fiber optic communication systems make use of planar waveguides made of electro-optic materials incorporated with light

emitting diodes or semiconductor lasers. Likewise, silicon-based, silica and polymer waveguides have also been used for a wide variety of applications particularly in LOC systems.

The integration of planar waveguides together with other microoptical and/or electronic components has been pursued for optical detection in LOC to limit the misalignment problem as well as to produce a high level of functionality. Furthermore, the planar waveguides can be used for building complex microphotonics devices for spectrometric applications, such as Mach-Zender filters, multi-mode interference couplers and arrayed waveguide gratings.

2.2.1 The basic operation principle of optical waveguides

The optical waveguide structure consists of a core surrounded by a cladding so that the light is confined in the core, as shown in Figure 5. The refractive index of the core n_1 is higher than that of the cladding n_0. As the light is being coupled to the end face of the optical waveguide, it is confined in the core by total internal reflection at the core and cladding interface and continues to propagate in the core. The condition for total internal reflection at the core and cladding interface is given by $n_1 \sin\left(\frac{\pi}{2} - \varphi\right) \geq n_0$.

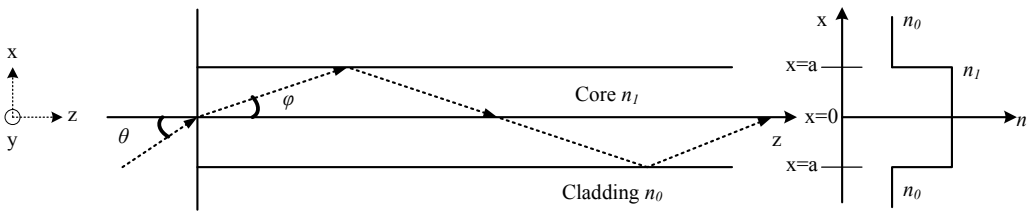

Figure 5: Basic structure and refractive index profile of an optical waveguide.

The angle φ is related to the incident angle θ by the relationship $\sin\theta = n_1 \sin\varphi \le \sqrt{n_1^2 - n_0^2}$, the critical condition for the total internal reflection can be obtained as $\theta \le \arcsin\sqrt{n_1^2 - n_0^2} = \theta_{\max}$. θ_{max} denotes the maximum light angle acceptance of the waveguide and is termed the *numerical aperture* (*NA*).The relative refractive index difference or *refractive index contrast* is given by the following equation and is usually stated in percentage form [27]:

$$\Delta = \frac{n_1^2 - n_0^2}{2n_1^2} \tag{15}$$

2.2.2 Formation of guided modes

A light ray with an arbitrary incident angle does not necessarily be able to propagate in the optical waveguide even if the angle θ is smaller than the θ_{max} because light ray propagation in a waveguide is also associated with a different mode for each discrete angle of propagation. The mode can be found by performing a detailed electromagnetic wave analysis based on Maxwell's equations. Consider a plane wave propagating at angle φ to the z-direction as shown in Figure 6. The phase fronts are perpendicular to the plane waves and their wavelength and wavenumber are λ/n_1 and kn_1 where $k = 2\pi/\lambda$.

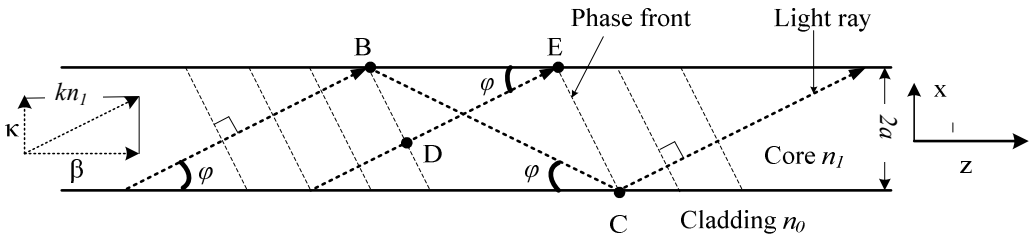

Figure 6: Light rays and their phase fronts in the optical waveguide. The light is polarized perpendicular to the incidence plane.

The propagation constants along the z-direction and x-direction are expressed by

$$\begin{aligned} \beta &= kn_1 \cos\varphi \\ \kappa &= kn_1 \sin\varphi \end{aligned} \tag{16}$$

Using the Fresnel reflection coefficients, the reflection coefficient of the total internally reflected light, which is polarized perpendicular to the incident plane, as shown in Figure 6 is given by,

$$r = \frac{n_1 \sin\varphi + j\sqrt{n_1^2 \cos^2\varphi - n_0^2}}{n_1 \sin\varphi - j\sqrt{n_1^2 \cos^2\varphi - n_0^2}} \tag{17}$$

Based on the complex reflection coefficient $r=\exp(-j\Phi)$, the amount of phase shift can be obtained from the reflection coefficient as

$$\Phi = -2\arctan\frac{\sqrt{n_1^2 \cos^2\varphi - n_0^2}}{n_1 \sin\varphi} = -2\arctan\sqrt{\frac{2\Delta}{\sin^2\varphi} - 1} \tag{18}$$

Consider the light rays BC and DE which originate from the same plane wave. The phase difference between these two light rays has changed because the light ray BC has reflected two times as it propagates from B to C whereas the light rays DE has not reflected at all. As shown in Figure 6, the points B and D or C and E are on the same phase front, hence, the optical path BC and DE (including the phase shift due to two total internal reflections) should be equal, or their difference should be an integral multiple of 2π.

The length l_1 and l_2 of segments |BC| and |DE|, can be easily deduced to be

$$l_1 = \frac{2a}{\sin\varphi} \tag{19}$$

and

$$l_2 = \left(\frac{2a}{\tan\varphi} - 2a\tan\varphi\right)\cos\varphi = 2a\left(\frac{1}{\sin\varphi} - 2\sin\varphi\right) \tag{20}$$

Hence, the phase matching condition for the two optical paths of BC and DE is

$$\left(kn_1 l_2 + 2\Phi\right) - kn_1 l_1 = 2m\pi \tag{21}$$

Substituting equation (19) and (20) into (21), the condition for the propagation angle φ can be obtained as

$$\tan\left(\frac{2\pi}{\lambda} n_1 a \sin\varphi - \frac{m\pi}{2}\right) = \sqrt{\frac{2\Delta}{\sin^2\varphi} - 1} \tag{22}$$

Equation (22) shows that the propagation angle is discrete and is determined by the waveguide structure (core radius a, refractive index n_1, and refractive index constrast Δ) and the wavelength of the light λ. The optical field distribution that satisfies the phase matching condition is called propagation mode and the minimum angle φ is obtained for the fundamental mode (m = 0) and larger angles result for higher modes ($m \geq 1$).

2.2.3 Planar waveguides for spectrometers: The array waveguide grating

A notable device for wavelength division multiplexing systems which is based on the planar waveguide technology and has wavelength separation capabilities is the arrayed waveguide grating (AWG). Figure 7 shows the schematic diagram of an AWG.

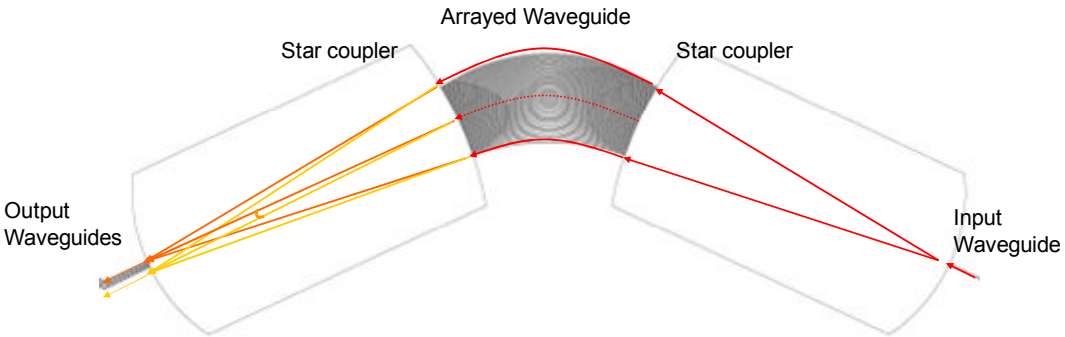

Figure 7: The schematic diagram of the AWG operating principle.

It consists of two $N \times M$ star couplers (a star coupler is in effect a continuous region of bulk material where the light beam propagates freely) and an array of M waveguides with constant length difference between adjacent waveguides that creates a constant phase difference resulting in a grating-like behavior which can be used for spectrometric wavelength discrimination.

The wavelength separation carried out by the AWG can be understood in simple physical terms as follows. The first star coupler spreads the incident light power onto the array of waveguide forming the grating. After travelling through the waveguide, the wavefront emerging from the output of the array of waveguide is tilted since each waveguide has a slightly different length and thus imparted a slightly different phase shift to the beam propagating through it. The tilt is wavelength dependent and each wavelength is focused by the second star coupler onto a different output waveguide. This physical behavior is similar to that of a diffraction grating where the wavelengths are directed at different angles. The star coupler and arrayed waveguide plays the roles of the lens and of the diffraction grating.

2.3 Previously reported microspectrometers for lab-on-a-chip (LOC) platforms

2.3.1 Microspectrometer with integrated microfluidics

As was mentioned in the previous section, microspectrometers can be categorized in one of two types, depending on wavelength discrimination element, namely employing either a Fabry-Pèrot interferometer or a diffraction grating.

The first Fabry-Pèrot microinterferometer fabricated using silicon micromachining technique was reported by Jerman et al., and was intended to be used as a wavelength division demultiplexer in optical fiber communications [28]. Jerman's bulk micromachined device consisted of a released silicon mirror supported from the centers of its sides by silicon arms and its operation was limited only to near infrared wavelengths because silicon is not transparent to the visible light range. Thus, Raley et al. further developed a silicon-based microinterferometer adapted from the work of Jerman et al. employing bulk micromachining technique [29]. In this case, silicon nitride membrane were used instead of thick silicon wafers to form the mirrors in order to suit the need for operation in the visible light range. The device has shown a resolution of 1.6 nm at 450 nm with a very limited free spectral range. Moreover, bulk micromachining does not lend itself to high density arrays and thus led Aratani et al. to employ surface micromachining for the fabrication of the interferometer small air gap between the mirrors could be electrically tuned to a controlled thickness using small voltages and could be used for red as well as near infrared light [30].

One crucial requirement for the realization of a high performance Fabry-Pèrot interferometer is the fabrication of high flatness mirrors, usually in the order of $\lambda/10$. Therefore, a device operating at for a λ = 450 nm demands a mirror flatness of 45 nm or better. This has led to the work of Correia et al. who improved the fabrication process and achieved a high flatness interferometer with low control voltage of less than 21 V for a 450 nm deflection compared with Raley's 100 V [31].

These Fabry-Pèrot microspectrometers contain movable parts which require high voltage electrostatic actuation for cavity tuning and typically exhibit a limited free spectral range. Therefore, Correia et al. proceeded to develop an array type single chip microspectrometer with many separate fixed mirrors, each for a different range, so that the entire array of such mirrors could cover a larger free spectral range [32]. This array of fixed Fabry-Pèrot microspectrometers realized using Ag thin films as mirrors and a SiO_2 dielectric achieved a FWHM of 16 nm for a FSR from 400 to 520 nm, or a FWHM of 1.8 nm for an operating range between 400 to 470 nm [33]. Based on this array consisting of 16 different Fabry-Pèrot ètalons for 16 different wavelength channels, Minas et al. redesigned the chip and achieved a higher performance microspectrometer with a FWHM less than 6 nm for an operational range between 450 to 650 nm with a peak intensity higher than 86% [34]. Combining these CMOS compatible Fabry-Pèrot filter arrays and electronic circuits for signal processing with an SU-8 polymer microfludic chip, the group further demonstrated uric acid and total protein spectroscopy measurements [35]. Hence, the group achieved the first absorption spectroscopy on a LOC platform albeit with a low resolution performance limited to 16 channels. Other than using a fixed gap Fabry-Pèrot interferometer, a linearly varying gap Fabry-Pèrot has been proposed by Schmidt et al., termed as the Linearly Variable Filter (LVF) and demonstrated for fluorescence spectroscopy [36]. Nonetheless, the LVF requires sophisticated fabrication techniques and compromises the resolution by having a non-parallel mirror.

The first attempt to miniaturize a grating-based spectrometer for chemical sensing was demonstrated by Goldman et. al [37]. In this demonstration, two

types of planar waveguides, one made up of polystyrene and the other made of tantalum pentoxide were employed on top of buried gratings which had been etched into the substrate. Light was focused into the waveguides through the first grating and spatially dispersed by the second grating after propagating in the waveguides. An external photodetector array collected the resultant spectral data. Although the photodetector was not integrated with the grating, this device demonstrated an absorption measurement of Congo Red Dye. Kwa et al. integrated the photodetector with grating by using silicon micromachining techniques [38]. A top wafer in which a 32-slit transmission diffraction grating and a detector array had been integrated was fusion bonded to another wafer with a trapezoidal bulk micromachined mirror coated with a reflective film. The final structure produced an optical path-length of 4 mm. This short optical path-length limited the dispersion of the light and thus did not allow considerable resolution for biological applications. As an alternative to the on-chip microspectrometer approach, Yee. et al. demonstrated a miniaturized chip-to-chip spectrometer for biochemical analysis by mounting micromachined diffraction gratings onto CCD imaging devices [39]. The resolution of the device was 8.5 nm FHWM at 632 nm. Similarly, Avrutsky et al., using a CCD imager as a light detector, improved the resolution to 2 nm by mounting the grating at an oblique angle with a distance longer than that used by Yee et. al [40]. However, unlike Yee et al., no demonstration of biological analysis was performed by Avrutsky.

Based on silicon micromachining and the LIGA process, Mohr et al. fabricated a three layer resist light guiding and planar grating spectrograph [41]. The light to be analyzed was introduced into the three layer resist waveguide

through an optical fibers, was dispersed by a reflection grating, and projected onto an array of fibers that guided it to an array of photodetectors. The planar arrangement provided a longer optical path-length, dispersing broadband light into 8 individual waveguides with 20 nm resolution each. Hence, it achieved a resolution $R = 10$ in the spectral range 720 and 900 nm. A similar approach has been implemented by Sander et al. with a transmission grating. Sander et al. presented an integrated microspectrometer for operating in the visible light range utilizing a silicon oxynitride waveguide and a transmission grating as dispersive element [42]. The same group further improved this design by employing a self-focusing grating which covered a spectral range between 350 and 650 nm with 10 nm resolution [43]. The detailed review of these optical microspectrometers fabricated using silicon-based technology has been reported by Wolffenbuttel [44].

The fundamental limitation of the grating-based microspectrometer is the intrinsic requirement of providing for a sufficient distance for the spatial dispersion of the separated wavelengths. Grabanik et al. has addressed this issue with a multireflection design with two gratings [45], which achieved a resolution of 3 nm in the spectral range 450 nm to 750 nm. On the other hand, the resolution of a diffraction grating can also be improved by utilizing a higher order of diffraction. According to equation (3), the highest order of diffraction m for a visible light incident at 0˚ for a commercially available grating will not be larger than 4. However, the invention of array waveguide grating in 1988 had made possible operation at a very high order [46].

The AWG form another very large category of wavelength-discriminating devices and traditionally they have been fabricated using silica-

on-silicon and semiconductor waveguide technologies [47, 48]. The AWG has originally been developed and almost exclusively used for wavelength division multiplexing (WDM) systems in telecommunications, namely for high port counts and narrow channel spacing. Near infrared operation AWGs have been pursued because of the WDM system application requires an operating wavelength of 1.3 to 1.55 μm. In 1996, an 128 input and output channels AWG with only 25 GHz (~0.012 nm) channel spacing around the 1.55 μm wavelength has been demonstrated [49]. Further advancements led to more complex devices, e.g. the realization of a 400 channels AWG with 25 GHz spacing [50]. The AWG has the capability of achieving subnanometer resolution because multiple numbers of phase differences can be created in an array of waveguides. Hence, based on this concept, a silicon-based microspectrometer has been demonstrated by Cheben et al. with a very high resolution of only 0.07 nm [51]. However, its spectral range was limited to 14 nm and operated only in the near infrared range.

However, AWGs have also been used for other applications besides telecommunications. The first known integration of a AWG with channel grooves for fluidic spectroscopy sensing was realized in silica-on-silicon by Japan's NTT lab and also operated in the near infrared range [52]. Later, a visible light operating AWG was realized in 2006 by the same group [53], which they have demonstrated spectroscopy for fluid solutions of chlorophyll *a* and *b* [54]. Subsequently, a parabolic waveguide was integrated with microfluidic channel for enhancement of the spectroscopic discrimination [55].

Table 1 shows the various types of microspectrometers which have been built for LOC applications.

Spectrometer Type	Resolution	Material	Type of Spectroscopy	Sample
Grating [39]	8.5 nm	Silicon Grating on CCD device	Absorption Spectroscopy	Fluorescent dye for DNA detection
Fabry Pèrot Etalon [35]	6 nm	Silicon-based Fabry-Pèrot Filter. CMOS compatible photodetector. SU-8 Photoresist microfluidic layer.	Absorption Spectroscopy	Uric acid in urine
Array Waveguide Grating [55]	12.5 nm	Silica based	Absorption Spectroscopy	Chlorophyll a & b in oil
Linear Variable Bandpass Filter [36]	N.A.	A linear variable filter on top of 12 bit CMOS sensor	Fluorescene Spectroscopy	Fluorescent particles

Table 1: Figures of merit for various types of reported microspectrometers for LOC applications.

The Fabry-Pèrot-based type shows the highest resolution but with a limited spectral range while the LVF allows a much broader operating range but with poor resolution and therefore is best suited only for less stringent fluorescence spectroscopy applications.

2.3.2 Limitations of grating and Fabry-Pèrot based microspectrometers

The grating-based microspectrometer has limitations in achieving high resolution as the size of the device scales down to micrometer range. The main impediment is having sufficiently long optical path-length (D) for both the distance between aperture and grating as well as distance between grating and

screen (or detector) as depicted in Figure 3. To utilize the grating equations (3), the basic assumption is that the Fraunhofer diffraction occurs rather than Fresnel diffraction. Fraunhofer diffraction requires that the law of far fields to be valid, i.e. the above mentioned optical path-length D must be larger than the Rayleigh distance which is given as [26]

$$D = \frac{\beta^2}{\lambda} \tag{23}$$

For an N-element grating, the aperture β can be taken as Nd where N is the number of grating lines and d is the pitch of the grating which depends on the fabrication technology. Therefore, equation (23) can be rewritten to give the maximum number of elements N_{max} as

$$N_{\max}^2 = \frac{D\lambda}{d^2}$$

For instance, a visible light (at λ = 550 nm) microspectrometer which targets small footprint has a limit of 1 mm on the optical path-length while the grating fabrication constraint of 0.2 μm will give N_{max} = 135. As a result, the maximum resolution R of a first order grating microspectrometer is only 135.

The second difficulty lies in the microfabrication of optically high quality grating. Grating imperfections produce scattered light and can be observed as Lorentzian-type noise and constant background components [56]. The Lorentzian-type noise has been predicted by the diffraction theory while the constant background component is due to Rayleigh scattering on the microscopic surface imperfections. Gratings fabricated using microelectronics and MEMS micromachining techniques have inevitable surface roughness as a result of dry etching process and the lack of suitable polishing techniques.

Lenses can be incorporated prior to the grating for collimating the incident light into a parallel beam as well as after the grating for focusing the dispersed spectrum at the minimum optical path-length. However, fabrication of such lenses has not been considered because of the current technological limitations. Consequently, the grating-based microspectrometers have been realized in almost all cases without optical signal conditioning and this has compromised the performance of the device.

The factors that limit the spectral resolution of the Fabry-Pèrot microspectrometer are different from the grating-type. The governing equation (8) of the Fabry-Pèrot interferometer states that high *finesse* is necessary for a high spectral resolution. It can be inferred from equations (8) and (9) that high reflectance of the mirrors is essential for attaining high *finesse* and high resolution. The fabrication of high reflectance mirrors necessitates a minimum thickness for a metal film based mirror [57]. A minimum thickness of 15 nm is required to produce a reflectance of 90% but absorption also increases rapidly as metal thickness increases. High absorption adversely affects the high transmission at the desired resonance wavelength. The transmission drops to lower than 15% in a 15 nm thick metal. It can be circumvented by utilizing multiple layers of dielectrics to form each reflecting mirror [58]. However, the fabrication of a multilayer stack of alternating materials with tightly controlled thickness and optical properties is incompatible with the standard silicon microelectronics process.

The spectral resolution for a Fabry-Pèrot microspectrometer can also be increased by operating at a high order, m. Consequently, the nominal width of the Fabry-Pèrot cavity has to be increased while maintaining the parallelism of

the two mirrors. The fabrication of a large width cavity becomes difficult with conventional micromachining techniques because the changes in the cavity in one device yield a wide range of resonance frequencies which reduce the spectral resolutions.

Theoretically, the *FSR* is inversely proportional to the cavity width as expressed in equation (14). Hence, the *FSR* is reduced as the cavity width increases to achieve high resolution. In addition, a large scanning movement is difficult as the practical cavity width modulation using electrostatic actuations is limited by pull-in of the microstructure.

2.3.3 Monolithic integration of waveguides and microfluidics

The monolithic integration of waveguides with microfluidics is important for both simplifying the LOC optical detection method (e.g. to steer the light around to the desired point) and for building complex microphotonic systems, such as a spectrometer. In the integration of waveguide and microfluidics, a few key factors have to be considered such as: the optical detection performance, selection of materials for low cost and the ability to be used as basic building blocks for complex microphotonics devices.

The integrated waveguide for detection are typically implemented either by free-space wave sensors or by evanescent wave sensors. The free-space wave sensor is more sensitive because all the light is launched into the microfluidic channel and interacts with the liquid sample. In contrast, only a small portion of the light in the evanescent field interacts with the liquid sample in the evanescent wave sensor. However, the free-space wave sensor suffers from increased losses due to unguided light in the detection channel. The integrated waveguides for LOC have been realized with, e.g., polymers in a free

space wave absorbance sensor [59] or with other dielectric materials (SiN and SiO_2) in a complex evanescent wave sensor [60]. Most often, the improvement of the optical detection performance in LOC dealt with reducing the optical losses as well as increasing the sensitivity and signal-to-noise ratio.

Several types of materials have been employed for integration of optical waveguides with microfluidics, including silicon oxynitride core with silica cladding [61,62], and polymer waveguides [63, 64, 65] as they exhibit very good transparency (low losses) in the visible light range. Silicon-based materials have initially been chosen because they can be readily implemented using fabrication techniques well-established in microelectronics. Nevertheless, the waveguides made of silica have turned out to be more costly than their polymer counterparts. Therefore, polymer waveguides have become the focus of attention with the recent trends in disposable biochips. For instance, a polymer waveguide made of SU-8, a photosensitive resin that allows photolithographic patterning, has been used in an integrated approach for absorbance detection [65]. However, relatively high propagation losses encountered with the SU-8 waveguides below 500 nm have made them unsuitable for applications requiring operation in the entire visible range.

In contrast, polydimethylsiloxane (PDMS) shows excellent transmission properties in the UV-visible range which make it an attractive material for optical microcomponents for the visible light range [66, 67]. PDMS is a very popular material used for microfluidic chips because of its chemical inertness, biocompatibility, permeability, low cost and rapid fabrication technique by soft lithography [66, 68]. Various optical components [69], such as 2D lenses [70], long-pass filters [71] and waveguides [72, 73] have already been demonstrated

in PDMS. PDMS has also been a favorite material for disposable biochips [66]. Several groups have aimed at a monolithic integration of waveguides and microfluidics all in a single PDMS chip [73, 74]. However, these devices have been implemented with either intrinsically "lossy" hollow waveguides where PDMS acts only as cladding [73], or liquid waveguides where PDMS does not take any part in the waveguiding process [74]. The liquid waveguides have been defined in microchannels by liquid-liquid interfaces which are mechanically unstable and hence require constant supply of liquids at controlled flow rates.

Dielectric waveguides integrated with microfluidic devices featuring complex microphotonics have demonstrated high sensitivity and selectivity in optical detection [75]. In comparison, the low cost polymer waveguides has yet to be developed into complex microphotonics devices and until now have only been used to realize simple straight or bend waveguides [76]. Hence, there is a need to develop complex microphotonics devices from polymers, particularly PDMS which could be used to build complex microoptical systems, such as a microspectrometer in a LOC system.

2.3.4 PDMS-based waveguide design and fabrication

PDMS-based waveguides have been reported as multi-mode waveguides with large cross-section (> 50 μm) and simple straight structure [72 – 74, 77]. None of these PDMS-based waveguides have shown single-mode propagation or complex photonics structures with added functionality. The main differences of these reported PDMS-based waveguides are the fabrication methods used for tuning the refractive index contrast between the core and cladding layer.

Splawn et al. used air (n = 1.0) as the core layer with PDMS (n = 1.45) for the cladding layer [73]. The basis of this hollow waveguide is based on the principle that light can propagate as evanescent wave on the interface of two different refractive indices. In another report, Wolfe et al. used two liquids with different refractive indices to create the core and cladding of the waveguide [74]. The two liquids were controlled under continuous flow to maintain the necessary liquid-liquid interface for confining the light. Both demonstrations of Splawn et al. and Wolfe et al. were fabricated using soft lithography technique with commonly used PDMS (Sylgard 184, Dow Corning Inc). The waveguides were either partially made of PDMS [73] or liquid waveguides contained in a PDMS chip [74].

To achieve a monolithic PDMS waveguide, the formation of refractive index difference between the core and cladding layer is vital. Thus, Chang-yen et al. proposed modifying the curing process of the PDMS (Sylgard 184, Dow Corning, Inc.) to produce the refractive-index difference between the core and cladding layer. PDMS (Sylgard 184, Dow Corning, Inc) is supplied in a non-cross-linked form and cross-linking occurs spontaneously over a period of 48 hours at room temperature when the base resin and curing agent was mixed at a ratio of 10:1. The cross-linking reaction time can be shortened by increasing the curing temperature. Chang-yen et al. has demonstrated that as temperature increased from 25 ^{o}C to 150 ^{o}C with curing time shortened to 1 hour, the refractive index of PDMS has changed by 0.02 [72]. The demonstrated fabrication process involved an optimized SU-8 photoresist mold for smooth pattern and additionally treated with detergent solution to prevent sticking of PDMS to the mold. PDMS precursor was first filled in the SU-8 mold and

excess PDMS was scraped off manually with a razor blade to define the core layer of the waveguide. The core layer was cured at 150 ^{o}C for 1 hour to create a higher refractive index PDMS. Subsequently, PDMS precursor was cured over the first layer at room temperature for 48 hours to produce the cladding layer. Finally, the PDMS was peeled off as a single PDMS chip.

In another demonstration to produce a similar monolithic waveguide, Kopetz et al. utilized a different commercial PDMS material (Elastosil RT 601, Wacker Chemie) for the cladding layer whereas the core layer was specially developed by Wacker Chemie with the provisional name SLM 77552 [77]. The refractive index has been increased by the introduction of phenyl groups in the side chain of the PDMS backbone for this specially formulated PDMS precursor. The fabrication process involved SU-8 as mold but without surface treatment for release. The blading process in the fabrication by Kopetz et al. was improved with a stencil printer with a motorized controller with a PMMA or POM blade to meet the demand of softness, flexibility and endurance. The cladding layer was cured with FR4 – printed circuit board, as a carrier. The final PDMS waveguide on FR4 layer can be used for electrical-optical board.

CHAPTER 3

POLY(DIMETHYLSILOXANE) RIB WAVEGUIDES

The objective of this chapter is to present the planar waveguide technology based on poly(dimethylsiloxane) (PDMS) rib waveguides. Firstly, the basic theory of rib waveguide is studied based on Maxwell's electromagnetic wave theory and equations. The calculations based on various simulation methods are explained and applied in the design of the PDMS rib waveguide. The design of single-mode propagation in the PDMS rib waveguides is presented based on geometrical parameters optimizations.

Next, details on how the refractive index contrast Δ between the core and cladding is achieved by modifying the properties of the same base material will be presented. Alternatively, a higher refractive index contrast is demonstrated by using PDMS materials from two different manufacturers. The fabrication methods for both multi-mode and single-mode PDMS rib waveguide are elaborated.

The characterization results for both multi-mode and single-mode PDMS rib waveguides are presented, with particular emphasis on the mode profile characteristics and the corroboration of the fundamental mode excitation in the single-mode waveguide. The insertion losses of the PDMS rib waveguides are shown in terms of propagation loss, transition loss and radiation loss.

Finally, the demonstration of single-mode PDMS rib waveguides as basic structures for building complex microphotonics devices, such as a Y-branch power splitter, is described.

3.1 Poly(dimethylsiloxane) rib waveguides

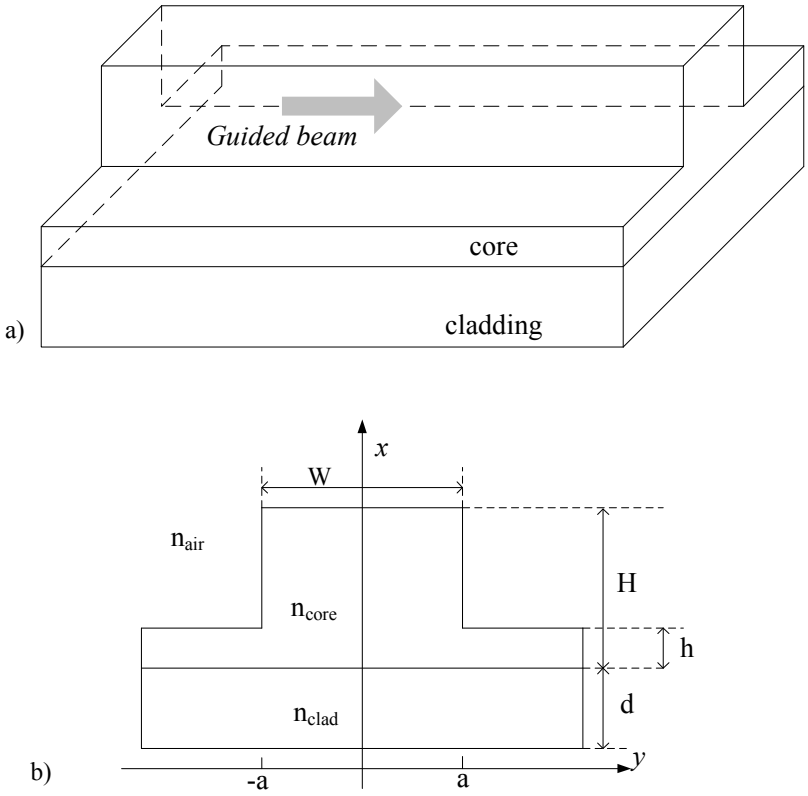

Figure 8: Schematic of the PDMS rib waveguides; a) 3-D structure view; b) cross-sectional view with geometrical parameters.

The PDMS optical waveguide has a rib structure as shown in Figure 8, consisting of three layers: the cover, core and cladding layers, respectively. The cover is air and the core and cladding layer are made up of different PDMS materials with different refractive indices. The refractive index contrast and the geometrical parameters of the waveguide will determine the mode propagating in the waveguide and the effective refractive index, polarization, power distribution, electric field strength and magnetic field strength characterizing the light propagating in the waveguide.

The refractive index of the PDMS can be modified by either one of these three proposed methods: silicone oil dilution, hexane dilution, or using

two different commercially available PDMS whose refractive indices can vary from 1.408 to 1.429.

3.2 Theoretical Design

The optical modes propagating in the rib waveguide structure are too complicated to be determined using the ray tracing method (section 2.2.2) and therefore have to be deduced by solving the Maxwell equations in order to find the specific solution which satisfies all boundary conditions and has a fixed spatial distribution along the propagation direction. The details of this method are presented in the next sub-section.

3.2.1 Maxwell Equations for optical waveguides

As light travels in an optical rib waveguide of very small dimensions, the ray theory description of light becomes inaccurate and must be explained instead by the wave theory based on the electromagnetic field relationships expressed in Maxwell's equations. The Maxwell equations for a dielectric optical waveguide take the form

$$\nabla \times \mathbf{E} = -\frac{\partial \mathbf{B}}{\partial t} \tag{24}$$

$$\nabla \times \mathbf{H} = \frac{\partial \mathbf{D}}{\partial t} \tag{25}$$

$$\nabla \bullet \mathbf{D} = 0 \tag{26}$$

$$\nabla \bullet \mathbf{B} = 0 \tag{27}$$

where **E** is the electric field vector and **H** is the magnetic field vector.

Also, the electric flux density **D** and the magnetic flux density **B** are related to the field vectors by the relationship

$$\mathbf{D} = \varepsilon\mathbf{E} \tag{28}$$

$$\mathbf{B} = \mu\mathbf{H} \tag{29}$$

Consider an homogenous and lossless dielectric optical waveguide, realized in a material whosepermittivity and permeability can be treated as $\varepsilon = \varepsilon_0 n^2$ and $\mu = \mu_0$, where ε_0, μ_0 are the values in vacuum (ε_0=8.854×10^{-12}F/m and μ_0=4π×10^{-7}H/m) and n is the refractive index. Hence, the Maxwell's equation for optical waveguide wave analysis can be simplified as

$$\nabla \times \mathbf{E} = -\mu_0 \frac{\partial \mathbf{H}}{\partial t} \tag{30}$$

$$\nabla \times \mathbf{H} = -\varepsilon_0 n^2 \frac{\partial \mathbf{E}}{\partial t} \tag{31}$$

By taking the curl of equation (31) and given $c = \frac{1}{\sqrt{\varepsilon_0 \mu_0}}$, the wave equation can be obtained as

$$\nabla \times (\nabla \times \mathbf{E}) = -\frac{1}{c^2} \frac{\partial^2 \mathbf{E}}{\partial t^2} \tag{32}$$

The electromagnetic field of light propagating in the optical waveguide can be obtained by solving the exact solution of the Maxwell equations with the given boundary conditions of the optical waveguide. Each mode of the waveguide is a specific solution of the equations. In order to fully solve and analyzethe rib waveguide, numerical methods such as Finite Element Analysis, Finite Difference Time Domain (FDTD) and Beam Propagation Method (BPM) can be employed to solve the equations. On the other hand, the simpler analytical effective index method helps to solve the equations in a faster manner and can be used as an approximate solution to the PDMS rib waveguide.

3.2.1.1 The analytical effective index method

The analytical effective index method requires the basic understanding of the slab waveguide structure as shown in Figure 9. The Maxwell equations for the optical mode propagating in the *z*-direction can be rewritten using the electric field and magnetic fields expressed in the form of $\mathbf{E} = |\mathbf{E}|(x, y)e^{j(\omega t - \beta z)}$ and $\mathbf{H} = |\mathbf{H}|(x, y)e^{j(\omega t - \beta z)}$ where $|\mathbf{E}|$ and $|\mathbf{H}|$ are the field amplitudes, ω is the angular frequency ($\omega = 2\pi f$) and the mode propagating in the *z*-direction with propagation constant β, and obtain the following six equations:

$$\left.\begin{aligned} \frac{\partial E_z}{\partial y} + j\beta E_y &= -j\omega\mu_0 H_x \\ -j\beta E_x - \frac{\partial E_z}{\partial x} &= -j\omega\mu_0 H_y \\ \frac{\partial E_z}{\partial y} - \frac{\partial E_x}{\partial y} &= -j\omega\mu_0 H_z \end{aligned}\right\} \quad (33)$$

$$\left.\begin{aligned} \frac{\partial H_z}{\partial y} + j\beta H_y &= j\omega\varepsilon_0 n^2 E_x \\ -j\beta H_x - \frac{\partial H_z}{\partial x} &= j\varepsilon_0 n^2 E_y \\ \frac{\partial H_z}{\partial y} - \frac{\partial H_x}{\partial y} &= -j\omega\varepsilon_0 n^2 E_z \end{aligned}\right\} \quad (34)$$

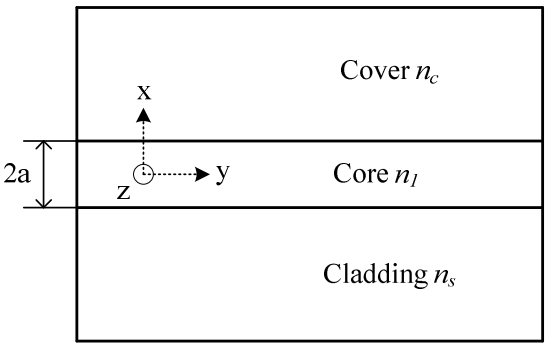

Figure 9: Slab optical waveguide.

For the slab waveguide structure, the *x*-axis is normal to the waveguide plane and the waveguide is infinitely long along the *y*-axis. Hence, the **E** and **H** are *y*-independent. In addition, both of them vary with *z* for an optical mode propagating along the *z*-axis as exp(*iβz*) and thus the *y* and *z* can be removed from the derivatives using

$$\frac{\partial \mathbf{E}}{\partial y} = 0\,,\ \frac{\partial \mathbf{H}}{\partial y} = 0\,,\ \frac{\partial \mathbf{E}}{\partial z} = i\beta\mathbf{E}\,,\ \frac{\partial \mathbf{H}}{\partial z} = i\beta\mathbf{H}$$

The six equations can be reduced to two distinct sets of linearly polarized solutions, known as the transverse electric (TE) and transverse magnetic (TM) modes. The TE mode satisfies the following wave equation

$$\frac{d^2E_y}{dx^2} + (k^2n^2 - \beta^2)E_y = 0 \tag{35}$$

and the magnetic fields are related to E_y as

$$H_x = -\frac{\beta}{\omega\mu_0}E_y \text{ and } H_z = -\frac{j}{\omega\mu_0}\frac{dE_y}{dx} \text{ where } E_x = E_z = H_y = 0$$

Conversely, the TM mode satisfies the following wave equation

$$\frac{d}{dx}\left(\frac{1}{n^2}\frac{dH_y}{dx}\right) + (k - \frac{\beta^2}{n^2})H_y = 0 \tag{36}$$

and the electric fields are related to H_y as

$$E_x = \frac{\beta}{\omega\varepsilon_0 n^2}H_y \text{ and } E_z = -\frac{j}{\omega\varepsilon_0 n^2}\frac{dH_y}{dx} \text{ where } E_y = H_x = H_z = 0$$

The propagation constant and electromagnetic fields for both TE and TM modes can be obtained by solving equations (35) and (36). For a uniform refractive index in the core and considering that the guided electromagnetic fields are confined in the core and exponentially decay in the cladding, the electric field distribution is taken as

$$E_y = \begin{cases} A\cos(\kappa a - \phi)e^{-\sigma(x-a)} & \text{for } (x>a), \\ A\cos(\kappa x - \phi) & \text{for } (-a \le x \le a), \\ A\cos(\kappa a + \phi)e^{-\xi(x+a)} & \text{for } (x<-a), \end{cases} \tag{37}$$

where κ, σ and ξ are wavenumbers along the x-axis in the core and cladding, and are given by

$\kappa = \sqrt{k^2 n_1^2 - \beta^2}$, $\sigma = \sqrt{\beta^2 - k^2 n_0^2}$ and $\xi = \sqrt{\beta^2 - k^2 n_s^2}$. The electric field, E_y and the magnetic field component H_z are continuous at the boundaries of core-cladding interfaces ($x = \pm a$) and based on $H_z = -\frac{j}{\omega\mu_0}\frac{dE_y}{dx}$ from equation (35), the following equations can be obtained

$$\tan(u + \phi) = \frac{w}{u} \text{ and } \tan(u - \phi) = \frac{w'}{u} \tag{38}$$

where $u = \kappa a$, $w = \xi a$ and $w' = \sigma a$. From equation (38), the eigenvalue equations can be found as

$$u = \frac{m\pi}{2} + \frac{1}{2}\arctan\left(\frac{w}{u}\right) + \frac{1}{2}\arctan\left(\frac{w'}{u}\right) \text{ and}$$
$$\phi = \frac{m\pi}{2} + \frac{1}{2}\arctan\left(\frac{w}{u}\right) - \frac{1}{2}\arctan\left(\frac{w'}{u}\right) \tag{39}$$

where $m = 0, 1, 2, \ldots$

From equations (37) and (38), the normalized transverse wavenumbers u, w, and w' are related by the following equations

$$u^2 + w^2 = k^2 a^2 (n_1^2 - n_s^2) \equiv v^2 \tag{40}$$

$$w' = \sqrt{\gamma v^2 + w^2} \text{ and } \gamma = \frac{n_s^2 - n_0^2}{n_1^2 - n_s^2} \tag{41}$$

where v is the normalized frequency and given as $v = kn_1 a\sqrt{2\Delta}$, and γ is a measure of the asymmetry of the cladding refractive indices (between cover and substrate). The values u, w, w', φ and β can be solved from the eigenvalue equations for a given wavelength of the light signal and geometrical parameters of the waveguide.

The *effective index* which is expressed as $n_e = \frac{\beta}{k}$ must satisfy the following condition for the optical field to be confined in the core region,

$$n_s \le n_e \le n_1 \tag{42}$$

and the optical field becomes a nonguided (or radiation mode) when $n_e < n_s$.

For a rib waveguide structure as shown in Figure 8b, the wave equation for the mode is given by equations (35) and (36). The basic assumption of the effective index method is that the equation of (36) can be expressed with the separation of variables as

$$H_y(x, y) = X(x)Y(y) \tag{43}$$

Substituting (43) into (36) and dividing it by $X(x)Y(y)$, the equation becomes

$$\frac{1}{X}\frac{d^2X}{dx^2} + \frac{1}{Y}\frac{d^2Y}{dy^2} + (k^2 n^2(x, y) - \beta^2) = 0 \tag{44}$$

By adding and substracting the y-independent value of $k^2 n_{eff}^2(y)$ into equation (44) and separating the equation into two independent equations one obtains

$$\frac{1}{X}\frac{d^2X}{dy^2} + (k^2 n^2(x, y) - k^2 n_{eff}^2(y)) = 0 \tag{45}$$

$$\frac{1}{Y}\frac{d^2Y}{dx^2} + (k^2 n_{eff}^2(y) - \beta^2) = 0 \tag{46}$$

where $n_{eff}(y)$ is called the *effective index distribution*. The height of the rib s takes the following values depending on the position on the y, $s = H + h$ for $0 \le |y| \le a$ and $s = h$ for $|y| > a$. Using the boundary condition that $H_z = \frac{dE_y}{dx}$ and from the continuity condition for dX/dy to be continuous at $x = 0$, d, $d+s$ in the three layer slab waveguides, the dispersion equation can be expressed as

$$\sin(\kappa d - 2\phi) = \sin(\kappa d)e^{-2(\sigma s + \psi)} \tag{47}$$

where $\phi = \arctan\left(\frac{\sigma}{\kappa}\right), \psi = \arctan\left(\frac{\sigma}{\gamma}\right)$ and

$\kappa = k\sqrt{n_c^2 - n_{eff}^2}$, $\sigma = k\sqrt{n_{eff}^2 - n_s^2}$, $\gamma = k\sqrt{n_{eff}^2 - n_{air}^2}$.

The solution of equation (47) with $s = H+h$ ($0 \le |y| \le a$) gives the *effective index*, $n_{eff}(H+h)$ and $s = h$ ($|y| > a$) gives the *effective index*, $n_{eff}(h)$ as shown in Figure 10.

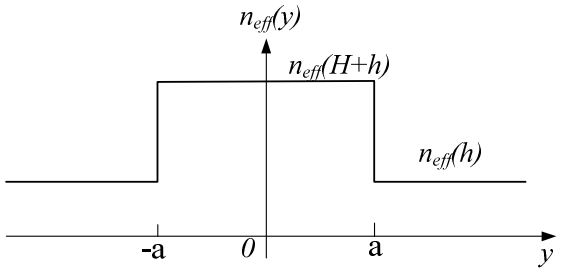

Figure 10: Effective index distribution $n_{eff}(y)$.

Thus, solutions of the wave equation in (46) can be calculated for each and every layer of the three layer symmetrical slab waveguide in the *y*-direction with $n_{eff}(H+h)$ and $n_{eff}(h)$ with satisfying of the boundary conditions at $y = \pm a$.

3.2.1.2 The Finite Element Method (FEM)

The method adopted here for the vector wave analysis of the guided modes in the three dimensional PDMS optical rib waveguide is the Finite Element Method (FEM) using the transverse electromagnetic field components. By introducing the Fourier Transform of $\widetilde{\mathbf{E}}(\omega) = \int_{-\infty}^{\infty} \mathbf{E}(t) e^{i\omega t} dt$ and using the identity $\nabla \times \nabla \times \widetilde{\mathbf{E}} \equiv \nabla(\nabla \bullet \widetilde{\mathbf{E}}) - \nabla^2 \widetilde{\mathbf{E}} = -\nabla^2 \widetilde{\mathbf{E}}$, equation (32) can be expressed as a three dimensional scalar wave equation of the form, which is often termed as the Helmholtz equation

$$\nabla^2 \widetilde{\mathbf{E}} + n^2 k^2 \widetilde{\mathbf{E}} = 0 \tag{48}$$

Hence, considering the transverse electromagnetic field in the *xy*-plane, the Helmholtz equation can be written into a Cartesian coordinate system and takes the form

$$\begin{bmatrix} P_{xx} & P_{xy} \\ P_{yx} & P_{yy} \end{bmatrix} \begin{bmatrix} E_x \\ E_y \end{bmatrix} = \beta^2 \begin{bmatrix} E_x \\ E_y \end{bmatrix} \tag{49}$$

where the polarization dependency of the waveguide modes is $P_{xx} \neq P_{yy}$ and the polarization coupling between the modes is $P_{xy} \neq 0$, $P_{yx} \neq 0$. For the rib waveguide structure, the minor component of the solution can be ignored by decoupling the mode with $P_{xy} = 0$ and $P_{yx} = 0$. This means the propagating mode is easily deduced by solving two equations:

$$P_{xx} E_x = \beta^2 E_x \text{ and } P_{yy} E_y = \beta^2 E_y \tag{50}$$

3.2.1.3 Finite Difference Time Domain method (FDTD)

The FDTD method is an alternative approach that directly solves Maxwell's equations by discretization of both time and space domains. Equations (30) and (31) can be rewritten as

$$\frac{\partial \mathbf{H}}{\partial t} = -\frac{1}{\mu}\nabla \times \mathbf{E} \tag{51}$$

$$\frac{\partial \mathbf{E}}{\partial t} = -\frac{\sigma}{\varepsilon}\mathbf{E} + \frac{1}{\varepsilon}\nabla \times \mathbf{H} \tag{52}$$

The discretization increments along the x, y and z directions can be represented with Δx, Δy and Δz. A centered difference form is adopted to discretize equations (49) and (50), which become

$$\frac{\mathbf{E}^{j} - \mathbf{E}^{j-1}}{\Delta t} = -\frac{\sigma}{\varepsilon}\mathbf{E}^{j-\frac{1}{2}} + \frac{1}{\varepsilon}\nabla \times \mathbf{H}^{j-\frac{1}{2}} \tag{53}$$

$$\frac{\mathbf{H}^{j+\frac{1}{2}} - \mathbf{H}^{j-\frac{1}{2}}}{\Delta t} = -\frac{1}{\mu}\nabla \times \mathbf{E}^{j} \tag{54}$$

where $t = (j - 1)\Delta t$, with j the iteration number while Δt represents the increment in time and the centered difference points for the electric field $\mathbf{E}$ are taken at $j - 1$ and j.

Hence, the $\mathbf{E}^{j-1/2}$ in equation (53) can be approximated by

$$\mathbf{E}^{j-\frac{1}{2}} \cong \frac{\mathbf{E}^{j} + \mathbf{E}^{j-1}}{2} \tag{55}$$

and reduces equation (51) to

$$\frac{\mathbf{E}^{j} - \mathbf{E}^{j-1}}{\Delta t} = -\frac{\sigma}{\varepsilon}\frac{\mathbf{E}^{j} - \mathbf{E}^{j-1}}{2} + \frac{1}{\varepsilon}\nabla \times \mathbf{H}^{j-\frac{1}{2}} \tag{56}$$

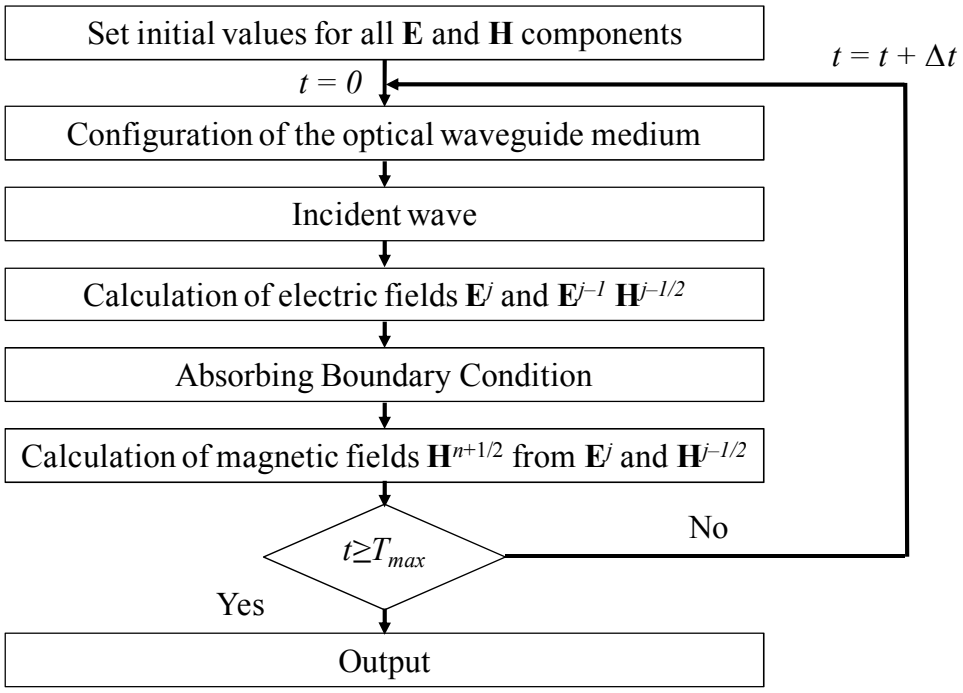

Figure 11: Flow Chart of FDTD analysis.

The expression $\mathbf{E}^j$ and $\mathbf{H}^{j+1/2}$ can be solved from equation (54) and (56) as

$$\mathbf{E}^j = \frac{1-\frac{\sigma\Delta t}{2\varepsilon}}{1+\frac{\sigma\Delta t}{2\varepsilon}}\mathbf{E}^{j-1} + \frac{\frac{\Delta t}{\varepsilon}}{1+\frac{\sigma\Delta t}{2\varepsilon}}\nabla\times\mathbf{H}^{j-\frac{1}{2}} \tag{57}$$

$$\mathbf{H}^{j+\frac{1}{2}} = \mathbf{H}^{j-\frac{1}{2}} - \frac{\Delta t}{\mu}\nabla\times\mathbf{E}^j \tag{58}$$

The electric and magnetic field components are located at specific points and are half-step offset each calculation in both space and time domain. The flow chart of the FDTD analysis is shown in Figure 11.

3.2.1.5 Beam Propagation Method (BPM)

A specific type of FDTD solutions is the BPM. BPM is a practical method which solves the electric field or the magnetic field of the light propagating in the waveguide. The electric field can be separated into two parts: a slowly varying envelope term $E(x,y,z)$ and a rapidly varying term $\exp(-jkn_c z)$, i.e. it is expressed as

$$E(x,y,z) = E(x,y,z)\exp(-jkn_c z) \tag{59}$$

where n_c is the refractive index in the cladding. Substituting equation (59) in the scalar wave equation (or the Helmholtz equation) in equation (48), the expression takes the form

$$\nabla^2 E - j2kn_c \frac{\partial E}{\partial z} + k^2(n^2 - n_c^2)E = 0 \tag{60}$$

Assuming the weakly guiding condition, the term $(n^2 - n_c^2)$ can be approximated to be $2n_c(n - n_c)$ and equation (60) can be rewritten as

$$\frac{\partial E}{\partial z} = -j\frac{1}{2kn_c}\nabla^2 E - jk(n - n_c)E \tag{61}$$

Hence, the right-hand side contains two terms: the first term represents free-space light propagation in a medium having the refractive index n_c and the second term represents the guiding function of the region with the refractive index *n(x,y,z)*. Both terms affect the light simulateously and can be assumed to be separable in the BPM analysis. In each small increment Δz the electric field is propagated in free space for a distance $\Delta z/2$ and the phase retardation due to the entire length Δz. Then, the electric field is propagated in free space for a distance of $\Delta z/2$. By repeating these same steps over the entire length, the light propagation can be calculated.

3.2.1.6 Comparisons of FEM, FDTD and BPM

The selection of the appropriate numerical method for a given task is important as each method, namely FEM, FDTD or BPM has its own strengths and weaknesses. An ideal method would score well in the computational time, computational memory usage, numerical aperture of the device (or the range of angle that can be accurately propagated), the refractive index contrast,

reflections in the device, non-linearity, dispersive material (where the refractive index vary with wavelength), arbitrary shape and the capability to implement absorbing boundary conditions [78].

FEM solves the optical waveguide in the frequency domain while the FDTD solves it in the time domain. FEM involves searching the roots of an eigenvalue equations formed by the discretization of matrix. Hence, the common problems associated with initial-guess are inevitable because such method has poor accuracy near and below the cutoff region which has large residue near the boundary. The second difficulty is the appearance of spurious or extraneous non-physical mode in the solutions. Unlike the FEM, FDTD solves Maxwell's equations in the time domain through explicit iterations with the required frequency domain information. Thus, the solution by FDTD is more accurate as compared with FEM.

However, one of the limitations is the longer computational time required by FDTD for its regular rectangular smaller grid for high resolution. FEM speeds up the computational by the reduction of the grid size locally and also follow the contours of a structure. In addition, FEM allows general geometry with arbitrary profile E_x and E_y in the traverse directions and has the flexibility and versatility for complicated structure, arbitrary shape, arbitrary refractive index profile and even anisotropy. Hence, the FEM offers a faster and more accurate solution for rib waveguide structure with minimum three refractive indices.

FDTD and FEM become increasingly time-consuming as the device cross-section or length increases. For devices with large length, BPM becomes attractive because of its axial algorithm which assumes that the light travels in

one direction. The key idea of BPM is to remove the fast varying term from the field and then solve only the slow varying field which reduces the computational time and memory. It works well for modeling waveguide components such as tapers and Y-junction with modest refractive index contrast and small angle of propagation. Arrayed waveguide grating can also be solved with the enhanced wide-angle BPM algorithm for increased accuracy of its off-axis propagation. Nonetheless, BPM has limited success for bi-directional simulations for reflections due to low speed and stability problems. FDTD works well for large refractive index contrast such as silicon waveguide and large numerical aperture device while BPM is suitable for large dimension devices with modest refractive index contrast such as polymer waveguide with small numerical aperture.

3.2.2 Single-mode PDMS waveguides

In order to study the single-mode PDMS waveguide, an extensive simulation effort has been performed with the above mentioned numerical methods in order to determine the effect of the geometrical dimensions on the mode propagation. Single-mode silicon-on-insulator rib waveguides (typically of width ≈ 5 μm) have been proposed initially by Soref *et al*. [79]. Based on mode matching calculations, the group has put forward an expression related to their geometry as shown Figure 8b to guarantee that they satisfied the single-mode condition

$$\frac{W}{H} \le \alpha + \frac{r}{\sqrt{1-r^2}} \qquad \text{for } 0.5 \le r \le 1.0 \tag{62}$$

where r = R/H is the ratio of slab height (h) to overall rib height (H), W/H is the ratio of waveguide width to overall rib height, and α = 0.3 by empirically

fitting. Later on, Pogossian *et al.* [80] suggested a more stringent value of $\alpha = 0$ based on an analytical effective-index design method. However, Lousteau *et al.* [81], using a full-vectorial beam propagation method, has demonstrated that this simple expression is insufficient to ensure single-mode behavior in rib waveguides. In addition, these analyses were limited to shallow rib height and did not provide enough information for deep ribs of large height ($r < 0.5$). Hence, Chan *et al.* [82] extended the studies of single-mode condition for deep ribs ($r<0.5$) of small width (~1μm or less). Although these works have revealed some guidelines for the design of single-mode rib waveguides, they are limited only to SOI waveguides with a different set of refractive indices operating at near infrared wavelengths. Hence, a comprehensive calculation and simulation of the waveguide has to be carried to obtain single-mode PDMS rib waveguide geometrical parameters with sizes on the order of a few micrometers ($W > 5$ μm). Furthermore, the single-mode rib waveguide should exhibit single-mode behavior with low propagation loss in the visible light range for the application of absorption spectroscopy.

In this thesis, the single-mode simulation was performed using FEM in Apollo Photonics Software™ for a rib waveguide using pure PDMS ($n = 1.412$) as core and modified PDMS ($n = 1.411$) as cladding. A second set of simulations was repeated for PDMS ($n = 1.429$) as core and PDMS ($n = 1.412$) as cladding. The simulations were carried out at a wavelength of 635 nm for fundamental, second and third order modes. The waveguide width (W) and rib height ($H - h$) were kept constant. The slab height (h) was increased in steps of 10 nm until the fundamental order mode would be supported. Hence, the single-mode lower cutoff boundary could be found. As the slab height increased, the

leakage of the fundamental mode to substrate increased and eventually it became a non-bounded mode. Therefore, the upper boundary limit can be found when the effective index of the fundamental mode is lower than the cladding refractive index.

Figure 12 shows the TE and TM modes (overlapping in the graph) of the single-mode boundary for a low refractive index contrast waveguide 8 μm wide, and with rib heights of 3 to 8 μm with a step of 1 μm. It is instructive to plot the graph in a different way from earlier results, as the rib height can be related to the thickness of the SU-8 mold whereas the slab height is determined by the residual layer left after blading away or by spin coating the PDMS in the soft lithography fabrication method. All higher order modes have been confirmed as radiation modes as their mode profile studies shows leakage to the substrate and the effective index of the mode propagation is lower than the cladding refractive index. For high refractive index contrast, the lower boundary is at 0.5 to 0.6 μm and an upper boundary greater than the low refractive index contrast waveguide. Thus, it was confirmed that these PDMS rib waveguide designs exhibit single-mode behavior.

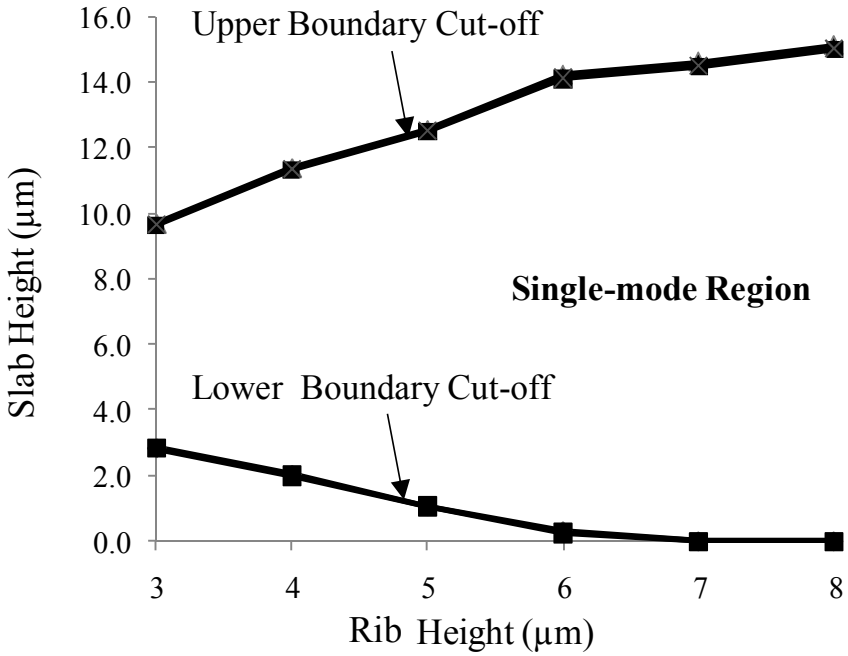

Figure 12: Single-mode region with cutoff boundary lines for an 8 µm width rib waveguide at an operating wavelength of 635 nm.

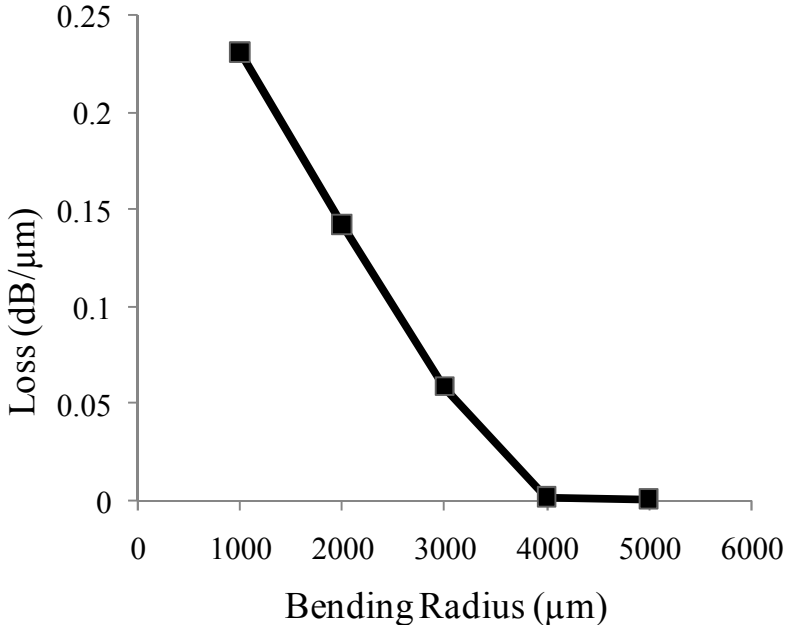

Figure 13: Bending radius loss for high refractive index contrast PDMS waveguide with 8 µm width, 4.5 µm rib height and 3.5 µm slab height.

The bending radius loss was simulated for the high refractive index contrast waveguides using FEM and a Y-branch power splitter was designed to demonstrate a more complex microphotonic device. Figure 13 shows the

bending radius loss for the high refractive index contrast and shows negligible loss for bending radius greater than 4000 μm.

3.2.3 Multi-mode PDMS waveguides

Multi-mode PDMS rib waveguides have large width, usually on the order of tens of micrometers. The large cross section of the waveguide in this case offers good light throughput and efficient coupling with light sources and detectors. Thus, multi-mode PDMS rib waveguides are also explored for lab-on-a-chip absorbance detection.

3.3 Fabrication

The PDMS waveguides are fabricated using an extended soft lithography technique that consists of two major steps; (1) Master mold preparation and (2) PDMS waveguide fabrication. The master mold was made of SU-8 photoresist (Microchem, NewtonMA, USA) spun on 8-inch silicon wafers. Three different types of PDMS waveguide fabrication techniques were proposed according to the refractive index modification techniques for the PDMS rib waveguide. The general procedure starts with patterning SU-8 photoresist for the master mold and is followed by coating anti-adhesion layer on it subsequently. Next, a thin layer of PDMS mixture was formed over the master mold for the waveguide core layer. Next, a lower refractive index cladding was fabricated over the core layer. The process was completed by releasing the PDMS rib waveguide from the master mold.

3.3.1 Preparation of SU-8 Master Mold

The master mold for the soft lithography was prepared by patterning a SU-8 negative photoresist (MicroChem, NewtonMA, USA). The fabrication steps of SU-8 photoresist are as follows [83]:

1. The substrate/wafers for SU-8 photoresist patterning should be thoroughly cleaned and dried prior to usage to obtain maximum process reliability and adhesion. This silicon substrate wafer was subjected to a Piranha (H_2SO_4 & H_2O_2) etch/clean followed by de-ionized water rinse and spin dry. The surface of the wafer was dehydrated in a convection oven for 200°C for 20 mins.

2. The SU-8 2007 was spin coated to the desired thickness according to the spin speed vs. thickness curve.

3. The resist was soft baked on a level hot plate to evaporate the solvent and densify the film. The process first began at 65°C and was ramped up to 95°C. The low initial bake temperature allows the solvent to evaporate out from the film at a controlled rate to produce better contour fidelity, reduced edge bead and improved resist to wafer adhesion.

4. Next, the resist was exposed to UV (350 – 400 nm) for cross-linking. The exposure time was optimized for a straight vertical profile. Over-exposure leads to T-topping profiles while under-exposure leads to catastrophic failure of resist.

5. Post-exposure baking (PEB) was necessary after exposure to selectively cross-link the area exposed. An initial bake temperature of 65°C was

ramp to 95°C. The low initial bake temperature is obligatory to ensure low stress induced during the cross-linking process.

6. The cross-linked SU-8 resist was developed with SU-8 developer by immersion under mild agitation to remove the uncross-linked resist. The developed SU-8 was rinsed with isopropanol and dried with N_2.

7. The patterned SU-8 photoresist was hard baked in a convection oven at 150°C for 20 minutes to further cross-link of the resist.

The SU-8 fabrication parameters for the realization of single-mode waveguide and multi-mode waveguides are shown in Table 2.

Process Step (Unit)		**Single-mode Waveguide**	**Multi-mode Waveguide**
SU8-Series		SU-8 2007	SU-8 2100
Spin Speed (rpm)		1000-1500	1000-1500
Soft Bake (mins)	65°C	1	5
	95°C	2	15
Exposure Dose (mJ/cm^2)		140-180	150-180
Post Exposure Bake (mins)	65°C	1	5
	95°C	2	15
Develop (mins)		2	5
Thickness (μm)		5-10	125-250

Table 2: Process Parameters for SU-8 Master Mold Patterning.

In the patterning of the SU-8 photoresist for optical mold, the exposure and PEB steps are critical in ensuring straight vertical profile and smooth surface sidewall. The patterned SU-8 was coated with a layer of fluorinated hydrocarbon by plasma decomposition of C_4F_8 gas to avoid PDMS stiction onto the SU-8 and also to reduce sidewall roughness. Alternatively, a monolayer of fluorinated silane can be deposited using chemical vapour deposition.

3.3.2 Refractive index modification of PDMS

The commercially available PDMS can be purchased from Dow Corning, Inc. (Sylgard 184) and Gelest, Inc. (OE-43). The refractive index of Sylgard 184 from Dow Corning is 1.412 whereas that of OE-43 from Gelest is 1.429. Hence, the two sources of PDMS can be employed directly in producing the core and cladding layer of the optical waveguide.

However, Sylgard 184 has been the preferred choice for the fabrication of microfluidic chip because of its lower cost and rapid protoyping. In comparison, OE-43 is ten times the more expensive than Sylgard 184 and requires a four times longer fabrication. Hence, it motivated us to fabricate both the core and cladding of the waveguide with Sylgard 184 by modifying its refractive index. Two methods of modification are presented. The refractive indices of the modified PDMS was measured using the prism coupling method (Model 2010, Metricon Corporation) with a refractive index accuracy of ± 0.0002 on a thin PDMS film spin-coated at 6900 rpm for 60 s.

The first proposed method is performed by adding silicone oil (200®, Dow Corning, Inc) to increase the refractive index of the Sylgard 184 PDMS. This method is able to increase the refractive index of pure PDMS from 1.412

with 0.010 when adding silicone oil upto a concentration of 10% w/w in to PDMS. A noticeable level of material non-uniformity was observed when more than 10% w/w amount of PDMS dilution with silicone oil is used.

The second proposed method consists of diluting Sylgard 184 with hexane. We surmised that the hexane dilution can decrease the refractive index of Sylgard 184. Indeed, the refractive index can be reduced by 0.001 in a modified PDMS with 10% w/w added hexane. It is suggested that the cross-linked PDMS macromolecules diluted with hexane form a guest/host matrix configuration. The hexane can be subsequently removed through evaporation by heating the cured PDMS at 90ºC for 1 hour (the boiling point of hexane is 78ºC). Thus, the evaporation of hexane resulted in a PDMS with numerous voids and a lower density.

3.3.3 Fabrication of PDMS optical layer

The PDMS rib waveguides with two different refractive indices were used to fabricate low refractive index contrast waveguides (Figure 14). Alternatively, high refractive index contrast waveguides can be produced directly from two commercially available PDMS (Figure 15).

As shown in Figure 14, the PDMS precursor mixture (Sylgard 184, Dow Corning) for low refractive index contrast was prepared at a weight ratio of base to curing agent 10:1 and split into two portions. One portion was further mixed with 10% w/w of hexane (Sigma-Aldrich, Inc.) to reduce its refractive index. The first precursor mixture of pure PDMS was poured on the SU-8 patterns to fill the trenches. The excess PDMS above the trenches was removed by blading it with clean room paper. Such method has been demonstrated by Ryu *et al.* to produce small features in PDMS with sized in the range of 5 μm.

[84] The blading process left a layer of PDMS on top of the SU-8 mold which formed the slab. Statistical studies of the slab height using microscope inspection showed it was 3 μm ± 1 μm thick and it is well within the acceptable region for single-mode region for the 8 μm width rib waveguide with rib height > 4 μm . The precursor mixture in the SU-8 trenches was allowed to settle down to a uniform layer and was thereafter cured at 80°C for 2 hours. The second precursor mixture with added hexane was subsequently poured to form a thin layer and cured at room temperature (25 ºC) for 48 hours. This second PDMS layer fused together with the first one and formed the waveguide cladding layer. A thick layer of pure PDMS had to be cured over this layer to prevent the chip from warping due to the compressive stress induced after the hexane evaporation. The amount of hexane was capped at 10% w/w because using a 20% w/w concentration showed no further decrease of the refractive index and produced severe warping after evaporation. The third layer of pure PDMS precursor mixture was then poured to form a thick substrate layer.

Figure 15 shows the fabrication process of the high refractive index contrast using OE-43 and Sylgard 184. For this high refractive index contrast waveguide, the PDMS precursor mixture (OE-43, Gelest) was prepared at a weight ratio of base to curing agent 1:1. This PDMS precursor has a lower viscosity as compared to the previous hexane-diluted method and allows spin coating on wafer to produce thin layers of PDMS, with a thickness down to 1 μm. The spin coated PDMS was cured at 55°C for 4 hours. Thereafter, the standard PDMS precursor mixture (Sylgard 184, Dow Corning) was cured over the thin layer of PDMS to form the cladding layer.

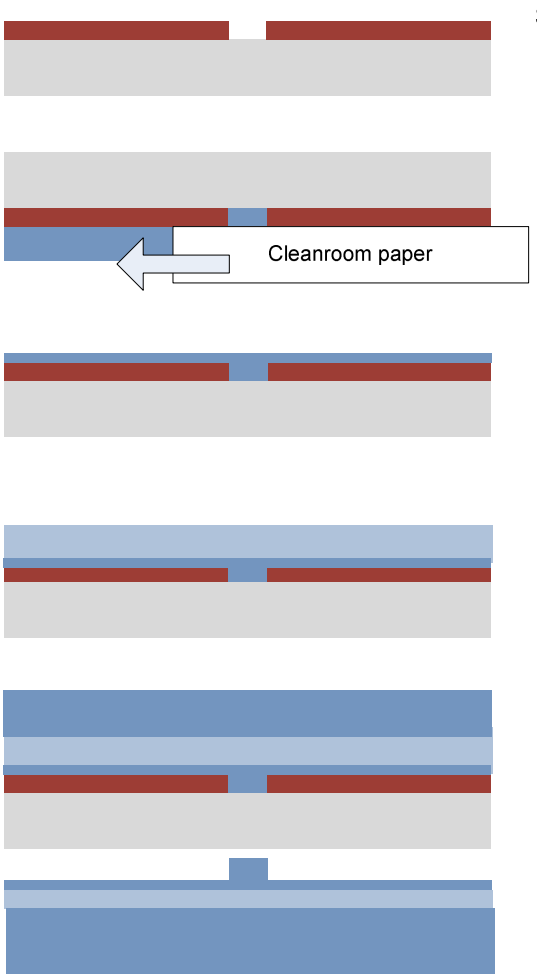

Step 1: SU-8 2007 photolithographically patterned

Step 2: Pure PDMS fills up trenches and the excess is wipe with cleanroom paper

Step 3: PDMS cured at 70˚C for 2 hours

Step 4: PDMS diluted in hexane poured and at room temperature for 48 hours. After curing, it is heated to 90˚C to remove the solvent

Step 5: Pure PDMS poured and thermally cured over second layer

Step 6: Final structure released

Figure 14: Schematic diagram of the fabrication method of the low refractive index contrast waveguide with hexane dilution.

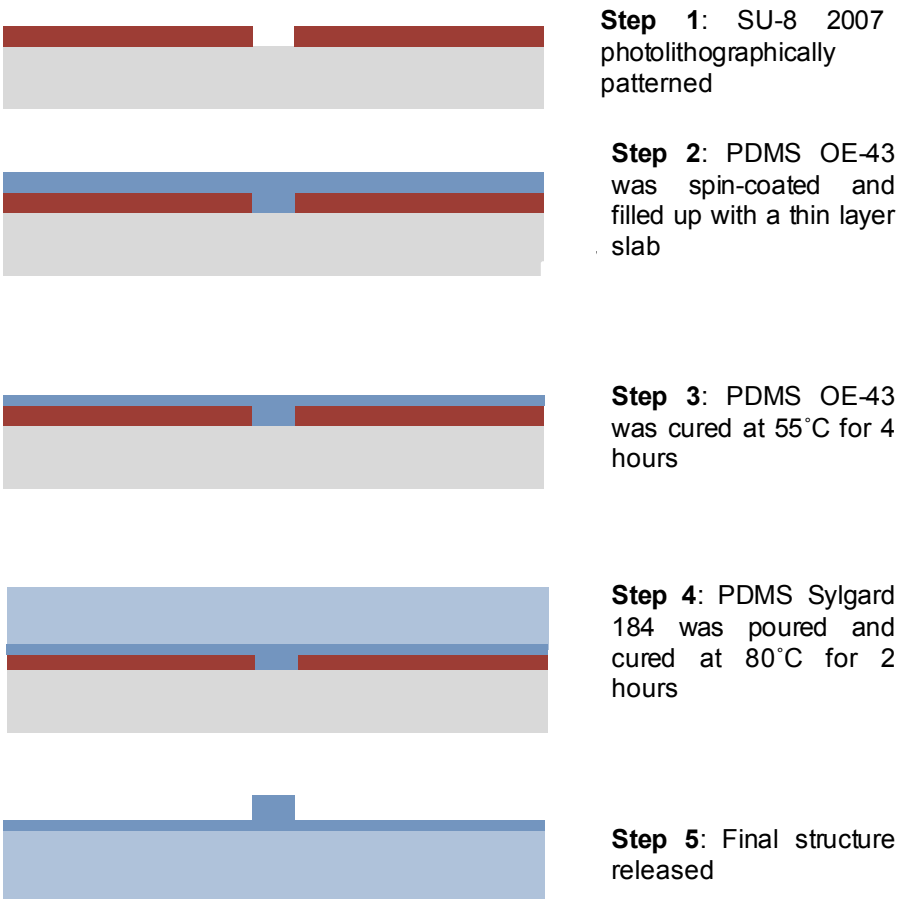

Figure 15: Schematic diagram of the fabrication process for the high refractive index contrast with OE-43 as core layer.

3.4 Experimental Setup

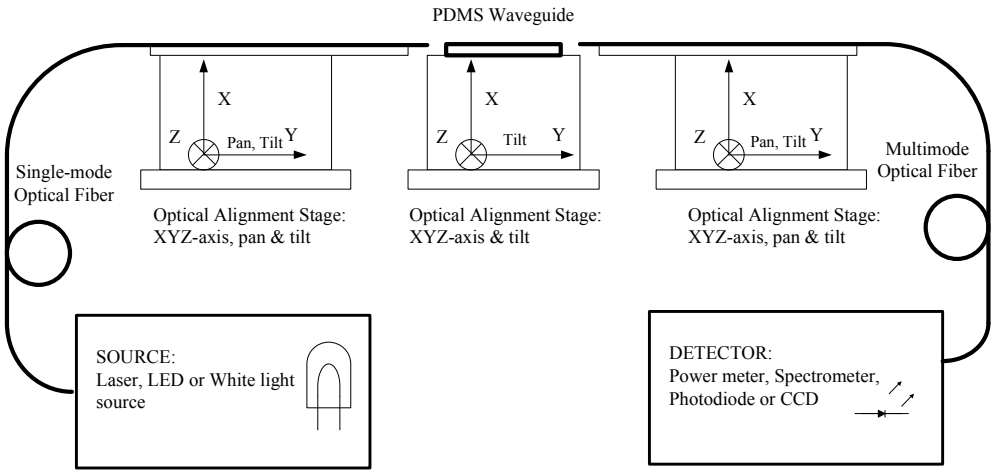

Figure 16: Experimental Setup for Waveguide Loss Characterization.

The experimental setup used to characterize the fabricated PDMS waveguides is shown in Figure 16. For the mode profile studies of the single-mode PDMS rib waveguide, a collimated diode laser beam of wavelength 640 nm (iFLEX 2000, Pointsource, Inc) was butt-coupled into the waveguide through a 9/125 μm single-mode optical fiber. The image of the output end of the waveguide was focused with a 50× objective lens and captured on a CCD camera (Exwave, Sony, Japan). The resulting image was analyzed using Origin Software™. The propagation losses of the waveguides were measured with a cut-back method in which the PDMS waveguides are cut-back from 7.5 cm to 2.5 cm in 4 steps. 10 measurements were taken and plotted for the loss calculations.

For the multi-mode waveguide characterization, the 125 μm fiber optic was properly aligned and butt-coupled with the PDMS waveguides to send and collect light from the waveguide. Silicone oil type 200® Fluid (Dow Corning Inc.) was applied at the fiber-waveguide interface to match their refractive indices and thereby reduce coupling losses. The optical fibers were then connected to the source and detector via Ocean Optics coupler. The light source was a turquoise light emitting diode (LED) type ETG-5CE490-15 (ETG, Inc.) with a 491 nm peak emission wavelength powered by 150 mA current pulses with 1 kHz frequency and 10% duty cycle. The photocurrent from the SFH 213 silicon photodiode (OSRAM, GmbH) was demodulated using the pulses powering the LED as a reference. The output signal from a demodulator was filtered by a low-pass filter of 4th order with 2 Hz cut-off frequency [85]. This modulation/demodulation technique improved the signal-to-noise ratio by several orders of magnitude and also suppressed the influence of ambient light

and other sources of noise. The resulting signal was recorded by a DPO 7054 oscilloscope (Tektronics, Inc.) and each measurement was repeated three times.

The multi-mode waveguide was characterized for propagation loss with increasing length from 2 to 18 mm in step of 2 mm. In addition, the insertion and transition losses of the multi-mode waveguide were also determined.

A Y-branch splitter was designed and fabricated based on the single-mode PDMS rib waveguide. The Y-branch was tested for splitting the power in the single-mode waveguide to a ratio 1:1 into both branching arms for two cases, namely a branch gap of 20 µm and of 50 µm.

3.5 Results and Discussion

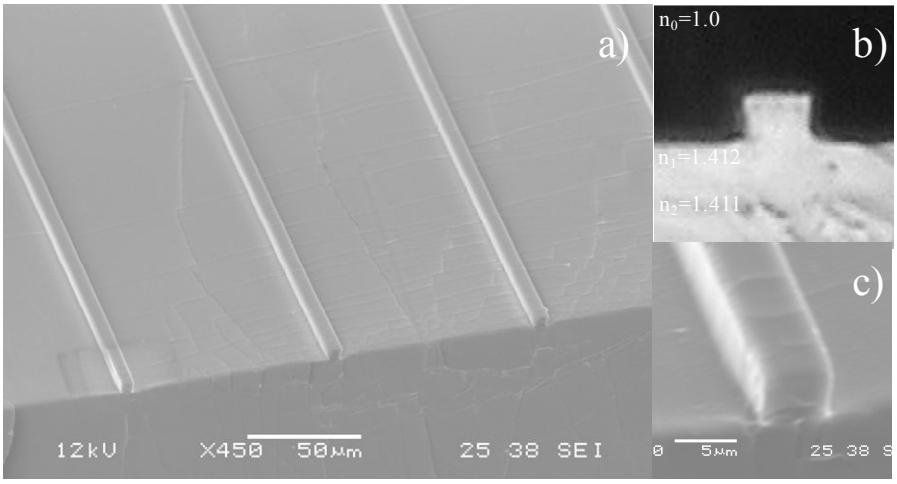

Figure 17: Images of single-mode rib waveguides fabricated in PDMS: a) SEM image of an array of waveguides; b) Microscope image of the face end of waveguide c) SEM image of a single rib waveguide.

Figure 17 shows the SEM images and microscope images of the fabricated single-mode waveguides. The distribution of the mode fields resulting from FEM and confirmed with BPM simulations for a PDMS rib waveguide 8 µm wide, with 6.8 µm rib height and 3.4 µm slab height are shown in Figure 18a.

From the pictures shown in Figure 18a, it can be observed that only the fundamental mode is bounded whereas the 2nd order mode is a radiation mode.

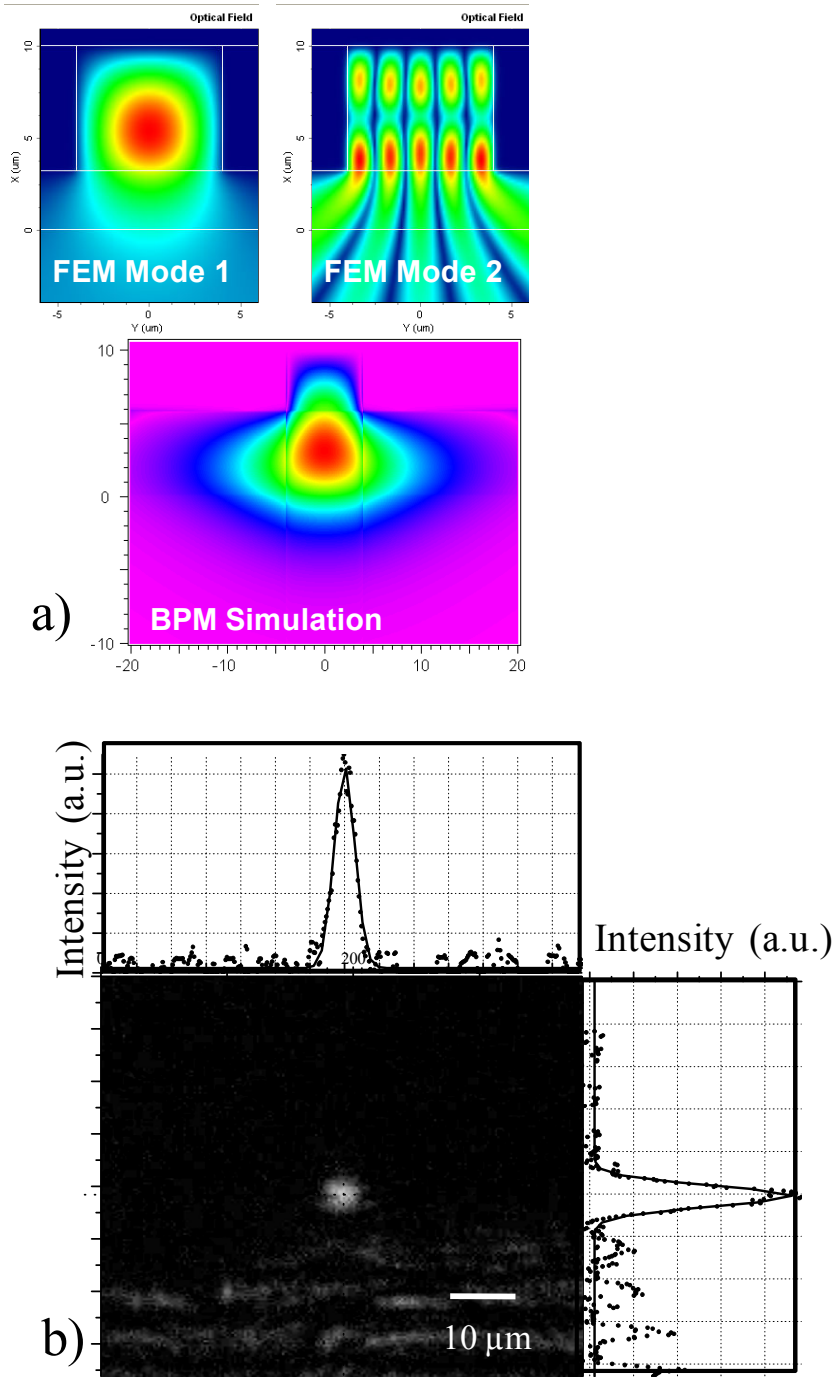

Figure 18 Beam profile studies on straight PDMS single-mode rib waveguides at a *z*-position of 5.5 cm: a) Simulation results of both FEM for mode 1 & 2 and BPM; b) Face end image of output waveguide captured by CCD.

The near-field pattern at the output of the waveguide was also studied, and the resulting cross-sectional intensity profiles in the *xy*-plane are shown in Figure 18b. The Gaussian-fit diameters of the intensity profiles were approximately 8.9 μm in the *x*-direction and 8.8 μm in the *y*-direction. These Gaussian diameters agree well with the simulated results of 9.14 μm in the *x*-direction and 9.15 μm in the *y*-direction and thus confirmed that the waveguide works essentially as a single-mode waveguide at the wavelength of 635 nm.

Next, we evaluated the propagation loss of both types of PDMS rib waveguides. The intensity of the mode profile captured at the waveguide end was measured as a function of the length of the waveguide to determine the propagation loss and the results are shown in Figure 19. The measured propagation loss of the single-mode waveguide at the wavelength of 635 nm was 0.48 dB/cm for low refractive index contrast waveguides (Δ=0.07%) and 0.2 dB/cm for high refractive index contrast waveguides (Δ=1.18%).

The propagation loss in a straight optical waveguide is generally attributable to absorption in the material and scattering losses due to the inherent roughness of the waveguide's sidewall. PDMS has a low absorption and the simulation results indicated that the mode radiation loss should be in the order of only ~0.2 dB/cm. Therefore, the higher propagation loss measured in our low refractive index contrast PDMS single-mode waveguide might be due to the scattering from the sidewall roughness of the waveguide and low confinement factor in the waveguide [86, 87] . This loss can be minimized through further optimization of the mold used in the soft lithography fabrication process. In addition, the improvement of light confinement in the waveguide

reduces the propagation loss as shown in Figure 19 by the high refractive index contrast waveguides.

The intercepts of 7.91 dB and 4.11 dB for both the high refractive index and low refractive index contrast waveguide can be attributed to the coupling loss. The main cause is the Fresnel reflection with the mode mismatch. Moreover, the larger coupling loss in high refractive index contrast waveguide is related to the NA of the optical fiber which does not match the waveguide properly.

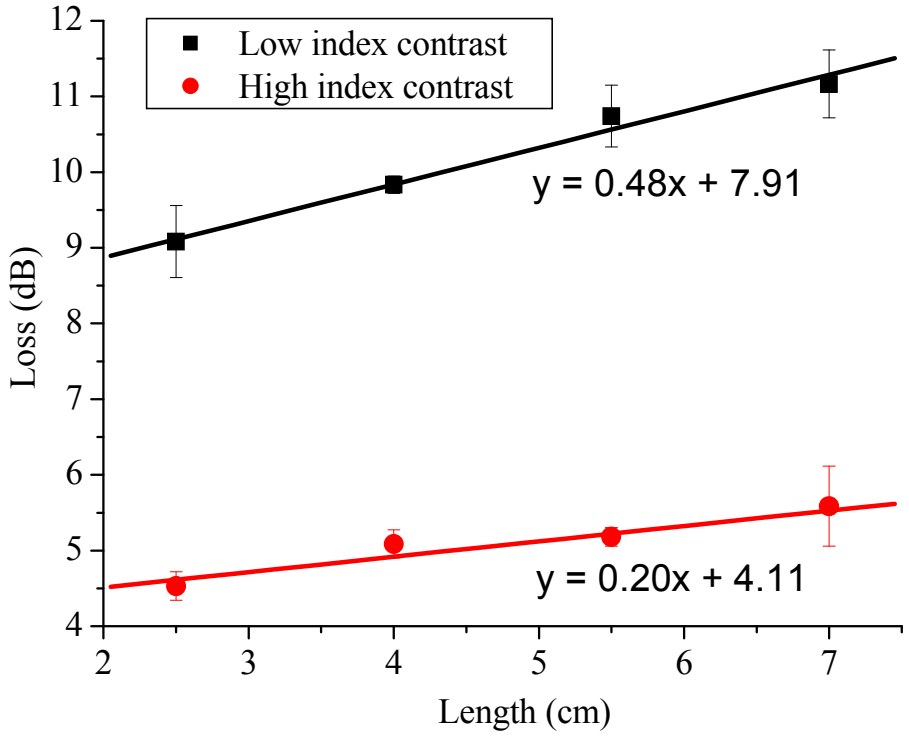

Figure 19: Measured propagation loss at λ = 635 nm for both the low t and high refractive index contrast PDMS single-mode rib waveguides.

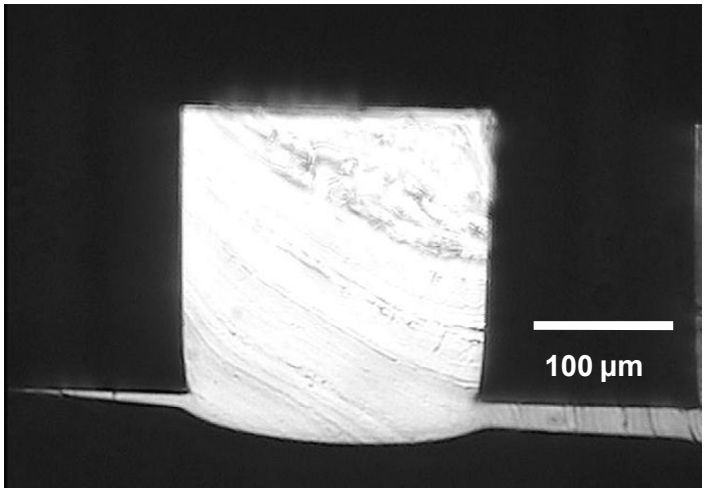

Figure 20 Microscope image of the face end of the PDMS waveguide

The fabricated mutli-mode PDMS rib waveguide is shown in Figure 20. The optical or insertion losses through a multi-mode rectangular waveguide can be separated into three main components: propagation, radiation, and transition losses. Each of these losses for the PDMS rib waveguides have been characterized and presented in plots in Figure 21, Figure 22 and Figure 23.

The propagation loss along a straight waveguide typically arises from scattering of light due to its sidewall roughness. Also, some of the light can be directly absorbed by the waveguide material itself. For straight PDMS waveguides, the propagation loss is found to be increasing almost linearly (R^2 = 0.979) with the waveguide length at a rate of 0.249±0.015 dB/cm (Figure 21).

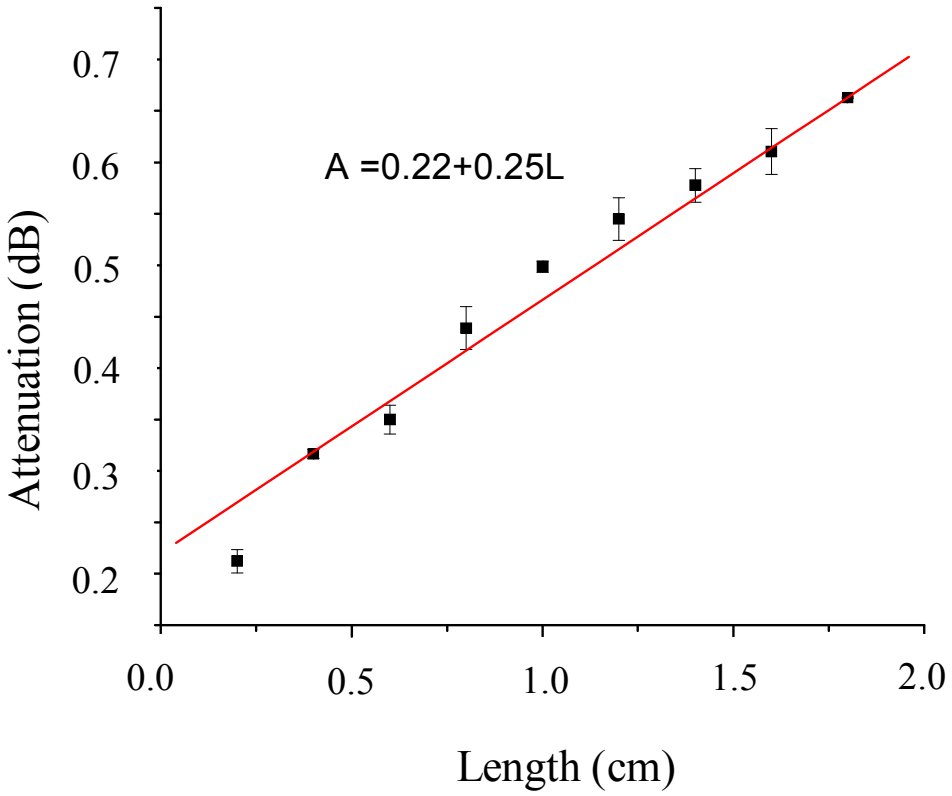

Figure 21: Propagation loss of the multi-mode PDMS waveguide measured at λ = 491 nm.

The intercept of 0.226±0.018 dB can be attributed to coupling losses between the PDMS waveguide and optical fibers. Coupling losses arise from Fresnel reflection which occurs when there is a considerable mismatch in the refractive indices of the waveguide and optical fibres. Mode mismatch as a result of cross-sectional differences (round versus rectangular) also contributes to the coupling loss. The former has been addressed by applying an index-matching fluid, silicone oil, between the waveguides and optical fibers.

The attenuation rate of 0.249±0.015 dB/cm measured at 491 nm for our PDMS multi-mode waveguide is lower than some of the values reported in literature for other polymer waveguides: >0.25 dB/cm for the photodefinable epoxy below 550 nm [88] and >7 dB/cm for the SU-8 waveguides at below 500 nm [89]. The propagation loss also depends on the modal wavelength,

increasing inversely with the wavelength as high-frequency waves get scattered more due to sidewall roughness [90]. Our PDMS multi-mode waveguides present a low attenuation partially due to their reduced sidewall roughness after coating the SU-8 template with a fluorinated hydrocarbon layer. Sidewall surface profiling by atomic force microscopy revealed a roughness of 30 nm and 10 nm for the PDMS waveguides prepared respectively before and after coating of the SU-8 template. A further explanation for the lower propagation loss can be given by a relatively large size of the guiding medium. It is known that larger waveguides exhibit reduced propagation losses. The presented waveguides having a square cross-sectional width of 250 μm are at least several times larger than those cited. For instance, PDMS waveguides with a size about half that of our waveguides have a reported attenuation rate of 0.40 dB/cm at a wavelength of 460 nm [91]. However, this report is based on the destructive cut-back method whereas, light-scattering striations of the cut-back method was avoided here by directly moulding PDMS waveguides at various lengths.

Radiation loss is encountered because curved waveguides are not capable of supporting perfectly bound modes. As a result of leaky modes, energy is being constantly radiated along the curvature of the waveguides. The amount of radiation depends on the waveguide radius of curvature, waveguide size, and the refractive index contrast between the core and cladding. A low index contrast, which is common in polymer waveguides, requires that the radius of curvature be increased in order to limit any radiation loss. The radiation loss in curved multi-mode waveguides, after being corrected for coupling and propagation losses, is presented in Figure 22 and, as expected, increases inversely with the radius of curvature. For curvatures below 0.4 cm

radius, radiation loss exceeds 1 dB and can be considerably larger than the corresponding propagation loss (<0.5 dB). However, once curvature radius exceeds 0.5 cm, both radiation and propagation losses become comparable. This characteristic is in agreement with the earlier reports in literature [92, 93, 94].

Transition loss occurs at the junction between straight and curved waveguides. Both waveguides support different modes and these modes mismatch as they meet. In a straight waveguide, the optical field is symmetrically centered whereas the field in a curved waveguide is displaced towards the outer curvature. For a large enough radius of curvature, the two fields align better, and the corresponding transition and radiation losses shall be minimal.

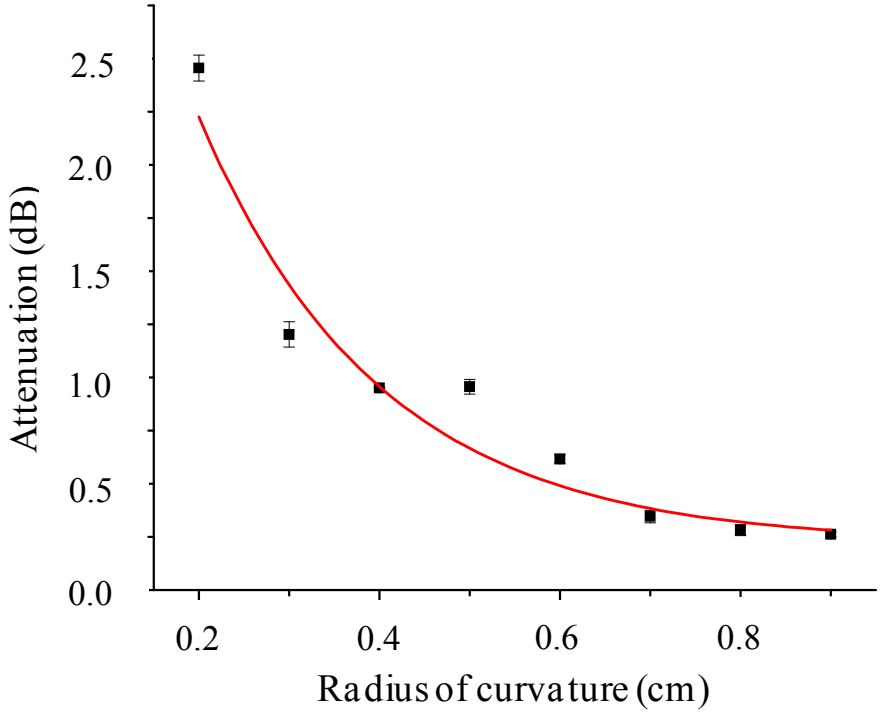

Figure 22: The measured radiation loss of the multi-mode PDMS waveguides.

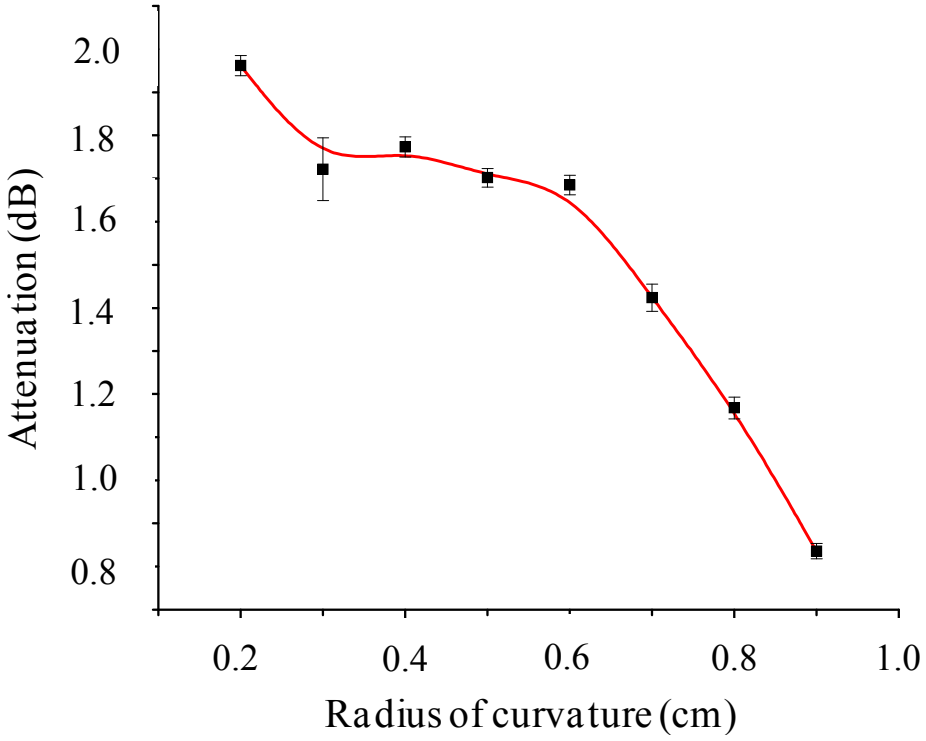

Figure 23: The measured transition loss of the multi-mode waveguide.

The transition loss of the multi-mode PDMS waveguides has been experimentally characterized and the results are shown in Figure 23. The transition loss is shown as a function of radius of curvature after being corrected for coupling, propagation and radiation losses. As the radius of curvature increases, the transition loss, outside the peculiar plateau region, declines linearly and lags the radiation loss which declines rather rapidly. For long waveguides, however, the propagation loss may surpass the sum of both transition and radiation losses.

The Y-branch power splitter demonstrated the feasibility of producing bending waveguides for complex microphotonics devices. The Y-branch had a linear branching length of 1 mm and was realized in 2 versions, with a branch gap of 20 μm and 50 μm, respectively. As shown in Figure 24, the output of the Y-branch allows the waveguide to split power equally (1:1) in both waveguide branches.

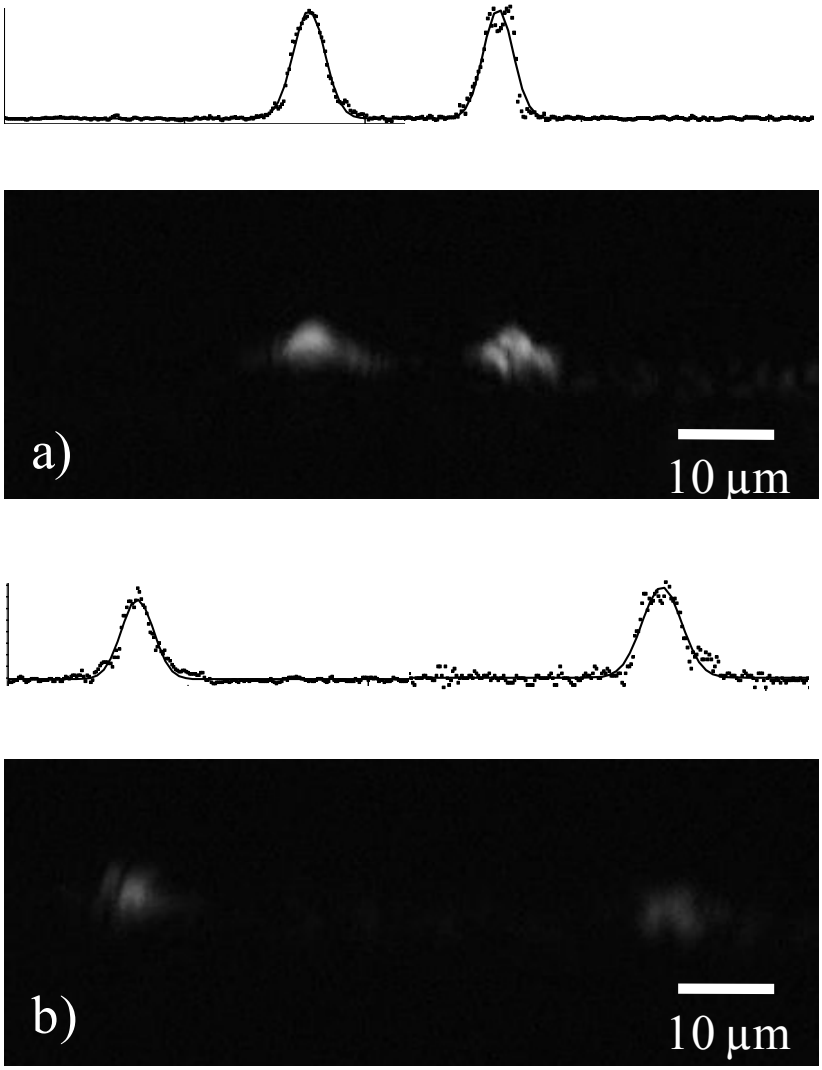

Figure 24: The mode profiles captured with a CCD for the Y-branch power splitter with a branch gap of: a) 20 µm, and b) 50 µm.

In this chapter, the design, fabrication and experiment of single-mode and multi-mode PDMS rib waveguides were presented. FEM, FDTD and BPM were employed to simulate accurately various configurations of PDMS rib waveguide. Simulations results have shown that by selecting the appropriate ratio of width to height and ratio of rib height to slab height, single-mode propagation can be generated even in a large cross section PDMS rib waveguide (> 5 µm).

The fabrication of single-mode PDMS rib waveguide was demonstrated to precisely control the slab height and rib height to form single-mode PDMS rib waveguide. The modifications of the refractive index contrast (Δ) of the PDMS were proposed with three methods; silicone oil dilution, hexane dilution or from two different commercially available PDMS and the refractive indices can vary from 1.408 to 1.429. The fabrication process of the PDMS waveguides involved surface-treated SU-8 master mold for the soft lithography and two steps curing for the formation of core and cladding layers.

The propagation loss of the single-mode waveguide was measured to be 0.48 dB/cm for low refractive index contrast waveguides (Δ=0.07%) and 0.20 dB/cm for high refractive index contrast waveguides (Δ=1.18%) at the wavelength of 635 nm. For the multi-mode PDMS waveguide, the propagation loss was measured to be 0.25 dB/cm.

In summary, both single-mode and multi-mode PDMS waveguide have been designed, fabricated, and characterization for their mode profile characteristic, insertion losses such as propagation loss, transition and radiation loss. The PDMS waveguide set up the basis for the construction of planar microspectrometer as well as the sensor for LOC spectrometer.

CHAPTER 4

POLY(DIMETHYLSILOXANE) ARRAYED WAVEGUIDE GRATING

The objective of this chapter is to report the realization of poly(dimethylsiloxane) (PDMS) arrayed waveguide grating (AWG) as a wavelength discrimination element for an integrated microspectrometer.

The design of a conventional layout PDMS AWG with four-channel output for operation in the visible light wavelength range is described. The device was designed for 1 nm channel spacing in a wavelength range from 639 to 644 nm. A second non-conventional layout PDMS AWG is then introduced, in order to provide a large free spectral range while operating at low diffraction order. The device was designed with an S-shape arrayed waveguides and produces 3 channel outputs for red, green and blue wavelength.

The fabrication methods for both type of PDMS AWGs (conventional and non-conventiona) are detailed. The measured transmission loss of the conventional PDMS AWG is shown in detail together with its polarization dependency, cross talk level and channel loss uniformity. The mode profile characteristics of both types of AWGs are also presented.

The fabrication related error and polarization dependency of the AWGs are investigated. Practical implementations of a PDMS AWG as a visible light spectrometer are discussed in detail.

Both type of PDMS AWGs are demonstrated for achieving high resolution and large free spectral range which serves as a potential candidate for

integration with microfluidics in a monolithic PDMS lab-on-a-chip device for visible light spectroscopy applications.

4.1 ARRAYED WAVEGUIDE GRATING FOR SPECTROSCOPY

The array waveguide grating (AWG), also known as the PHASAR, has been invented to be used as wavelength multi/demultiplexer in a wavelength division multiplexing (WDM)-based photonics network for telecommunication applications [95,96]. Since its inception, it has been demonstrated for high wavelength resolution, low insertion loss and high stability [97]. The implementation and usage of AWGs has been extensive, and mainly for telecommunication applications, such as production of multiwavelength light sources [98], tunable filters [99] and wavelength routing [100].

AWG have been fabricated using different types of materials. Many groups have reported the realization of AWG in various materials such as Silicon-on-Insulator (SOI) [101], Silica-on-Silicon [102] and Silicon-based Polymer Technology [103] for the infrared wavelength range in telecommunication applications. However, the realization of AWGs for operating in the visible light wavelength requires different type of materials which have high transparency in the visible light such as silica-based, silicon nitride and polymers such as PMMA and PDMS.

The attractive characteristics of AWGs have led to new applications other than those in telecommunications such as spectroscopy and chemical sensing [104]. A conventional spectroscopy equipment typically consists of a broad-band light source, a dispersive element, a focusing lens, a slit and a detector. However, such a structure is difficult if not impossible to monolithically integrate as-is in a single chip. The highly dispersive array

waveguides and focusing slab waveguides in AWG ease the integration of most the required elements (except the light source) on a planar substrate for wavelength separation in an integrated microspectrometer.

Spectroscopy for biological and biochemical samples is mostly performed in the visible light (400–700 nm) because a large portion of the bio/chemical spectroscopical signatures of interest lie in this wavelength range. Therefore, spectroscopy requires dedicated integrated photonic devices which are transparent and operable in the visible range. An AWG-based spectrometer for biochemical spectroscopy has been demonstrated in silica-on-silicon technology for usage in the visible range [104]. Silica has initially been chosen because it can be easily produced using well-established techniques in microelectronics. Nevertheless, AWGs made of silica are more costly than their polymer counterpart. Low cost polymer AWGs enable the realization of disposable biochips for reduced sample contamination. Moreover, polymer-based waveguide devices offer rapid processibility, high yields and high performance such as lower optical loss and smaller birefringence compared to silica as well as compactness owing to the large refractive index contrast [105].

4.2 ARRAYED WAVEGUIDE GRATING OPERATING PRINCIPLE

Figure 25 shows the schematic diagram of an AWG structure which consists of the input & output waveguides, the two concave slab waveguide star couplers (or free propagation region FPR), connected by an array of waveguides with a constant path length difference ΔL between adjacent waveguides.

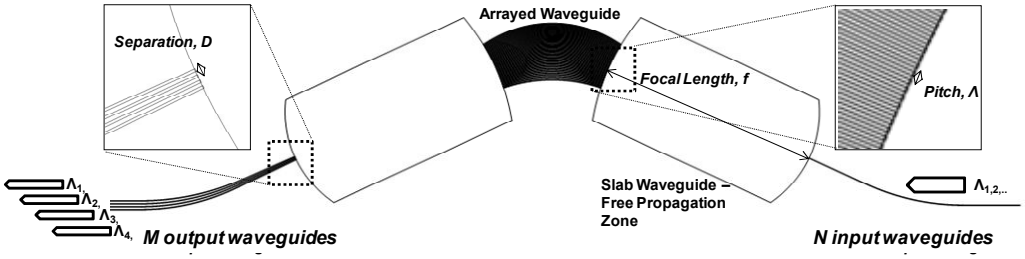

Figure 25: Schematic diagram of the arrayed waveguide grating with parameters.

As light enters the center of FPR from the input waveguides, light diffracts as it would be in free space, diverging and coupling into the arrayed waveguides. This diffracted field profile between the input waveguide and the slab waveguide is typically Gaussian where the *divergence half angle* can be estimated from the Gaussian diffraction formula. The Gaussian diffraction formula is given by [106]

$$\alpha = \frac{2\lambda}{\pi \omega n_{eff,s}} \tag{63}$$

where α is the *divergence half angle* or the angle between the light propagation direction and the Gaussian far field asymptote of the $1/e^2$ irradiance surface, ω is the *Gaussian beam waist* (mode diameter) in the input channel waveguide and $n_{eff,s}$ is the effective index of the slab waveguides.

The arrayed waveguide has been designed such that the constant path length difference ΔL between adjacent waveguides equals an integer multiple of the central wavelength λ_c. After light propagates through the arrayed waveguides, this central wavelength constructively interferes into one focal point at the center of the second FPR. The arrayed waveguides are positioned along a Rowland arc centered at the input waveguide-slab waveguide junction and with a radius equal to the focal length f of the FPR. Therefore, at the end of the

arrayed waveguide, the lights beams arrive with a phase difference between adjacent waveguides and that can be expressed as [107]

$$\Delta\varphi_{AWG} = \frac{2\pi(\Delta OPL)}{\lambda} = \frac{2\pi\Delta L n_{eff,a}}{\lambda} \tag{64}$$

where ΔOPL is the *Optical Path Length* difference and $n_{eff,a}$ is the *effective index*. The phase difference is chosen to be $2\pi m$ for the *central wavelength* λ_c resulting in constructive interference of order m between the wavelets emerging from the arrayed waveguide output aperture. Hence, the relationship between the order m and the constant length difference ΔL is given by [108]

$$m = \frac{n_{eff,a}\Delta L}{\lambda_c} \tag{65}$$

As the wavelength varies from the center wavelength, $\lambda_c + \Delta\lambda$, a linear phase change occurs across the waveguides of the array due to the constant path length difference between adjacent waveguides. This ultimately results in a tilted wavefront focused in a point shifted away from the center. Thus, by placing the output waveguide at a proper position along the Rowland arc, spatial separation of different wavelengths channels is produced.

For a wavelength deviating with $\Delta\lambda$ from the central wavelength, the maximum constructive interference condition is satisfied in direction θ with respect to the coupler axis when the total *optical path length* equals $m\lambda$, and can be written as,

$$\Delta OPL_s + \Delta OPL_a = m\lambda$$

$$n_{eff,s}\Lambda\sin\theta + n_{eff,a}\Delta L = m\lambda \tag{66}$$

where Λ is the waveguide pitch between the interface of the waveguide array and the FPR, $n_{eff,s}$ and $n_{eff,a}$ are the effective indexes of the slab and array

waveguides, respectively. Differentiating the above equation (66), the AWG *linear dispersion* in the focal region is obtained as [108]

$$\frac{dx}{d\lambda} = f\frac{d\theta}{d\lambda} = \frac{fN_c\Delta L}{\lambda_c n_{eff,s}\Lambda} \tag{67}$$

with $N_c = n_{eff,a} - \lambda\frac{dn_{eff,a}}{d\lambda}$.

The *free spectral range* (FSR), or the difference between two wavelengths diffracted into the same direction in successive order, is given by [106]

$$FSR = \frac{\lambda}{m} \tag{68}$$

and with a resolution

$$R = mN = \frac{OPD_{\max}}{\lambda} \tag{69}$$

where $OPD_{\max}$, is the optical path difference between the longest and shortest waveguides in the phase array.

4.2.1 Conventional PDMS AWG

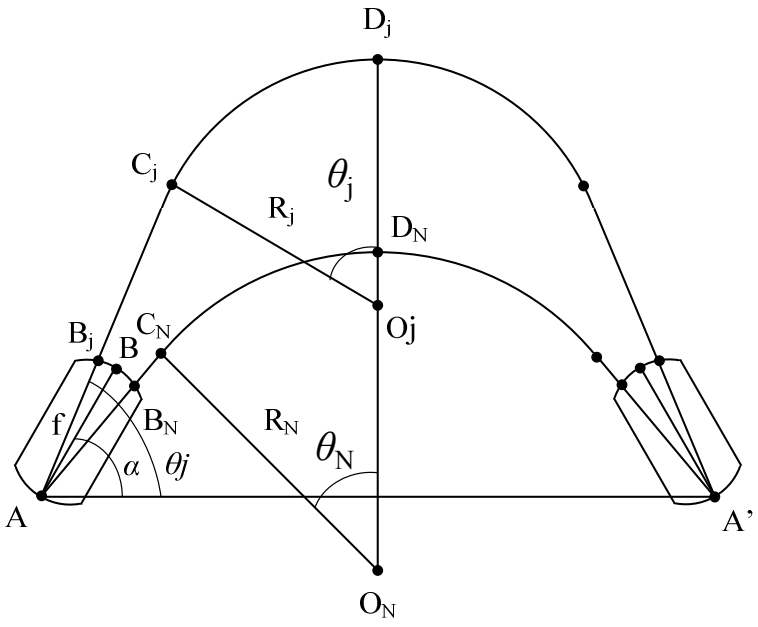

Figure 26: Schematic layout for the conventional AWG design.

Figure 26 illustrates schematically the layout of the conventional AWG. Each waveguide in the array consists of two equal but straight waveguides (one at the beginning/input, the other at the end/output) that are smoothly connected.The slab angle α with respect to the horizontal x-axis of the two FPRs , also simply called slab and the separation of the slab L_{slab} (distance between AA') are the design parameters.

The two basic equations for the layout design are

$$S_j + R_j\theta_j = S_N + R_N\theta_N + (N-j)\frac{\Delta L}{2} \tag{70}$$

$$(f + S_j)\cos\theta_j + R_j \sin\theta_j = \frac{L_{slab}}{2} \tag{71}$$

where S_j and S_N are the straight path lengths connecting B_jC_j and B_NC_N where j = 1…N. Both the straight S_j and curved waveguide $R_j\theta_j$ have different lengths and different tilt angle θ_j with R_j centered at different O_j. Equation (70) is the requirement for the path length difference of array waveguide. Equation (71) expresses the condition that the distance between point A and the center line is $L_{slab}/2$. The straight length S_N of the innermost waveguide should be determined for a minimum necessary straight length. From equations (70) and (71), R_j and S_j for j=1…N (where N is the number of arrayed waveguide) can be rearranged to obtain

$$R_N = \frac{L_{slab}/2 - (f + S_N)\cos\theta_N}{\sin\theta_N} \tag{72}$$

$$R_j = \frac{L_{slab}/2 - [f + S_N + R_N \cdot \theta_N + (N-j)\Delta L/2]\cos\theta_j}{\sin\theta_j - \theta_j\cos\theta_j} \tag{73}$$

$$S_j = S_N + (R_N \cdot \theta_N - R_j \cdot \theta_j) + (N-j)\frac{\Delta L}{2} \tag{74}$$

Equation (72), (73) and (74) give a total of 2N equations with 2N+1 unknown parameters (α, L_{slab}, S_1-S_N, and R_1-R_N). Hence, there are infinitely many solutions for the AWG parameters. Nonetheless, there also are a few restrictions to obey such as the minimum of R_j should be larger than the minimum bending radius R_{min}, the straight length of S_j should be larger than S_N, and the minimum array waveguide separation at the center line should be larger than the known value $\Delta y_{\min}$. The optimization of the AWG layout should result in short arrayed waveguide lengths to minimize phase errors due to refractive index fluctuations.

4.2.2 Non-conventional PDMS AWG

An AWG with a large FSR (~300 nm) is needed to cover the whole visible light range from 400 to 700 nm. Since $FSR \approx \lambda_c/m$, a low diffraction order ($m \leq 2$) is needed for the AWG to span the required large FSR at a central wavelength λ_c of 550 nm. Such a low diffraction order (i.e. small path-length difference between adjacent waveguide) causes the arrayed waveguides layout in the conventional AWG (shown in Figure 26) to overlap/merge each other and become indistinguishable from one another. This is because for a low diffraction order, the path length difference ΔL is small and the solutions to the equation (72), (73) and (74) will produce arrayed waveguides that crosseach other. In order to eliminate this problem a non-conventional shape has to be adopted for the AWG, such as the S-shape [109] or gull-wing shape [110].

The conventional shape AWG consists of two straight waveguides sections and a curved one. In contrast, the S-shape AWG has an asymmetrical arrangement with four straight and three curved waveguide sections, as shown in Figure 27. Part A and part B are identical in shape and size but are oriented

in opposite directions. In each part of A and B, there are 2 straight and one curved waveguide section. The waveguides in part A have equal length differences between neighbouring waveguides and are arranged in increasing length such that waveguide *N* is the shortest and waveguide *j* = 1 is the longest. The increasing length difference in part A will be cancelled out by the decreasing length difference in part B for each waveguide. Hence, each waveguide has the same total length in both parts A and B. In addition, the waveguides in part A have equal spacing between each other up to the intersection of OA. Similarly, the waveguides in part B have equal spacing between each other along their entire length from the FPR until the intersection with line OA'. Hence, the path length difference is only introduced by part C. In part C, all waveguides are concentric arcs (of same centre point and arc angle) with constant differences in the radius of curvature from one to another.

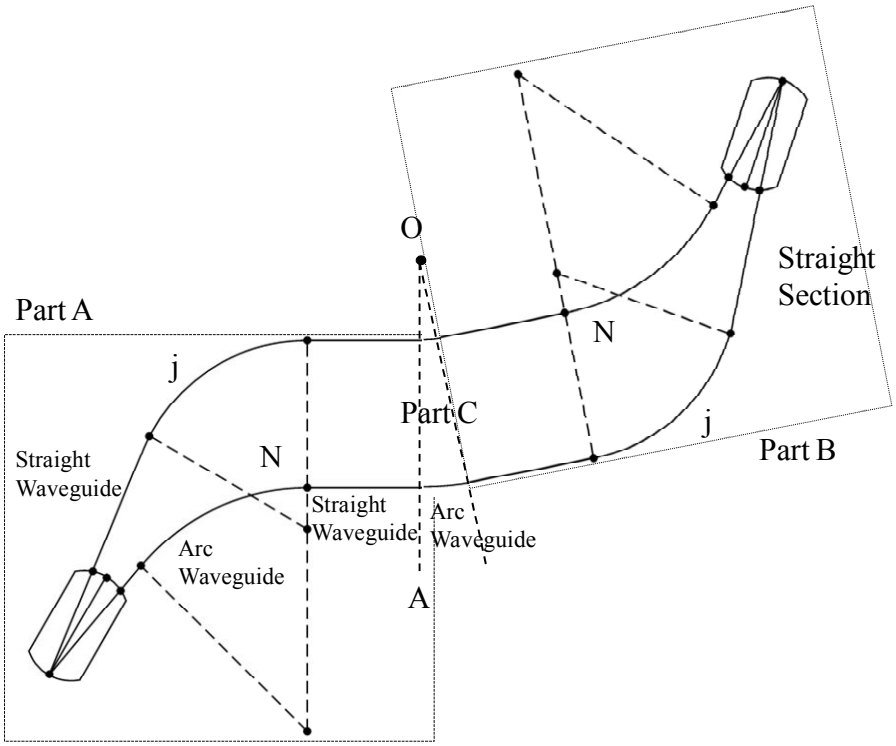

Figure 27: Schematic of the array waveguide layout for the S-shape AWG.

As shown in Figure 28a, three criteria have to be met in the design of the layout parameters; T_j, R_j and S_j for j=1…N (where N is the total number of arrayed waveguides in the AWG).

Firstly, the path length difference between adjacent waveguides must be constant and increasing from N to j and the relationship between adjacent waveguide can be written as,

$$T_j + S_j + R_j\theta_j = T_N + S_N + R_N\theta_N + (N-j)\Delta L \tag{75}$$

Secondly, the waveguides must be equally spaced at the intersection with line OA, and this is expressed as,

$$(f+S_j)\sin\theta_j + R_j(1-\cos\theta_j) = (f+S_N)\sin\theta_N + R_N(1-\cos\theta_N) + (N-j)\Delta y \tag{76}$$

Thirdly, the lateral distance of every waveguide path from the coupler point must be equal to one another. This distance L must be optimized together with the coupler angle α to minimize the overall dimension of the AWG. The third criteria can be written as,

$$(f+S_j)\cos\theta_j + R_j\sin\theta_j + T_j = L \tag{77}$$

From equations (75), (76) and (77), a total of 3N–2 equations have to be solved simultaneously with 3N+1 variables (S_1 – S_{N-1}, R_1 – R_N, T_1 – T_N, α and L). Hence, there are infinitely many solutions. However, by selecting an appropriate value of R_N (where all R must be larger than R_{min}) and optimizing α and L values, the number of variables is reduced to 3N–2. Thus, the set of solutions to the equations (75), (76) and (77), is unique.

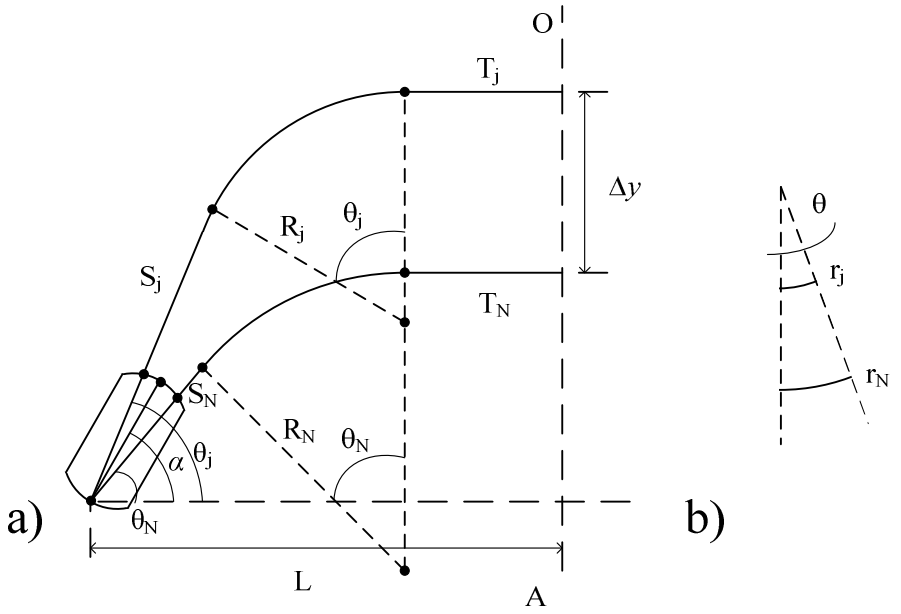

Figure 28 Schematic layout of the S-shape AWG highlighting its key geometrical design parameters: a) Part A & B, and b) Part C.

For the design parameters of part C shown in Figure 28b, the path length difference is introduced by the constant difference in radius of curvature between adjacent waveguides and is given as,

$$\Delta L = \Delta s = \theta \Delta y = \theta (r_N - r_j) \tag{78}$$

In determining the values of r_j (j=1…N), the restricting conditions necessitate that the gap (Δy) must be well separated to ensure that the waves propagating in each waveguide are well decoupled from each other and that all r_j are greater than R_{min} to reduce bending radius loss.

4.4 Design & Simulation

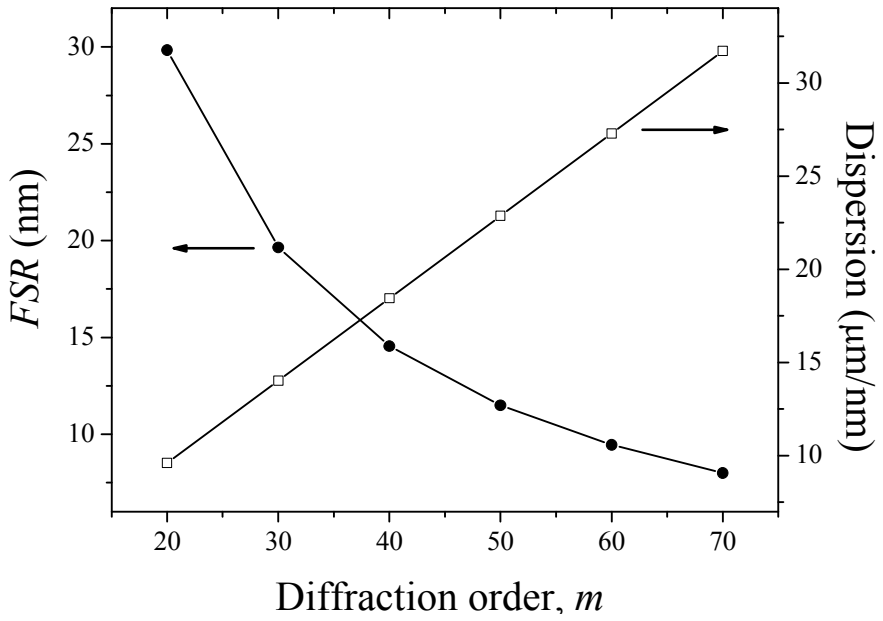

Figure 29: Relationship between free spectral range, dispersion and diffraction order for an AWG of pitch size of 5 μm, n = 1.41 and a focal length of 3 mm.

The main advantage of the conventional AWG is its very high resolution which is obtained by designing the device to work at a high diffraction order m in equation (78). The reason is that, based on equation (76), a high dispersion effect is produced by having a high m (or selecting large ΔL) in the AWG. However, a large ΔL (or m) compromises the FSR as governed by (77). The divergent requirements for the diffraction order m for achieving both high resolution and large FSR in a AWG for visible light spectroscopy is illustrated in Figure 29. Hence, the designs presented here seek to obtain two types of different AWG, namely the conventional type AWG for high resolution and the non-conventional S-shape AWG for large FSR.

4.4.1 Conventional shape AWG for nanometer resolution

The first step of designing the PDMS AWG is to produce single-mode PDMS waveguides as the first basic building block necessary for the ultimate realization of the AWG. The theoretical design and simulation of the single-mode PDMS rib waveguide was reported in Chapter 3. Both the rib height and width of the waveguide are 8 μm and the slab height of the waveguide is 4 μm. For the design of a PDMS AWG operating in the wavelength range of 639 to 644 nm, the high index contrast PDMS single-mode rib waveguide was utilized. A high index contrast waveguide is highly suitable for the demonstration of a AWG because of low bending radius loss. The refractive indices of core and cladding of the high index contrast waveguide are n_{core} = 1.429 and n_{clad} = 1.412. The effective index of the waveguide n_s, the group effective index n_g of the array and slab waveguides, respectively, were then determined using FEM method simulations of the waveguide. These results are necessary for the design of the PDMS AWG's geometrical parameters.

The general design procedures for a conventional PDMS AWG are as follows:

1. The number of output channels N was selected. As a proof-of-concept device, we selected 4 output channels.
2. The wavelength channel spacing $\Delta\lambda$ was selected. In order to demonstrate nanometer resolution sensing capability, a 1 nm wavelength separation was targeted.
3. The free spectral range FSR was calculated using the simple relation FSR = $N\Delta\lambda$. After considering an additional tolerance of ± 0.5 nm, a final value of 5 nm was the required FSR.

4. The diffraction order m was calculated as $m = integer(\lambda_c/FSR)$ which gives a value of 128. The central wavelength, λ_c of 641.5 nm was chosen to match the laser wavelength for characterization.
5. The length difference ΔL between the adjacent waveguides was calculated as $\Delta L=(m\ \lambda_c/n_{core})$ which gives a value of 57.4 µm.
6. The output waveguide pitch Δx and the array waveguide pitch Λ was selected to be as small as possible to create a compact AWG. The lowest limit of the pitch was constrained by the critical dimensions of the mask used in the fabrication process. On the other hand, the output waveguide pitch must be sufficiently large to provide isolation between neighbouring waveguides. The critical dimension of the mask is 5 µm. Nonetheless for a 8 µm wide waveguide, a gap of a 8 µm was preferred for its sharper features in the SU-8 photoresist mold.
7. The focal length of the FPR can be determined from the equation (67).

As a matter of fact, the above calculated length difference ΔL between adjacent waveguides does not produce the expected central wavelength at 641.5 nm due to the fact that the n_c is an approximate value of the true value of $n_{eff,a}$ as dictated by equation (67). Also, the calculated value of the focal length of the FPR, L_f with the minimum output waveguide pitch, Δx does not produce the desired channel spacing based on the equation (68). To solve equation (67) and (68), numerical solutions such as FDTD or BPM are mandatory to find the exact value of $n_{eff,a}$, $n_{eff,s}$ and N_c. In the AWG design, the parameters were simulated and optimized using the Apollo™ Photonics Solution Suite (APSS) software. The APSS first solved the waveguides based on FEM and FDTD to

obtain the necessary waveguide information. Thereafter, the BPM was used to solve the wavelength dependent response at the output waveguides.

The optimization algorithm for the search of the central wavelength involved the tuning of ΔL by step of 0.01 until the desired value was attained. Next, the channel spacing was tuned by changing the Δx and/or L_f. The optimum Δx and L_f values should generate the desired channel spacing with sufficient adjacent crosstalk (>20 dB) while keeping the overall layout size compact. Large adjacent channel crosstalk necessitates large L_f and Δx but at the cost of large chip size. Thus, L_f and Δx was optimized by first increasing the L_f to achieve the desired channel spacing and adjacent crosstalk at the minimum Δx of 16.0 μm. Then, Δx was increased gradually at the same time as L_f was reduced for smaller chip size while maintaining the required channel spacing with a tradeoff of the adjacent crosstalk. The final results of the parameter optimization are shown in Table 3: The values of the design parameters for the four-channel PDMS AWG..

The simulated insertion losses of the PDMS AWG for both the Transverse Electric (TE) mode and Transverse Magnetic (TM) modes are shown in Figure 30. It can be seen that the insertion losses for both the TE and TM modes show almost identical transmission spectrum peaks and position. The insertion loss is 3.6 dB at the transmission peak located at 641 and 642 nm and the adjacent crosstalk is >34dB.

Parameter	Value
Center wavelength λ_c (nm)	641.5
Channel spacing $\Delta\lambda$ (nm)	1
Channel number N	4
Number of array waveguide	24
Diffraction order m	128
Length difference ΔL	57.04
Output waveguide pitch Δx (μm)	17.4
Array pitch d (μm)	16.0
Focal length L_f (μm)	3000
Chip size (mm^2)	15 × 7.5

Table 3: The values of the design parameters for the four-channel PDMS AWG.

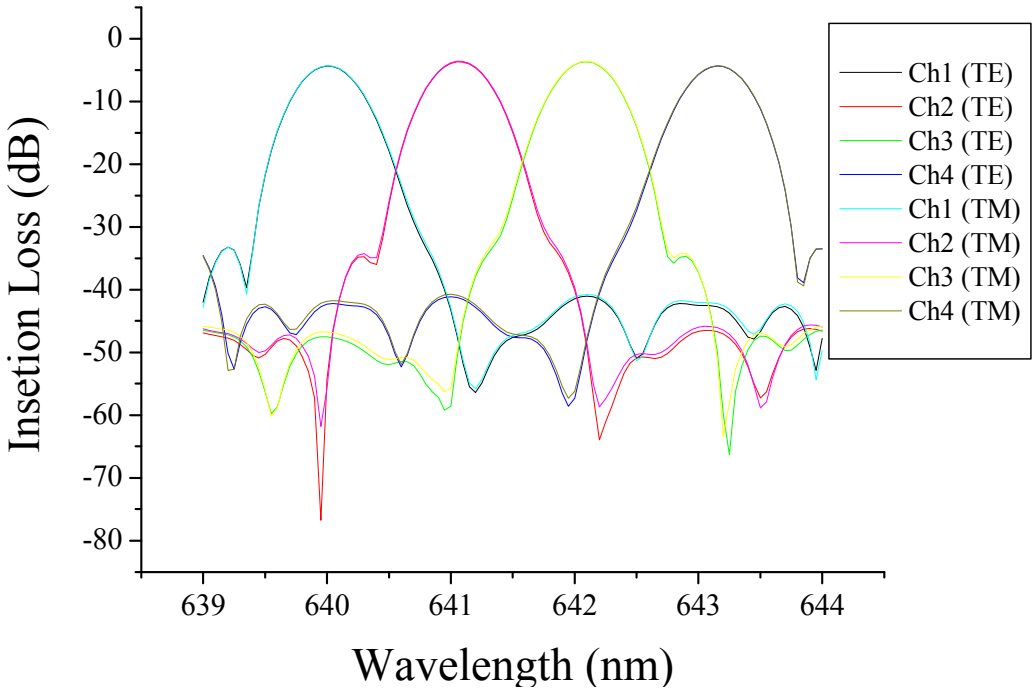

Figure 30: Simulation results of the 4 channel PDMS AWG as per design shown in Table 3.

The overall insertion loss of the AWG originates from the combined contribution of several factors, such as the FPR to array waveguides transition, the curvature of the waveguides, and the transition between straight to curved waveguides. The minimum bending radius of our AWG was kept at 4000 µm which has negligible loss (0.0018 dB/µm). The loss due to the transition between straight to bending waveguides was calculated to be 0.2 dB. Thus, the main contribution for the overall insertion loss comes from the FPR to array waveguide transition. An estimated 3 dB power loss was expected at this junction because our 8 µm wide array waveguides were separated laterally only by a gap of 16 µm from one another. Hence, an approximate 3 dB was expected at this junction. The mask layout is shown in Figure 31 with the input waveguide perpendicular to the output waveguide.

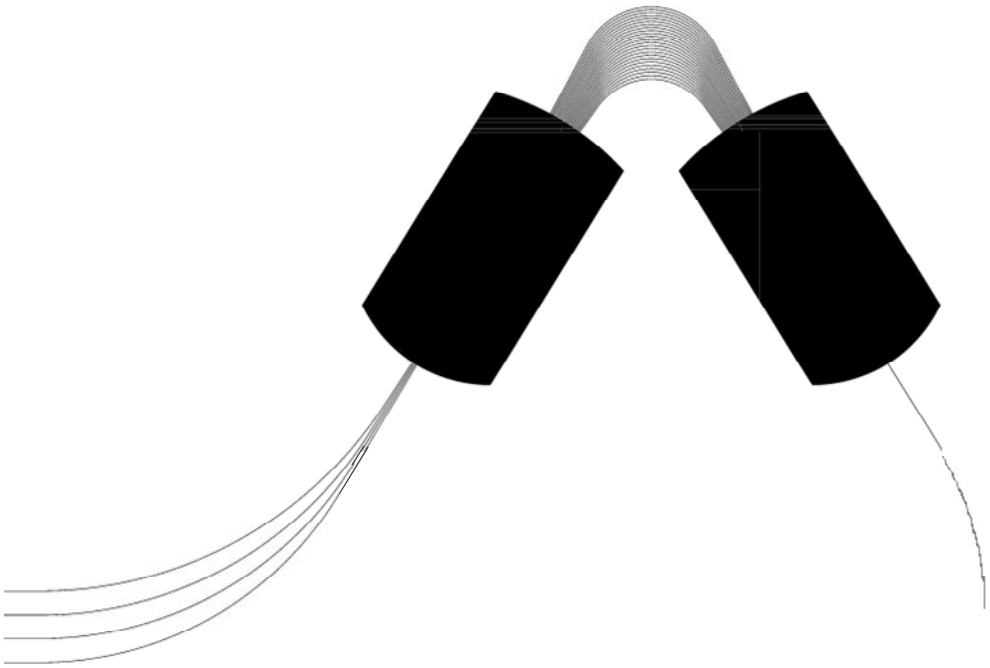

Figure 31: Mask layout of the fabricated conventional PDMS AWG with 1 input channel and 4 output channels.

4.4.2 Non-conventional S-shape AWG for large *FSR*

For the design of a PDMS AWG operating in the entire visible range from 400 to 700 nm (*FSR* = 300 nm), an S-shape AWG was employed, using high index contrast PDMS single-mode rib waveguides. The refractive indices of core and cladding of the high index contrast waveguide are n_{core} = 1.429 and n_{clad} = 1.412. As the path length difference was provided by the center arc section, the design procedures takes on a different approach.

The general design procedures for the S-shape AWG layout are as follows:

1. The number of output channels *N* was selected as 3 for demonstration of Red, Green and Blue (*RGB*) output.
2. The number of arrayed waveguides was selected as 7. Based on the Gaussian beam diffraction, equation (63) and with the BPM simulations, the focal length of the coupler was calculated for best coupling. As shown in Figure 32, the insertion loss of the center array waveguide increases while the peripheral array waveguide decreases as the coupler increases. The focal length was chosen to be more than 2100 μm and shows good coupling by the BPM field as shown in Figure 33.
3. The minimum gap spacing for proper decoupling was found to be 44.5 μm.
4. The parameters of part A and B are solved with MATLAB™ by optimizing R_j, α and L.
5. The θ in part C was selected as 1°. The r values are solved with the minimum gap spacing. Hence, the ΔL is calculated to be 0.776 μm with m = 2, resulting in a *FSR* of 275 nm.

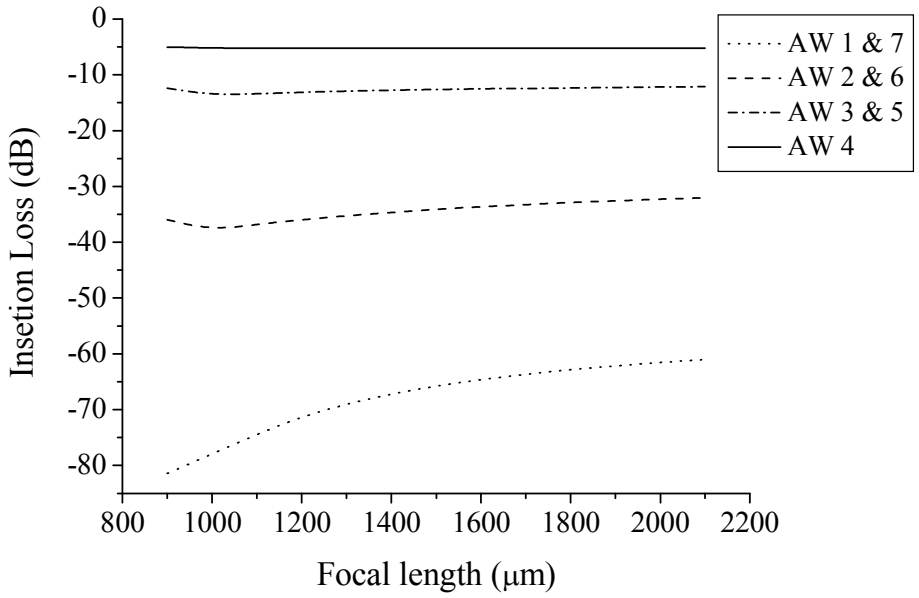

Figure 32: Insertion loss vs. focal length of the seven arrayed waveguides in a S-shaped AWG.

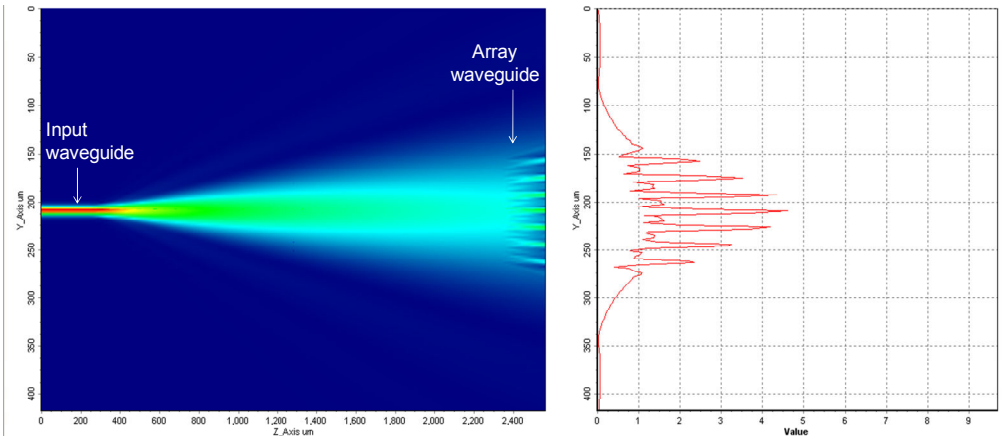

Figure 33: BPM simulation results of the 1st FPR where input waveguide launches a beam into an array of 7 waveguides.

The final parameters optimization is shown in Table 4. The layout of the final S-AWG is shown in Figure 34. The chip size is 13 mm × 19 mm.

Parameter	**Value**
Center wavelength λ_c (nm)	555
Channel spacing $\Delta\lambda$ (nm)	80
Channel number N	3
Number of array waveguide	7
Diffraction order m	2
Length difference ΔL	0.776
Output waveguide pitch Δx (μm)	16
Array pitch d (μm)	16
Focal length L_f(μm)	2100
Chip size (mm^2)	13 × 19

Table 4: The values of the design parameters for the S-shape PDMS AWG.

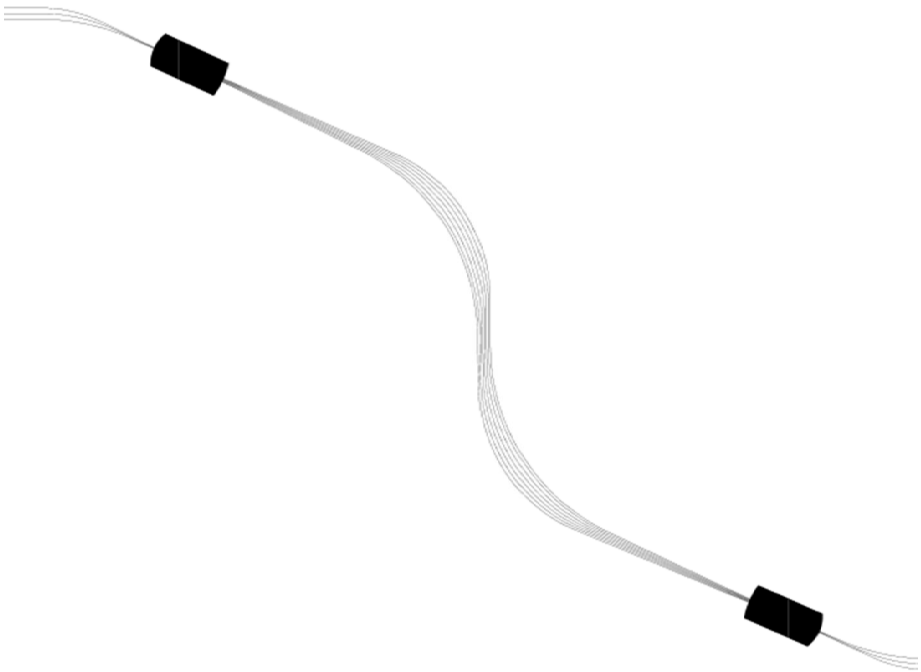

Figure 34: Mask layout of the S- shape AWG for large FSR.

4.5 Fabrication & Characterization

The fabrication of a single-mode PDMS rib waveguide was previously presented in chapter 3 and the fabrication of AWG is based on the same method. Therefore, only a short summary of the key aspects for the fabrication of the PDMS AWG is presented here.

The master mold for the soft lithography was prepared by patterning a 8 μm thick SU-8 2007 (MicroChem, NewtonMA, USA) photoresist spun on 8-inch silicon wafers. The exposure dose and duration for post-exposure bake steps were optimized for acceptable vertical sidewall profile and low surface roughness. The patterned SU-8 master mold was treated with a silane anti-stiction coating in a chemical vapor deposition (CVD) process to avoid sticking of the PDMS onto the SU-8 mold and also to reduce the sidewall roughness. The PDMS precursor mixture (OE-43, Gelest) was prepared using a 1:1 base to curing agent weight ratio. After the mixture was degassed for 15 mins, this PDMS precursor was spun onto the wafer to produce a thin layer of PDMS which made up the core waveguide layer with a slab height of ~4 μm. The spin coated PDMS was cured at 55°C for 4 hours. Thereafter, the second PDMS precursor mixture (Sylgard 184, Dow Corning) was cured at 80°C for 2 hours over the thin layer of PDMS to form the cladding layer. Finally, the cured PDMS structure was released from the master mold.

The PDMS AWG was characterized on a fiber optic alignment stage set. For the characterization of conventional shape AWG, the light source is a solid-state laser (iFLEX2000, PointSource) with a peak wavelength at 641 nm and an emission range of 639 to 644 nm. For S-shape AWG, the light sources were three interchangeable lasers with emission peaks of 473 nm, 532 nm and 641

nm. The laser light source was butt-coupled into the AWG input waveguide through a 9/125 μm single-mode optical fiber. The TE and TM modes measurement was carried out with a polarization maintaining fiber connected to the polarized connector of the laser module. The image of the output end of the waveguide was focused with a 5× objective lens and captured on a CCD camera (Exwave, Sony, Japan). For the transmission spectrum measurement, the light from each output waveguide was measured using a visible light spectrometer (OSM100, Newport) collected through a multi-mode optical fiber. The readings were repeated three times and averaged for the spectrum insertion loss measurement.

4.6 Results and discussions

4.6.1 Conventional AWG

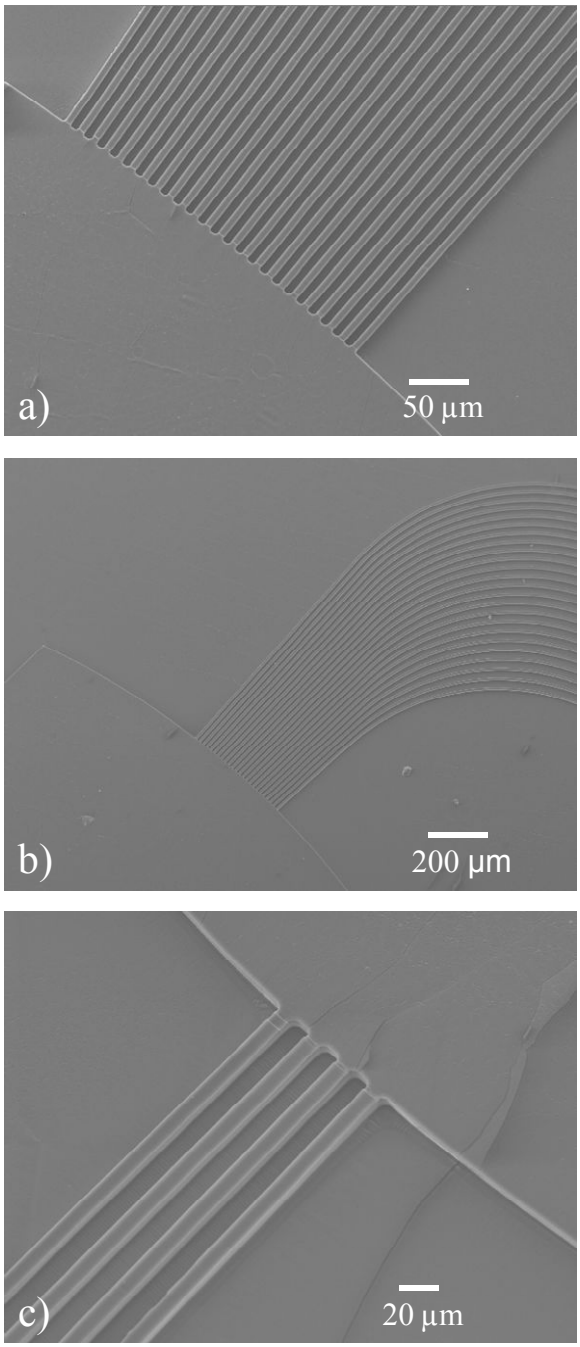

Figure 35: SEM images of the conventional PDMS AWG: a) The arrayed waveguide pitch, b) Top view of the 24 arrayed waveguide c) The output waveguides.

Figure 35 shows the SEM images of the fabricated four-channel PDMS AWG. The images show that the PDMS AWG has well defined sidewall and corners. Cross-sectional microscope studies showed that the PDMS AWG had a slab height of 4.2 μm, a rib height of 9.1 μm and an 88° negative sloping of the sidewall.

Simulations were further performed to evaluate the outcome of the deviations in the slab height, rib height, refractive index contrast and sidewall slope of the waveguides on the AWG performance due to possible variation during the fabrication process (Figure 36). The refractive indices of the PDMS may differ from the values used in simulations because of inherent variations in the process, such as the curing temperature and duration. Thus, an estimated change of 5% and 10% was considered for the refractive index contrast, Δn. Figure 36a shows that such Δn fluctuations have very little impact on the transmission spectrum. As the slab height increases, the insertion loss decreases but the crosstalk deteriorates with the transmission peak shifting to larger wavelengths (Figure 36b). This observation can be explained as follows: a small slab height produces a small beam diameter with stronger confinement, which helps in the diffraction and spectral separation but at the same time provides a smaller transmission area which increases the insertion loss. The slab height of the waveguide depends on the viscosity of the PDMS precursor mixture and the spin speed during spin coating of the PDMS core waveguide layer. A 4 μm slab height was targeted in fabrication by keeping a constant time between the PDMS precursor mixing step to the spin coating step because PDMS viscosity changed once the curing agent was added to the precursor. The thickness and sidewall profile of the SU-8 photoresist determined the

waveguide height and sidewall slope. As shown in Figure 36c, a negative slope within 2 degrees of a vertical sidewall does not shift the peak nor increases the insertion loss significantly. Figure 36d shows that each 1 µm increment in the rib height produces a peak shift of 0.05 nm and increases insertion loss with 0.1 dB. In the fabricated PDMS AWG, a 9.2 µm thick PDMS AWG with an 88° negative sloping has an estimated peak shift less than 0.1 nm and insertion loss of 4.43 dB. These simulation results show that the PDMS core layer slab height is the most critical parameter in the AWG fabrication for ensuring a practical transmission spectrum very close to the simulated one.

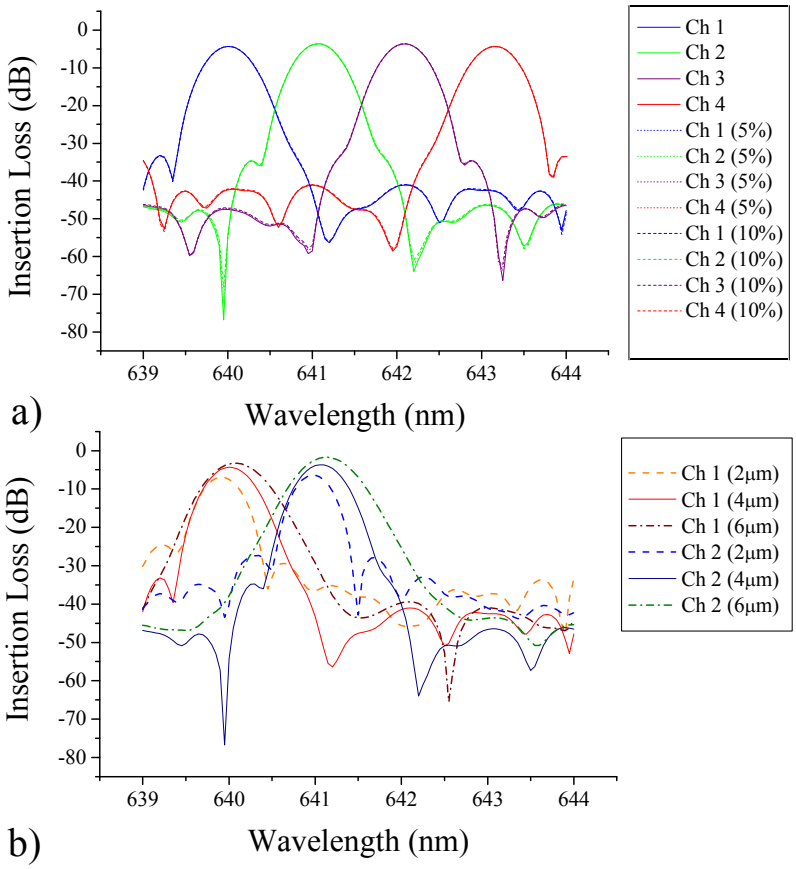

Figure 36: Simulation results indicating the effect of deviations in key fabrication parameters on the performance of a conventional AWG: a) The effect of a 5% and 10% change in refractive index contrast, b) The effect of a 2 µm, 4 µm and 6 µm slab height of the rib waveguide. (cont'd next page)

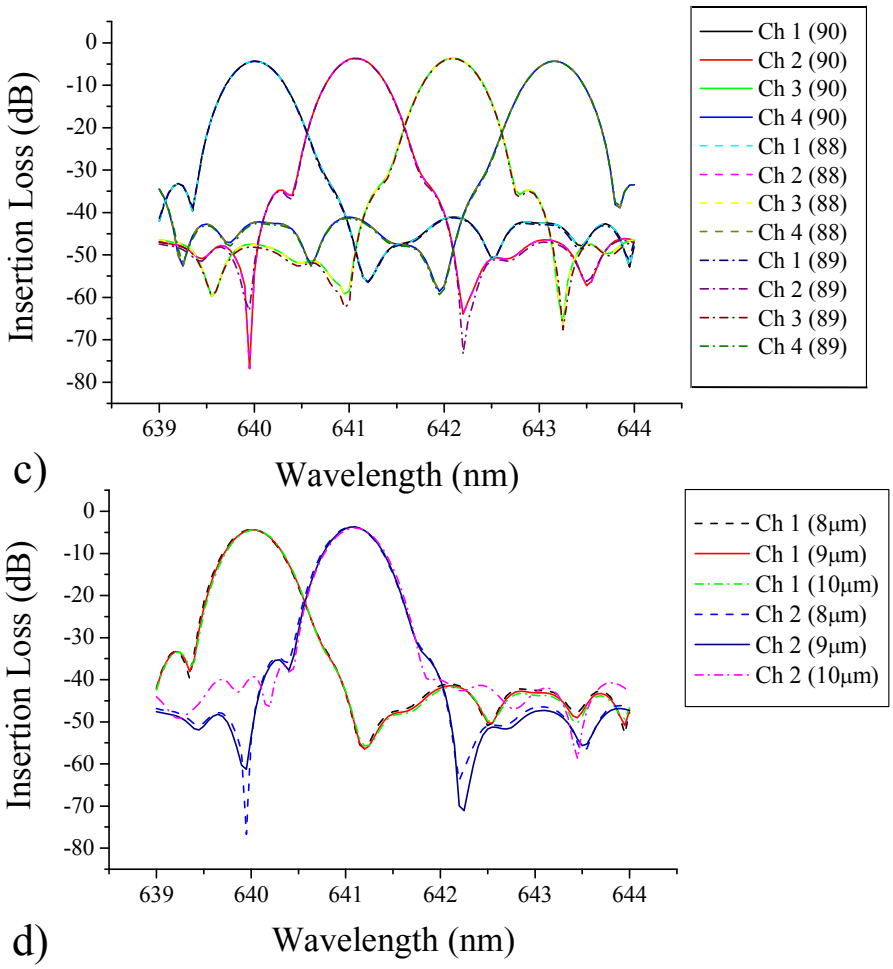

Figure 37: Simulation results indicating the effect of deviations in key fabrication parameters on the performance of a conventional AWG (continued): c) The effect of the waveguide sidewall slope with values of 88° 89° and 90°, and d) The effect of the rib waveguide height (or SU-8 photoresist height), with values of 8, 9 and 10 μm. For (b) and (d), only channels 1 and 2 are shown for clarity.

The near field pattern of the four output waveguides separated by a port pitch of 250 μm is shown in Figure 38. The plotted profile of the mode field is compared with the simulation results for the 4 peaks transmission at 640, 641, 642 and 643 nm. The mode profile shows excellent transmission of the beam intensity through the AWG.

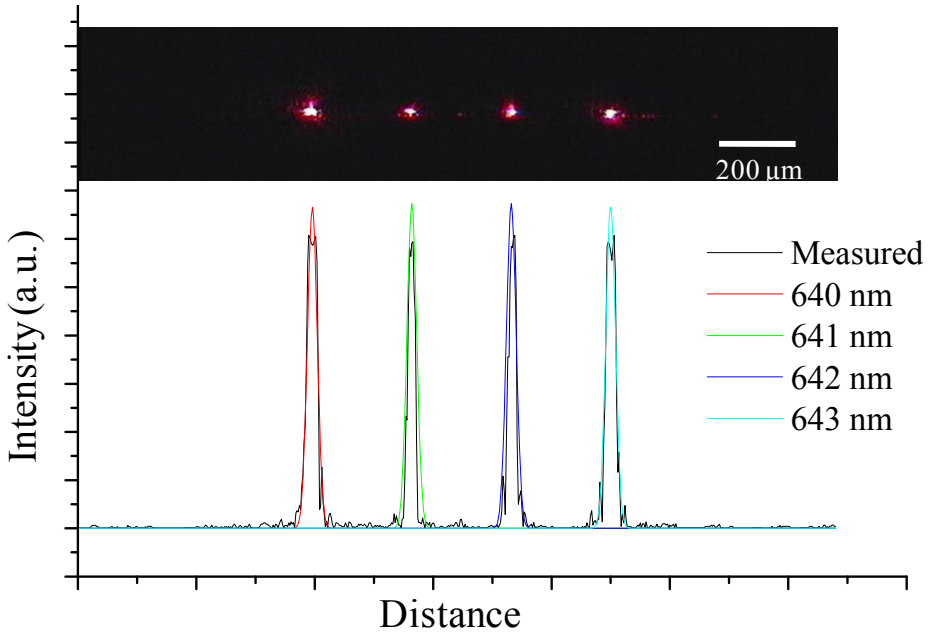

Figure 38: Output modal images of the four-channel PDMS AWG. Comparison of the measured output mode field profile with the simulated results of the output mode for the wavelength of 640, 641, 642 and 643 nm.

Each of the four captured output mode profiles was fitted with a Gaussian variation that was characterized by a FWHM of 4.92 μm as compared with the value of 4.86 μm indicated by the simulations. The simulation results were obtained from the 2D-BPM simulations of the E-field at the output waveguides according to the parameters in Table 3.

The polarization dependence of the pass wavelength difference of an AWG is largely determined by the birefringence of the waveguide. The polarization-dependent pass wavelength difference is given by [108]

$$\delta\lambda = \frac{n_c(TE) - n_c(TM)}{m}\Delta L \tag{79}$$

The birefringence of a rib waveguide structure is mainly caused by stress anisotropy along x and y direction and by the asymmetry in the geometrical parameters of the rib waveguide, i.e. the width to height ratio and

slab height [111]. The calculated polarization-dependent pass wavelength due to geometrical parameters of the rib waveguide is in the order of 0.003 nm, as shown in Figure 39a. The PDMS rib waveguide is made up of a single polymer material which has negligible stress anisotropy induced by any lattice mismatch. As shown in Figure 39b, the measured pass wavelength difference is 0.01 nm between the TE and TM polarization. However, the measured crosstalk has deteriorated as compared with the simulated result (Figure 30) and is mainly attributed to the phase error in the arrayed waveguides region [112]. The phase error is caused by the effective index fluctuation which resulted from the non-uniformities of the width and height of the rib waveguide and the inhomogeneity of the PDMS refractive index. Extra caution was taken in the spin coating and pre-exposure baking steps of the patterning of SU-8 photoresist. The thickness uniformity was measured to be in the range of ± 0.1 μm. Hard contact was employed in the photolithography step to reduce lateral variations due to diffraction effect. The inhomogeneity of the PDMS refractive index is related to the mixing and curing process. This inhomogeneity effect can be alleviated by degassing the PDMS precursor for at least 1 hour before curing and slow ramping-up of the temperature in the curing step.

Figure 40 shows the measured transmission spectrum of the four-channel PDMS AWG. The measured total insertion loss was 11.4 dB for the transmission peak at 641 nm and the insertion loss uniformity of the four channels is 0.5 dB. The non-uniformity insertion loss of the PDMS AWG is being termed as a Gaussian shape spectral response where the center output port has a higher transmission than the peripheral output port. The reason for this

spectral response is the Gaussian input electric field being sampled by the arrayed waveguide and reproduced at the output plane [108].

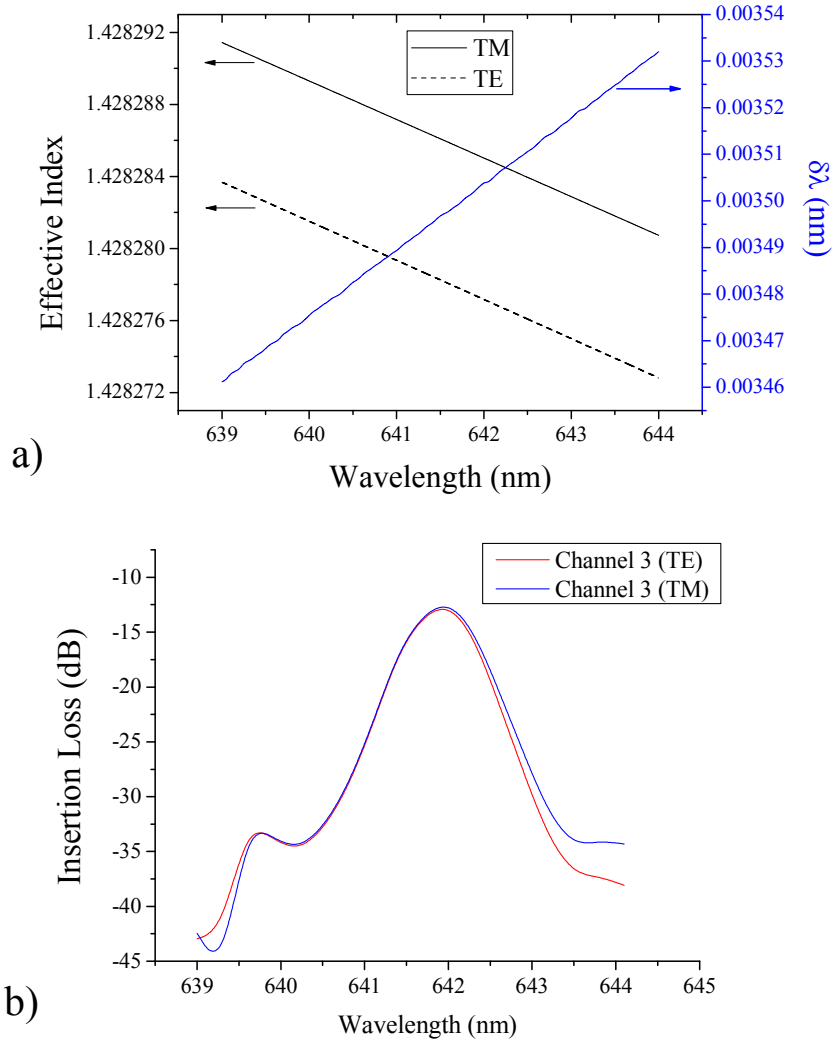

Figure 39: The TE and TM mode studies for the PDMS AWG; a) the calculated pass wavelength difference caused by the effective index difference of the TE and TM mode and b) measurement of the insertion loss of both TE and TM modes, only channel 3 is shown for clarity.

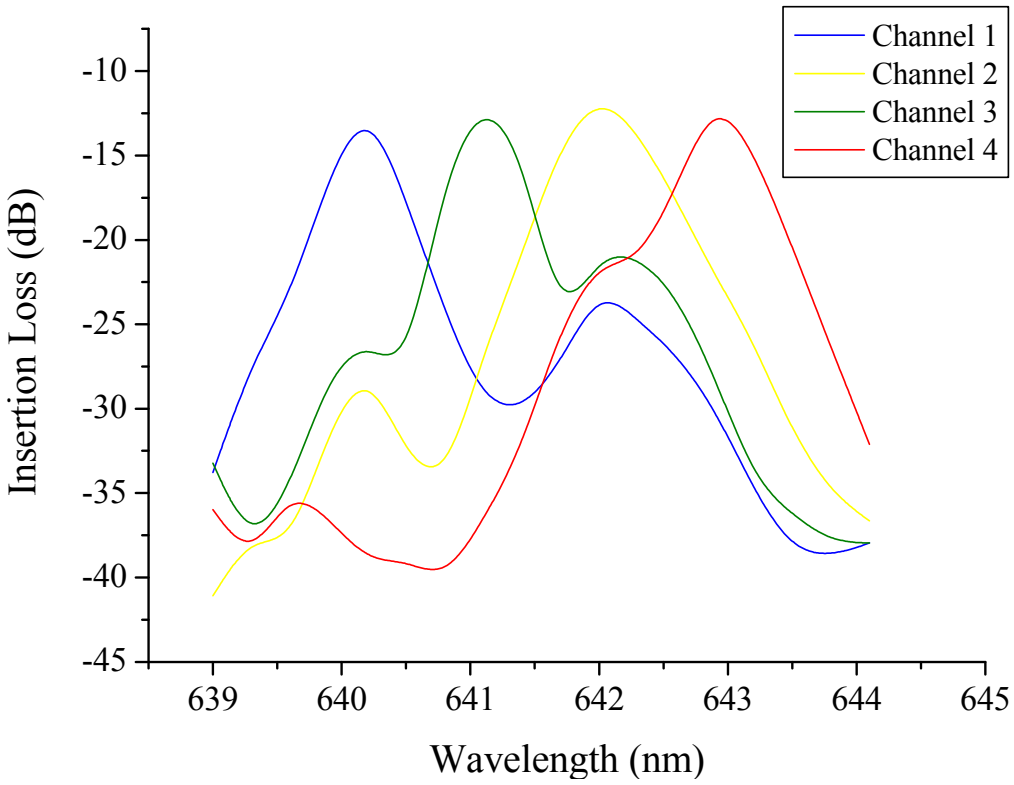

Figure 40: Measured insertion loss of the four-channel PDMS AWG.

As shown in Figure 36b, the Gaussian spectral non-uniformity increases as the slab height of the single-mode PDMS waveguide increases from 2 to 6 μm. As the slab height increases, the Gaussian beam mode diameter of the input waveguide increases. At a fixed focal length, the width of the Gaussian far field pattern projected by the input waveguide at the arrayed waveguide is inversely proportional to the beam mode diameter of the input waveguide. For an equal number of arrayed waveguides of identical size and pitch, a broader Gaussian field produces a more uniform insertion loss because it is being sampled only at the center flattened field. In contrast, a narrower Gaussian field will be sampled across the entire field pattern. Nevertheless, the insertion loss for an input waveguide with a smaller slab height increases due to the partial sampling of the Gaussian field as well as a smaller transmission area. In the fabrication of our PDMS AWG, the slab height of the waveguide varies within 4 ± 1 μm.

Thus, a variation of the insertion loss uniformity is expected within 0.4 to 0.6 dB (Figure 36). The PDMS AWG insertion loss non-uniformity can be improved by modifying the input waveguide with a flat response shape [113] or by making a sinc-like electric field envelope in the array waveguides [114].

A comparison between the measured (Figure 40) and simulated (Figure 30: Simulation results of the 4 channel PDMS AWG as per design shown in Table 3.) results shows that the insertion loss differs from the simulated value by ~7 dB. The measured adjacent crosstalk of the AWG is >15.1 dB is also lower than the simulated result of 34 dB. The much higher insertion losses observed practically are attributed to the fiber to waveguide coupling loss, measured to be 4.1 dB. The other losses can be attributed to the waveguide bending and propagation loss of the waveguides as well as the variation of the slab height in the fabrication process. The measured transmission spectrum shows channel separation of 1 nm and FSR that spans more than 4 nm. The adjacent crosstalk was degraded by the formation of higher order leaky modes in the arrayed waveguide. Each of the higher order modes has its own propagation constant which produce ghost peaks and changes in the passband shape and center wavelength.

The face end PDMS waveguide has striation marks due to direct molding or cutting. The waveguide does not allow face end polishing like those utilized in silicon-based waveguide to enhance coupling efficiency. Nonetheless, the fiber-to-waveguide coupling can be improved by incorporating a tapered structure or grating coupler.

The normal operating temperature for PDMS is from –45°C to 200°C and thermal degradation only happens when temperature exceeds 300°C. However,

PDMS is a rubbery material which is sensitive to mechanical and temperature fluctuations. Based on the values of $dn/dT = -3.4 \times 10^{-4}$/°C and coefficient of thermal expansion $\alpha = 3.4 \times 10^{-4}$/°C, the calculated temperature sensitivity of the pass wavelength in the PDMS AWG for visible light is about $\Delta\lambda/\Delta T = 4.8 \times 10^{-2}$ nm/°C. Hence, the operation of the PDMS AWG for visible light spectroscopy applications should be implemented in a well-controlled environment to prevent thermal shift of the spectrum.

4.6.2 S-shaped AWG

The S-shaped AWG was demonstrated as a coarse wavelength channel separation device where wavelength separation is in the range of tens of nanometers. Therefore, the polarization independent pass wavelength difference is not as critical as in the conventional nanometer resolution AWG. The pass wavelength difference polarization dependence in the range of < 1 nm is small as compared with the wavelength separation of the output channels. The near field pattern of the three output waveguides is shown in Figure 41. Three separate lasers were alternately used as light source; red (641 nm), green (532 nm) and blue (473 nm). The laser light source was butt-coupled into the AWG input waveguide through a 9/125 μm single-mode fiber optic. The images of shown in Figure 41 (b), (c) and (d) are captured by interchanging the three different laser light sources.

The plotted profile of the mode field is shown in Figure 42. The mode profile shows excellent transmission of the beam intensity through the AWG. Each of the three captured output mode profiles clearly and demonstrates RGB separation.

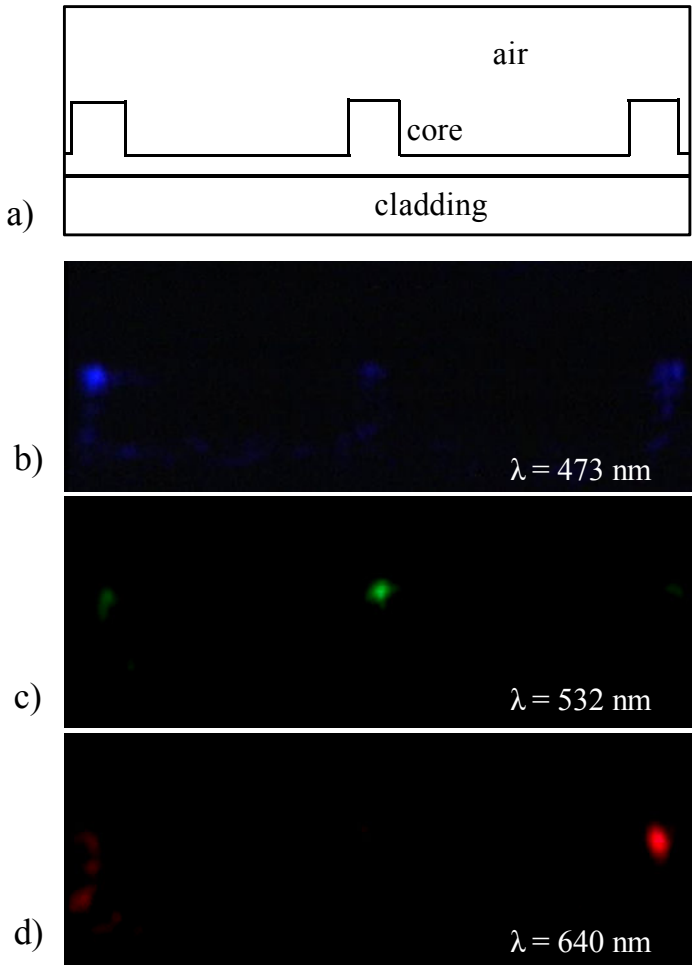

Figure 41: Face end images at the outputs of the S-shaped AWG: a) Schematic cross-section through the output of the S-shaped AWG, and b) Blue c) Green and d) Red.

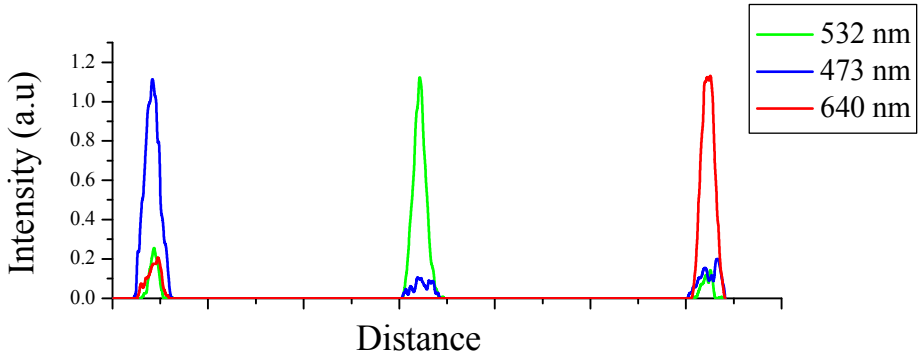

Figure 42: Output mode profiles of the S-shaped AWG.

In this chapter, the design, fabrication and experiment of PDMS-based AWG are presented. Two types of PDMS AWG were designed to meet the requirements of high resolution and large *FSR* for a microspectrometer. The first conventional PDMS AWG has been designed with a resolution as high as 1 nm. The second non-conventional PDMS AWG with an S-shape arrayed waveguides has been realized with large *FSR* of 275 nm.

The fabrication-related error studies on the conventional PDMS AWG had shown high tolerance to refractive index contrast Δn change up to 10% and sidewall slope angle of 2˚. Nonetheless, the precision of the slab and rib heights were critical in ensuring a practical transmission spectrum very close to the simulated one. Hence, the fabrication methods for both types of PDMS, conventional and non-conventional AWG were carried out with cautionary steps to produce a uniformity of ± 0.1 μm for the rib and slab heights. The measured transmission loss of the conventional PDMS AWG has shown an insertion loss of 11.4 dB at 641 nm transmission peak and adjacent crosstalk of > 15 dB with channel loss uniformity well within 0.6 dB. The polarization dependency of the transmission characteristic was measured to be around 0.01 nm which is caused by effective index fluctuation which resulted from the non-uniformities of the width and height of the rib waveguide and the inhomogeneity of the PDMS refractive index.

Both types of PDMS AWGs have demonstrated for high resolution and large *FSR* which serves as a potential candidate for excellent microspectrometer if used in a cascaded manner.

CHAPTER 5

POLY(DIMETHYLSILOXANE) WAVEGUIDES INTEGRATED WITH MICROFLUIDICS FOR LAB-ON-A-CHIP ABSORPTION SPECTROSCOPY

The objective of this chapter is to investigate optical detection performance of PDMS waveguides integrated together with microfluidics as a component of a LOC microspectrometer.

The integration schemes for PDMS microfluidics with straight and curved multi-mode waveguides in a direct free space manner are presented. The characterization of the optical detection performance of microfluidics integrated with waveguides in PDMS is presented to test the sensitivity, limit of detection and signal-to-noise ratio. Results of real-time measurement of fluorescein are presented to assess of the system's performance.

As the size of the optical components shrinks, the optical detection performance of related analytical methods, e.g. absorption spectroscopy is adversely affected. As a counter-measure, an enhancement method based on total internal reflection is proposed to improve the sensitivity of the measurement. Leveraging on the PDMS material properties and the low cost and simple fabrication technique, a multi-reflection microfluidic chip was fabricated and the absorbance measurement was characterized for increased sensitivity measurement.

The direct integration of PDMS single-mode waveguides with microfluidics in the simplest configuration results in a large diffraction loss as the light traverses across the channel. Evanescent field absorption spectroscopy

with a PDMS single-mode waveguide is presented to counteract the large diffraction loss.

5.1 Co-integration of PDMS waveguides with microfluidics

The miniaturization of the microspectrometer for LOC demands a micro total analysis system (μTAS) which integrates both microfluidics and optical detection capabilities into a single platform [115, 116]. Such a LOC platform can benefit from various optical microcomponents capable of efficiently focusing and guiding light to a desired point in order to achieve a highly sensitive and robust detection at a low cost [117]. In this regard, numerous efforts have been made to develop new optical prisms, lenses and waveguides for LOC integration [118].

Conventional optical fibers are attractive due to their intrinsic ability to direct light and their efficient coupling with commercial light sources and detectors. Nevertheless, their alignment with microfluidic channels at detection sites can be problematic and extremely time-consuming as any imperfect coupling may result in high optical losses which can degrade the overall efficiency of the optical detection. Monolithic waveguides have been pursued for microfluidic absorption detection to limit the misalignment problem as well as to produce a high level of integration [119].

In this chapter, the monolithic integration of PDMS waveguide and microfluidic all in a single PDMS chip is pursued. The integration of either single-mode or multi-mode PDMS waveguides with microfluidics was investigated. In addition, various schemes of enhancing the detection capabilities was also explored.

5.2 Theory

The absorption measurement spectroscopy is governed by the Beer-Lambert's Law

$$A = \log_{10}(I_0/I) = -\log_{10} T = \varepsilon \times L \times C \tag{80}$$

where I_0 is the incident light intensity, I is the measured light intensity after passing through the sample, L is the optical path length through the sample, C is the analyte concentration and ε is the molar absorptivity (extinction coefficient) of the analyte.

5.2.1 Multi-mode waveguide with microfluidic

Several groups have aimed at a monolithic integration of multi-mode waveguides and microfluidics all in a single PDMS chip [120, 121]. However, these devices have been implemented with either intrinsically "lossy" hollow waveguides where PDMS acts only as cladding [120], or liquid waveguides where PDMS does not take any part in the waveguide material [121]. The liquid waveguides have been defined in microchannels by liquid-liquid interfaces which are mechanically unstable and require constant circulation (and hence consumption) of fluids through the chip. Here, multi-mode waveguides were integrated with a microfluidic channel of varying width perpendicular onto the waveguides, as shown in Figure 43. Hence, the optical path length through the sample L stated in equation (80) is directly determined by the microfluidic channel width.

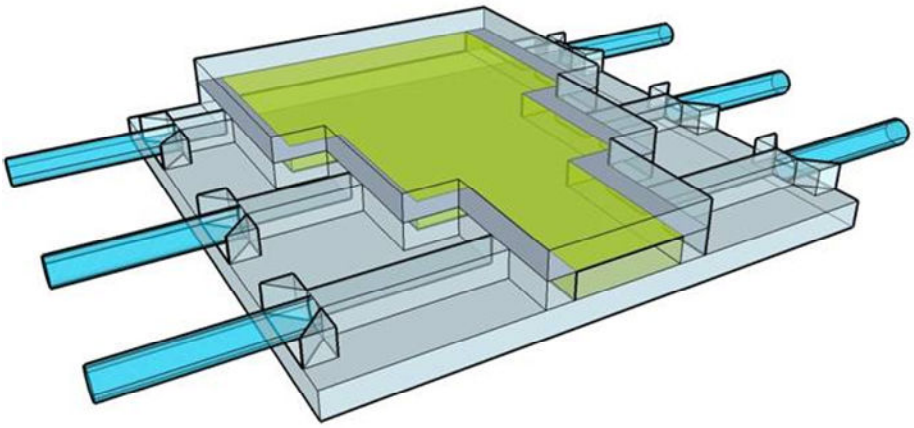

Figure 43: Schematic of the straight waveguides integrated with a microfluidic channel.

In such a perpendicular arrangement of the waveguides with respect to the microfluidic channel, detection issues will arise when the microfluidic channel's width reduces as the device shrinks. The reduced sample volume means a reduction of sensing volume, decreasing the number of analytes available for detection and making it more difficult to detect them. Therefore, the two main factors that affect the optical sensing are sensitivity and scalability to smaller dimensions [122, 123].

Based on Beer-Lambert's law given by equation (80), the absorbance measurement for low concentration of analytes in a microfluidic channel is limited by the short optical path-length L inherently associated with a small microchannel width. To circumvent this drawback, several groups have attempted to improve the sensitivity of the optical detection. Petersen et al. has demonstrated a U-cell configuration microfluidic channel to lengthen the optical path-length to 750 μm [124]. However, the stray light becomes the dominant issues, i.e. light that does not pass through the microchannel is detected.

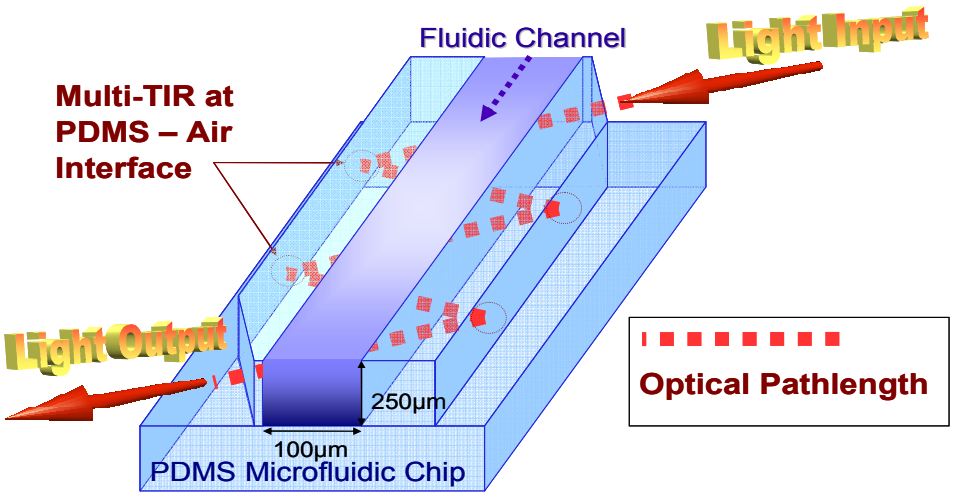

Figure 44: Schematic of Multi-TIR concept.

In another approach, the interactions of fluids with light can be increased by employing multireflections such as the demonstration by Verpoorte et al. [125]. The sensitivity of the detection has increased tremendously by multireflection, utilizing the mirror light surface of a silicon crystalline plane in the channel wall fabricated through anisotropic wet etching. The silicon crystalline plane reflectivity can be enhanced by coating the channel walls with metal, as reported by Salimi-Moosavi et al. for capillary electrophoresis application [126]. Multireflection by monocrystalline silicon has limited applicability since silicon's reflectivity is rapidly affected by absorption which increases significantly for shorter wavelengths in the UV-Visible light range, whereas coating with metal brings in additional processing steps and increased cost. An alternative approach is proposed and presented with PDMS material; the multireflection of light by employing the total internal reflection phenomenon. The Multi Total Internal Reflection (MTIR) was implemented in PDMS and combined with microfluidics by positioning the light input beam of the waveguide at an incident angle greater than the critical angle of the PDMS-air interface at the channel's sidewalls as shown Figure 44.

5.2.2 Single-mode waveguide with microfluidic

The integration of a large cross section microfluidic channel (in the range of tenth of micrometers) with small cross section (8 μm) waveguides requires accurate alignment and does not permit a perpendicular arrangement such as the multi-mode waveguide. A large cross section microfluidic channel is required for low pumping pressures because the pressure difference of a fluid flow along a microchannel is inversely proportional to the cross sectional area of the microchannel. As the small beam diameter of the light propagates across the microfluidic channel, the light will diffract as in free space and only a small portion of light is collected by the small size single-mode waveguide at the opposite side of the microfluidic channel. Thus, high high diffraction loss is associated with such arrangement.

For the efficient detection of very small volumes using small waveguides, evanescence field sensing was proposed by Pandraud et al. where the waveguide runs parallel to the microfluidic channel [127]. The evanescent field exists at the waveguide core-cladding interface and penetrates into the cladding layer up to a depth of several hundreds of nanometers as the light propagates along the waveguide core.

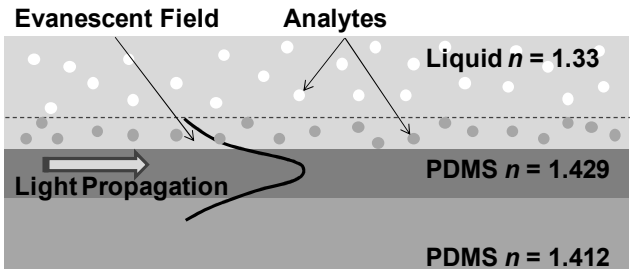

Figure 45: Schematic diagram of the evanescent field absorption spectroscopy concept.

The analyte that comes into this field evanescened from the guided mode propagating along the waveguide interacts with it and alters its intensity. This interaction of the evanescent field with the analytes adjacent to it at the core-cladding interface provides the sensing mechanism for absorption spectroscopy. The concept of such an evanescent sensor is shown in Figure 45. Evanescent wave absorbance can be measured and calculated by the modified Lambert-Beer formula

$$A = \log(I_{ref} / I_{sample}) = \sigma \times \varepsilon \times l \times c \quad (81)$$

where I_{ref} is the light intensity measured by the detector when a non-absorbing reference medium is used, I_{sample} is the light intensity measured by the detector when an absorbing analyte is used, σ is the fraction of the normalized mode power propagating in the evanescent field region of the waveguide, ε is the molar absorption coefficient, l is the optical path-length and c is the concentration of the analyte.

5.3 Experimental

5.3.1 Integrated multi-mode waveguide with microfluidic

The multi-mode waveguide was fabricated as detailed in Chapter 3. Here, a brief summary of the fabrication steps of integrated waveguide with microfluidic is presented. The master template for the soft lithography was prepared by patterning a 250 µm thick SU-8 photoresist spun on 8-inch silicon wafers. The PDMS precursor mixture (Sylgard 184, Dow Corning) was prepared at a weight ratio of base to curing agent 10:1 and split into two portions. One portion was further mixed with 10 % w/w of silicone oil (200® Fluid, Dow Corning, Inc.) to increase its refractive index. The first precursor

mixture with the additive of silicone oil was spun on the SU-8 patterns at a nominal thickness of 250 µm. The spun on precursor mixture filled up the SU-8 trenches and was allowed to settle down to a uniform layer, thereafter being cured at 80°C for 2 hours. This PDMS layer defined the waveguide core and microchannel sidewalls. The second precursor mixture without the additive of silicone oil was subsequently poured and cured over the wafers. This second PDMS layer, once cured the same way as the previous one, fused together with the first one and formed the waveguide device substrate. The resulting monolithic PDMS was then peeled off from the wafers and cut into individual chips. A third layer of PDMS was punched with inlet/outlet holes and, using oxygen-plasma surface activation, permanently bonded to the PDMS device substrate to cap the microfluidic channels and to form the final structure.

All waveguides had a square cross-section with a size of 250 µm by 250 µm to provide a larger throughput for light collection and to match a commercially available 250 µm size fiber optic. Two sets of design are presented; straight waveguide (Figure 46a) and 90°-curved waveguide (Figure 46b) integrated with microfluidic channels of various widths.

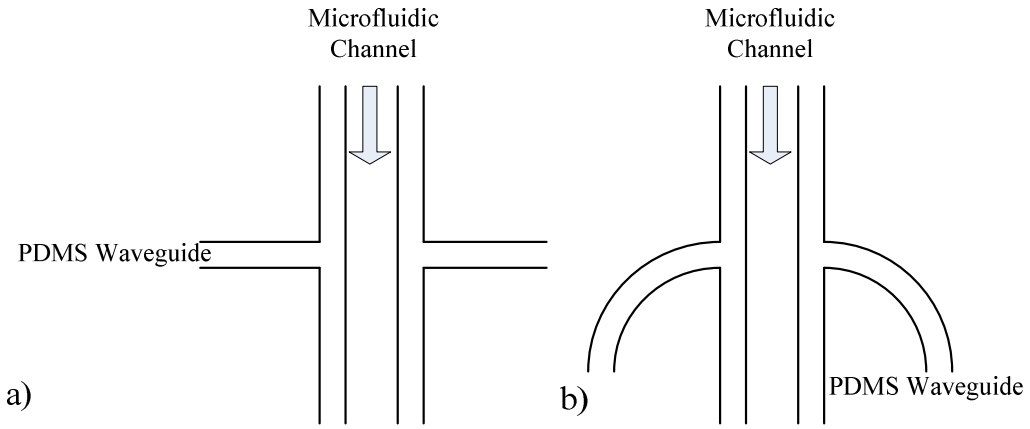

Figure 46: Schematic of the integration of PDMS multi-mode waveguide with microfluidic.

The first design set of straight waveguides coupled with microfluidic channels 250 µm, 500 µm and 1000 µm wide, and the second design comprised a set of 90°-curved waveguides 4 mm, 6 mm and 8 mm in radius of curvature coupled with microfluidic channels 500 µm wide. The straight waveguide design has the excitation and collection optical fibers in a straight path arrangement whereas the 90°-curved waveguide design has the optical fibers perpendicular to each other.

The PDMS devices were tested on a probe station (Cascade Microtech, Inc.) whereby optical fibers 250 µm in diameter were properly aligned and butt-coupled with the PDMS waveguides by means of custom-made holders mounted on the micromanipulators (Figure 47a). Silicone oil type 200® Fluid (Dow Corning Inc.) was applied at the fiber-waveguide interface to match their refractive indices and thereby reduce coupling losses. The optical fibres were then connected to the source and detector via an Ocean Optics coupler. The light source was a turquoise light emitting diode (LED) type ETG-5CE490-15 (ETG, Inc.) with 491 nm peak emission wavelength powered by 150 mA current pulses with 1 kHz frequency and 10% duty cycle. The photocurrent from the SFH 213 silicon photodiode (OSRAM, GmbH) was demodulated using the pulses powering the LED as a reference. The output signal from a demodulator was filtered by a low-pass filter of 4th order with 2 Hz cut-off frequency (Figure 47b) [128]. This modulation/demodulation technique improved the signal-to-noise ratio by several orders of magnitude and also suppressed the influence of ambient light and other sources of noise. The resulting signal was recorded by DPO 7054 oscilloscope (Tektronics, Inc.) and each measurement was repeated three times.

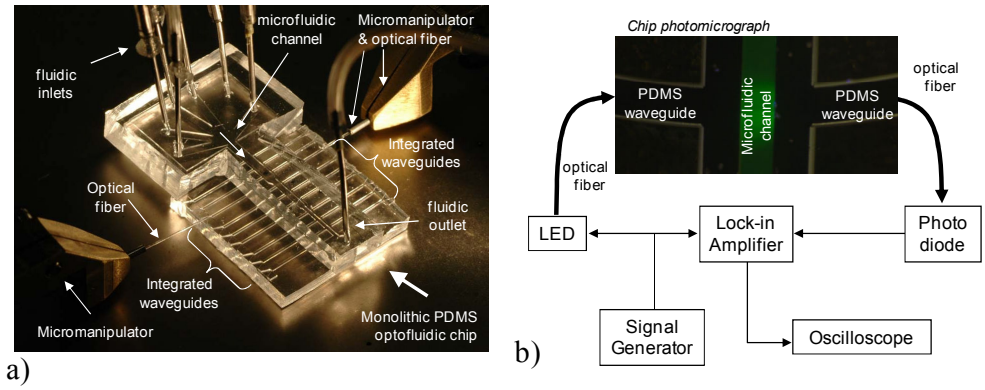

Figure 47: Experimental setup. (a) Photograph of a fabricated optofluidic device including an array of integrated straight waveguides coupled with a microchannel; (b) Block diagram of a complete measurement setup.

Test solutions were prepared by dissolving fluorescein salt (Sigma-Aldrich, Inc.) in de-ionized (DI) water at concentrations ranging from 0.5 μM to 50 mM. DI water without fluorescein was used as a reference. Test and reference solutions were delivered into microchannels by syringe pumps (KD Scientific, Inc.).

For the MTIR demonstration, a 635 nm pigtailed laser diode (Edmund Optics, Inc) was used as the light input and the light output was detected by a photodiode (Perkin Elmer, VTB8440B). Reflectivity measurements were carried out for incident angles of 40°, 45°, 48°, 50°, 53° and 55° using silicone oil as an index matching fluid in the channel for characterisation. Brilliant blue (Sigma) of concentration from 0.1 μM to 500 μM was used in absorbance measurements for one, two and four TIRs in the channel.

5.3.2 Single-mode waveguide integrated with microfluidics

The single-mode PDMS rib waveguides made use of air (n = 1) as the top and side cladding. In utilizing the rib waveguide as an evanescent wave

sensor, the liquid analyte with $n \approx 1.33$ flows along and adjacent to the waveguide core and makes up the top and side cladding.

The fabrication of single-mode waveguides integrated with microfluidics is shown in Figure 48. The PDMS waveguides were fabricated using two types of PDMS: Gelest OE43 ($n = 1.429$) for the core layer and Dow Corning's Sylgard 184 ($n = 1.412$) for the cladding layer. For the core layer, the PDMS precursor mixture (OE-43, Gelest) was prepared at a 1:1 weight ratio of base to curing agent. This PDMS precursor has low viscosity which allows spin coating onto the wafer to produce thin layers of PDMS. The spin coated PDMS was cured at 55°C for 4 hours. Thereafter, the PDMS precursor mixture (Sylgard 184, Dow Corning) was prepared at a weight ratio of base to curing agent of 10:1 and cured over the thin layer of PDMS to form the cladding layer. This second PDMS precursor mixture was also used for the microfluidic layer mold. The resulting PDMS layers containing the single-mode waveguides and the microfluidics were peeled off from their respective molds and cut into individual chips. The PDMS microfluidic layer was punched with inlet/outlet holes. Both the waveguide layer and microfluidic layer chip were washed with isopropanol and de-ionized water and placed in a 150°C oven for dehydration bake for 20 mins. After oxygen-plasma surface activation, the two layers were properly aligned and permanently bonded to form the final structure.

The single-mode waveguide for evanescent field sensing was characterized on a fiber optic alignment stage set. A visible light source (Ando, AQ4303C) was butt-coupled to the waveguide through a 9/125 μm single-mode fiber optic and the signal from the output waveguide was collected by a multi-mode fiber optic connected to an optical spectrometer (Newport, OSM100-

UV/Vis). For all evanescent wave absorbance measurements, ultra pure water was pumped into the microfluidic channel and taken as the reference signal. Subsequently, various analytes were pumped into the microchannel for reading.

Biomolecules of interest, such as oligonucleotides, protein or DNA, can be immobilized on the PDMS waveguide surface and interact with the light in this evanescent field region. The biomolecule has a typical size of a few hundreds of nanometers and falls well within the evanescent field region. If the biomolecules are labelled with a fluorescent tag, they can be excited by the evanescent field and their emission can also be collected back into the waveguide. The excitation signal can be used for detection of the biomolecule of interest using evanescent field absorption spectroscopy.

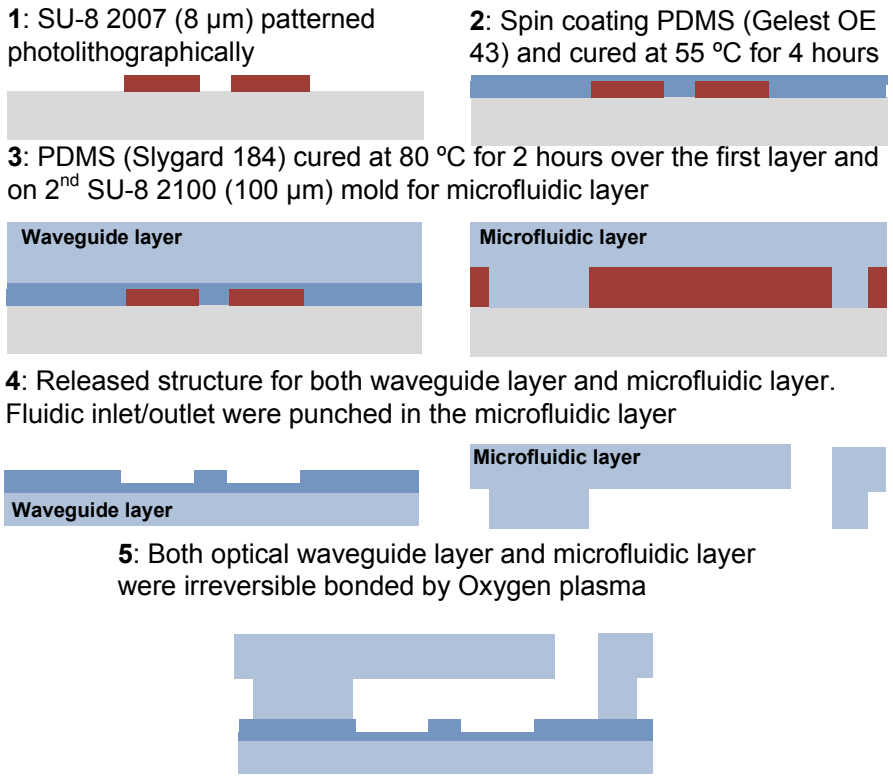

Figure 48: The fabrication steps involved for the integration of single-mode waveguides together with microfluidics.

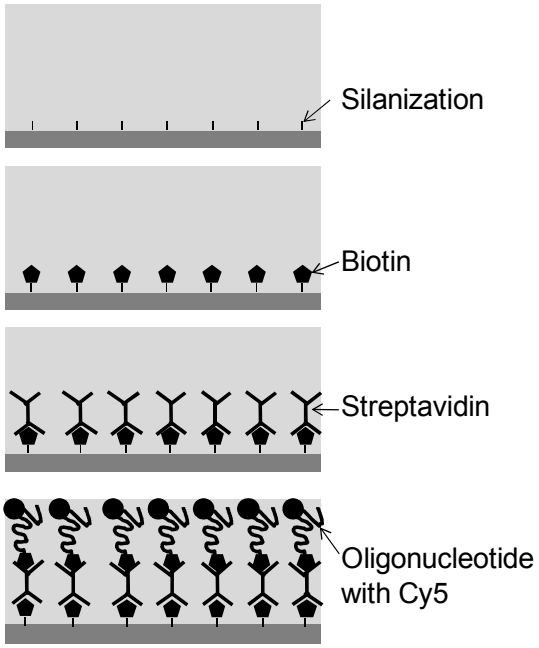

Figure 49: Immobilization steps of the oligonucleotide on the PDMS waveguide.

The oligonucleotide was immobilized on the PDMS waveguide surface to demonstrate the evanescent spectroscopy. A schematic representation of the key surface functionalization is shown in Figure 49. The inert surface of PDMS was activated by oxygen plasma followed by pumping a prepared solution of pure water, denatured ethanol and 3-aminopropyltriethoxysilane (APTES) mixed in a ratio of 1:2:197 at 0.4 ml/hr for 2 hours. The device was washed by pumping ethanol and dried with air. Next, 10 µg/ml of sulfo-NHS-biotin in 1× phosphate buffer saline (1×PBS) was pumped into the microchannel and incubated at room temperature for 1 hour. The unreacted biotin was washed by pumping 1×PBS through the channel and dried by air. After that, 1 µg/ml of streptavidin in 1×PBS was pumped into the chip and incubated for 1 hour at room temperature. After washing with 1×PBS and drying, the oligonucleotide immobilization was accomplished by pumping the Cy5 labelled biotinylated

oligonucleotide into the chip and incubated for 1 hour at room temperature. The whole surface functionalization was completed by thoroughly washing with 1×PBS pumped through the microchannel.

5.4 Results and discussions

5.4.1 Multi-mode waveguide direct absorbance detection

The utility of absorption measurement by PDMS waveguides was demonstrated by monolithically integrating the straight waveguides with a microfluidic channel. In addition of low loss guiding of light in straight direction, compact curved waveguides with microfluidics are also necessary to achieve high integration densities (Figure 50).

Moreover, curved waveguides have another advantage, namely circumventing the stray light issues. Stray light is part of the incident light from the optical fiber which does not couple into the excitation waveguide and propagates unguided in the device. If stray light reaches the detector without passing through the detection microchannel, the noise level will increase and thus affect the sensitivity level [124]. Curved waveguides, due to their perpendicular arrangement of the excitation and collection optical fibers, reduce the amount of unguided light that does not pass through the waveguides and microchannel. Hence, a second set of experiments were repeated to explore the sensitivity performance of curved waveguides with microfluidics.

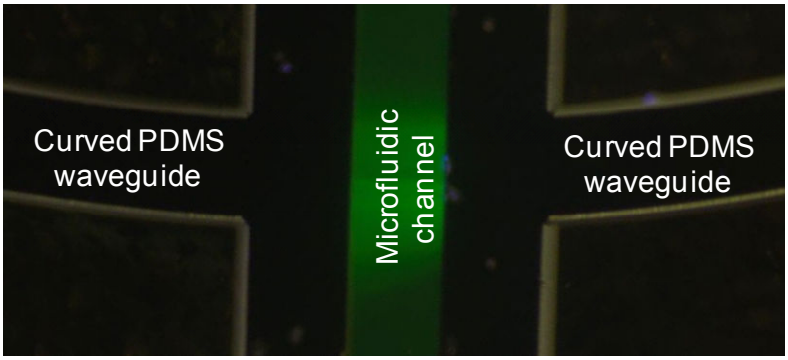

Figure 50: Microscope image of curved waveguide integrated with microfluidic channel.

Real-time absorbance readings from the device, when it was alternately pumped with a series of increasingly concentrated test solutions, is presented in Figure 51. Each test solution was subsequently removed by a DI water wash. After washing, the absorbance signal returned back to its original baseline level with the exception of a slight drift at 0.01V. This indicated that fluorescein did not noticeably stain the microchannel wall. The signal-to-noise ratio is defined as the ratio of the amplitude of signal detected to the background noise at the baseline signal reading and it remained at 58 dB. The response to a concentration step of 100 μM took about 2 min to stabilize when the test solution was applied at a rate of 100 μl/min (1.33 cm/s). As detailed in Figure 51b, the signal decayed linearly at a rate of 3.7 mV/s and then exponentially with a time constant of 10 s. The syringe pump was connected to the PDMS chip through long fluid delivery tube. The time required to drive the test solution from the pump to the detection site took about 35 s. Based on the solution of the Fick's second law of diffusion, the concentration step profile of this fluorescein underwent diffusion in this period of time (~35s) and resulted in a complementary error function (erfc) profile.

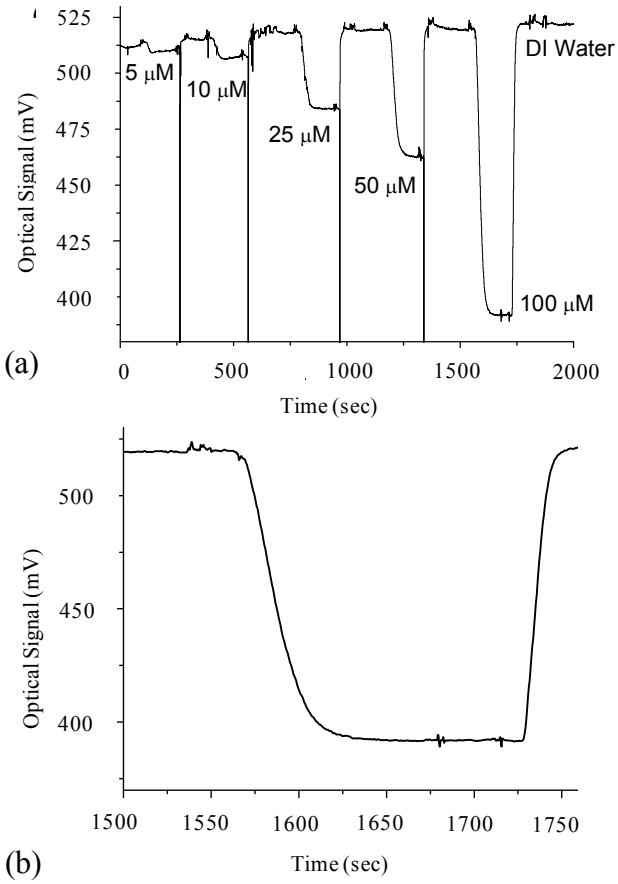

Figure 51: (a) Real time absorption measurement on the integrated device as the microchannel is sequentially pumped with increased fluorescein concentrations. The sharp drops between the solutions are air-bubble artefacts and have no influence on the measurement. (b) Details of the signal segment that corresponds to the 100 μM sample.

Furthermore, the pressure driven (Poiseulle) flow increased the effective diffusion length of fluorescein in the flow direction which severely stretched the (erfc) profile. The resultant effect was a profile with low gradient linear profile in the center with slow decaying exponential profiles at the two ends. The initial exponential decay of the profile is less observable due to low concentration level. Subsequently, the linear concentration profile was detected in the linearly decay rate of 3.7 mV/s that lasted 25 s, while the slow exponential decay had a time constant of 10 s. By definition, the signal

stabilized after 5 times the time constant which gave duration of 50 s. Hence, the total time required for the signal to stabilize is about 110 s or about 2 mins.The steady-state absorbance readings taken from the integrated waveguide devices can be correlated to the corresponding concentration levels by the calibration plots given in Figure 52. Regardless of their waveguide geometry, whether they are straight (Figure 52a) or curved (Figure 52b), the calibration plots for the shown concentration ranges follow a nearly linear trend with slope and intercept values as listed in Table 5.

W (μm)	RC (mm)	S ($\times10^{-3}$) ($AU\mu M^{-1}$)	I ($\times10^{-3}$) (AU)	R^2	LOD (μM)
1000	-	1.63 ± 0.08	4.03 ± 9.04	0.990	30.8
500	-	1.14 ± 0.02	-2.65± 2.03	0.999	9.9
250	-	0.47 ± 0.01	-2.44 ± 0.60	0.999	7.0
500	8	2.36 ± 0.07	-29.97 ± 15.05	0.996	39.7
500	6	2.36 ± 0.07	-26.47 ± 14.49	0.996	38.2
500	4	2.49 ± 0.09	-12.24 ± 19.02	0.994	47.5

[a]W – microchannel width; RC – radius of waveguide curvature; S – slope; I – intercept; and LOD – the limit of detection.

Table 5: Regression parameters and the limit of detection (LOD) values calculated for the calibration plots.

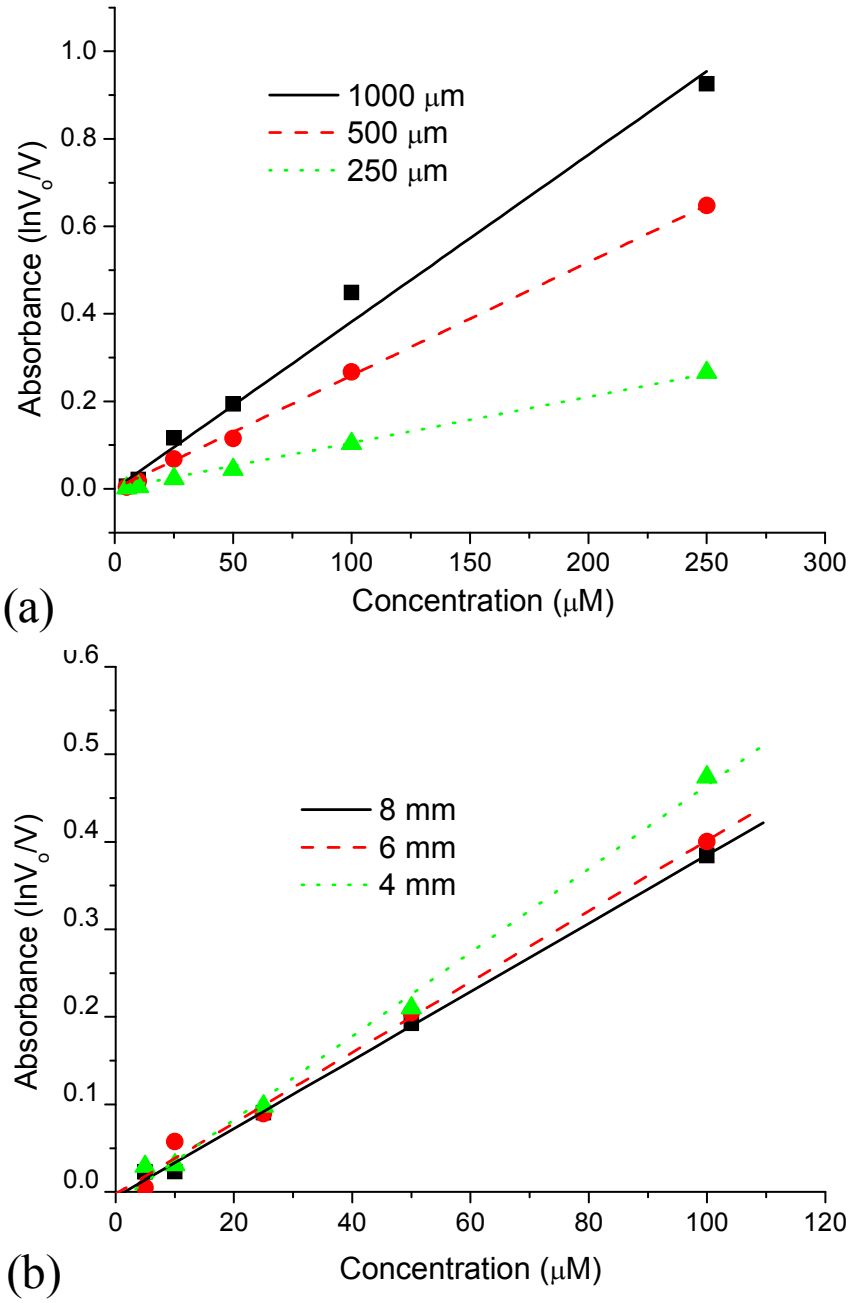

Figure 52: Calibration plots for the absorbance measurement on the integrated devices with: (a) Straight waveguides; the legend inserted in the plot refers to microchannel width, and (b) curved waveguides, the legend inserted in the plot refers to waveguide radius of curvature. For this latter case the microchannel width remained at 500 μm.

A null intercept value can be assumed as most regression lines pass near origin. The slope which sets the sensitivity of the absorbance measurement more or less increases proportionally with the microchannel width for the devices with straight waveguides. This is expected according to Beer-Lambert's law as the width directly determines the optical path length through the sample. For all the devices with curved waveguides, the microchannel width is kept at 500 μm and thus their absorbance sensitivities do not appreciably change.

At low concentrations, the sensitivity decreases by a factor of (1 – *stray*) where *stray* can be defined as the fraction of light that reaches the detector without passing through the detection cell [124]. The sensitivity of the straight waveguides and 90°-curved waveguides can be compared if they have the same optical path length and same molar absorption coefficient. For the same microchannel width (500 μm), a two-fold increase in sensitivity of the same studied analyte (fluorescein) can be noticed for the curved-waveguide in comparison with the sensitivity for the straight one. Thus, we can conclude that curved waveguides design has a reduced amount of stray light in absorption measurement as compared with the straight waveguides.

The limit of detection (LOD) is defined as the minimal amount of analyte which would determine a signal-to-noise ratio of three at the baseline signal reading. Table 5 lists the calculated values which are all less than 50 μM. For detection of low sample concentration, the improvement of sensitivity by increasing optical path length comes with the cost of reduced transmitted power which results in an optimal channel width [129]. Since the LOD value, by definition, depends on the signal-to-noise ratio, improving the signal of the transmitted light detected thus provides a lower LOD value. For the devices

employing straight waveguides, the transmitted optical power for longer microchannel width is smaller than the short microchannel width because of increased coupling loss [130]. The coupling loss increases due to the amount of unguided light increases and resulted in a lower amount of light being collected at the opposite waveguide. Thus the signal detected is lower for a wider microchannel. Albeit no direct referencing can be made with the LOD values reported in literature because of the differences in experimental setups for each integrated waveguide device, a rough comparison shows that the LOD values are approximately in the same range: 200 µM for a 50 µm path length [120], 6 µM for a 140 µm path length [131], and 3 µM for a 750 µm path length [119].

Based on Beer-Lambert's Law, a large gradient of calibration line means high sensitivity of the absorbance measurement. The gradient can be increased by increasing the optical path length by our proposed MTIR method in which input light was not incident normally onto the microfluidic channel but at an angle of 53° as shown in Figure 53. The MTIRs demand high reflectivity of PDMS-air interface. Figure 54 shows that the reflectivity of the PDMS-air interface is in the range of 80% to 90% when the incident angles is greater than 44.7° (the critical angle of the PDMS and air interface).

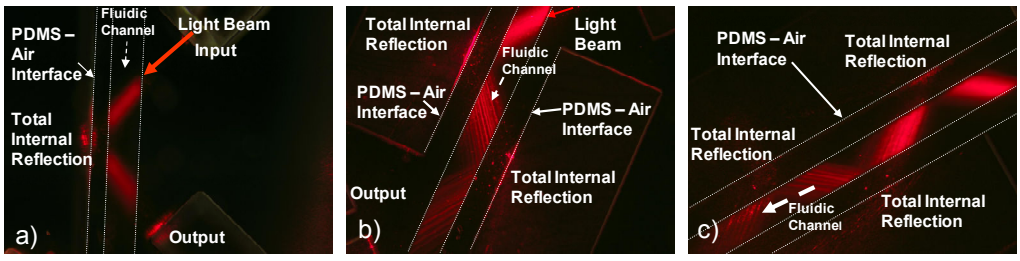

Figure 53: Microscope images of the MTIR with: a) 1, b) 2 and c) 4 reflections, respectively.

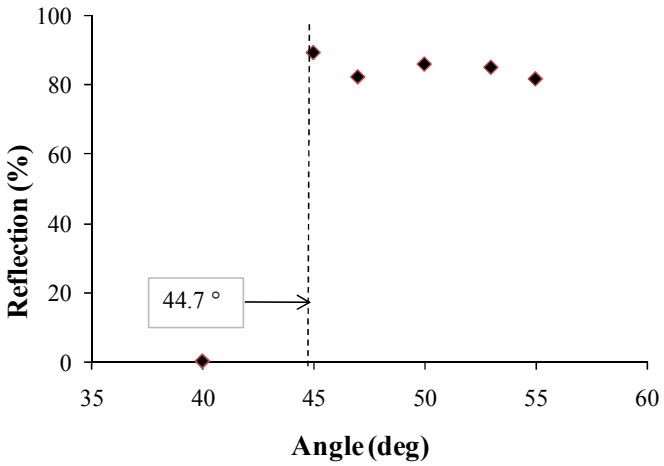

Figure 54: Reflectivity of PDMS-Air interface.

The calibration plots obtained using 'Brilliant Blue' solutions are given in Figure 55. A null intercept value can be assumed as most regression lines pass near origin. The calibration plots show linear trend with optical path length and relative sensitivity listed in Table 6. The gradient of the plots increases as the number of reflections increases. Table 6 summarizes that an 18-fold increase in detection sensitivity was accomplished with the four TIRs as compared with the single TIR.

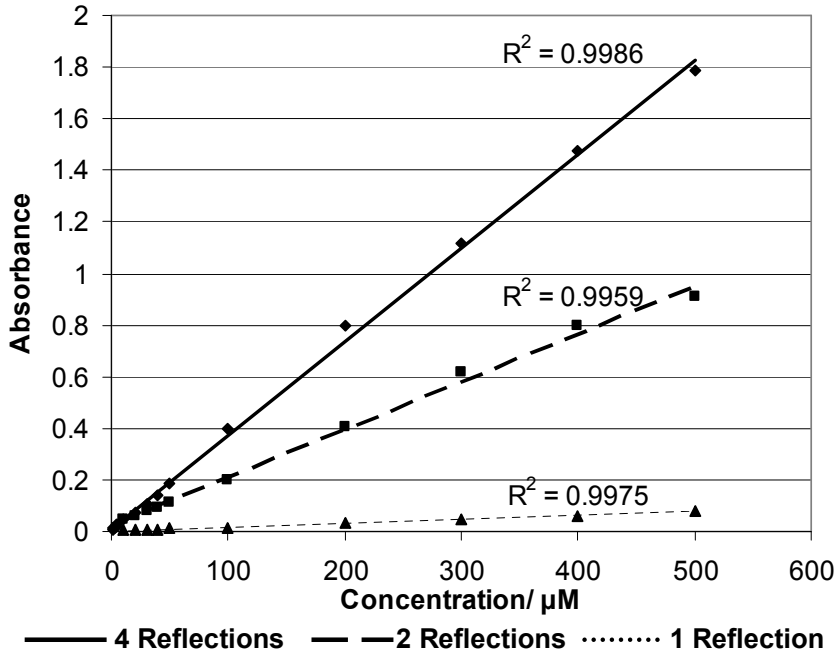

Figure 55: Calibration plots of 'Brilliant Blue' solutions for the MTIR.

Number of TIR	Optical Path-length (μm)	Relative Sensitivity (slope)
1	750	1
2	1125	9
4	1875	18

Table 6: Comparison of Absorbance Measurements for 1, 2 and 4 Total Internal Reflection.

5.4.2 Evanescent field absorption spectroscopy with single-mode waveguide

The fabricated PDMS integrated single-mode waveguide with microfluidic is shown in Figure 56. As shown in Figure 56a, the microfluidic channel was properly aligned on top of the rib waveguide. The cross sectional image of the successful integration of microfluidic channel with rib waveguide is shown in Figure 56b. The microfluidic channel has a cross sectional area of 130 μm × 130 μm and the rib waveguide is 8 μm high and 7 μm wide.

The light confinement in the rib waveguide can be observed from the image. At the core-cladding surface, the evanescent field decays exponentially with the distance from the waveguide surface.

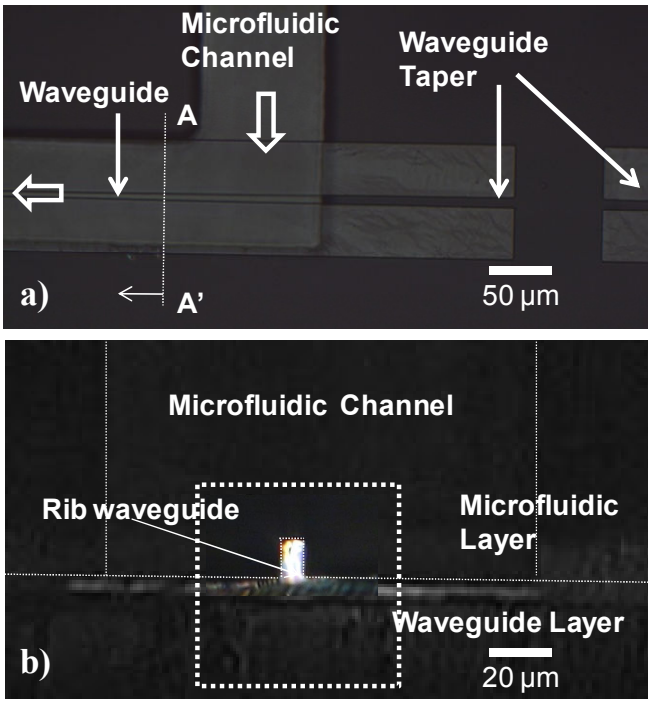

Figure 56: The microscope images of the integrated microfluidic and waveguide layer. a) The top view of the integrated single-mode rib waveguide with the microfluidic channel; b) the cross section image at the line AA' of (a) with the single-mode rib waveguide illuminated with a white light source.

The penetration depth d_p, which is defined as the distance where evanescent field decreases to $1/e$, can be estimated by the formula [132],

$$d_p = \frac{\lambda}{2\pi\sqrt{n_{eff} - n_c}} \tag{82}$$

where λ is the wavelength of light, n_{eff} is the effective index of the waveguide and n_c is the cladding refractive index (i.e. the analyte refractive index in this case). For a PDMS single-mode rib waveguide operating at a 650 nm wavelength with water as cover cladding, the penetration depth is more than 470 nm, which is highly suitable for sensing even large biomolecules up to hundreds of nanometers in length.

The achievability of the fabricated PDMS chip for evanescent absorption spectroscopy was first confirmed by measuring the absorption spectra of both fluorescein and bromophenol blue. The absorption peaks of fluorescein and bromophenol blue are at 490 nm and 590 nm, respectively. Figure 57a shows the absorption peaks for both of the analytes. The absorption measurement was further performed for various concentrations of bromophenol blue and is shown in Figure 57b. The minimum concentration detected by the single-mode evanescent field is 0.1 μM. Bromophenol blue is a polar molecule and has a pH dependent spectra characteristic. The bromophenol blue was prepared with ultra pure water to maintain the pH dependency of the spectra characteristic as well as controlling the non-linearity of the pH dependent absorption of the solute on the surface.

An oligonucleotide is a single stranded molecule that can be used as biological recognition element. The base sequence in the oligonucleotide can be employed for hybridization of double stranded molecule. Hence, the oligonucleotide can be used as a gene probe base test to any complementary sequence of interest [133]. The successful immobilization of the fluorescently tagged oligonucleotide used in the experiments was confirmed by the fluorescent microscope images (Figure 58). A microfluidic channel with no chemical surface functionalized treatment was used as a reference waveguide. The reference waveguide does not show fluorescence while the sensor waveguide shows a strong fluorescent signal of the Cy5 labelled oligonucleotide. The absorption spectroscopy of the oligonucleotide is shown in Figure 59.

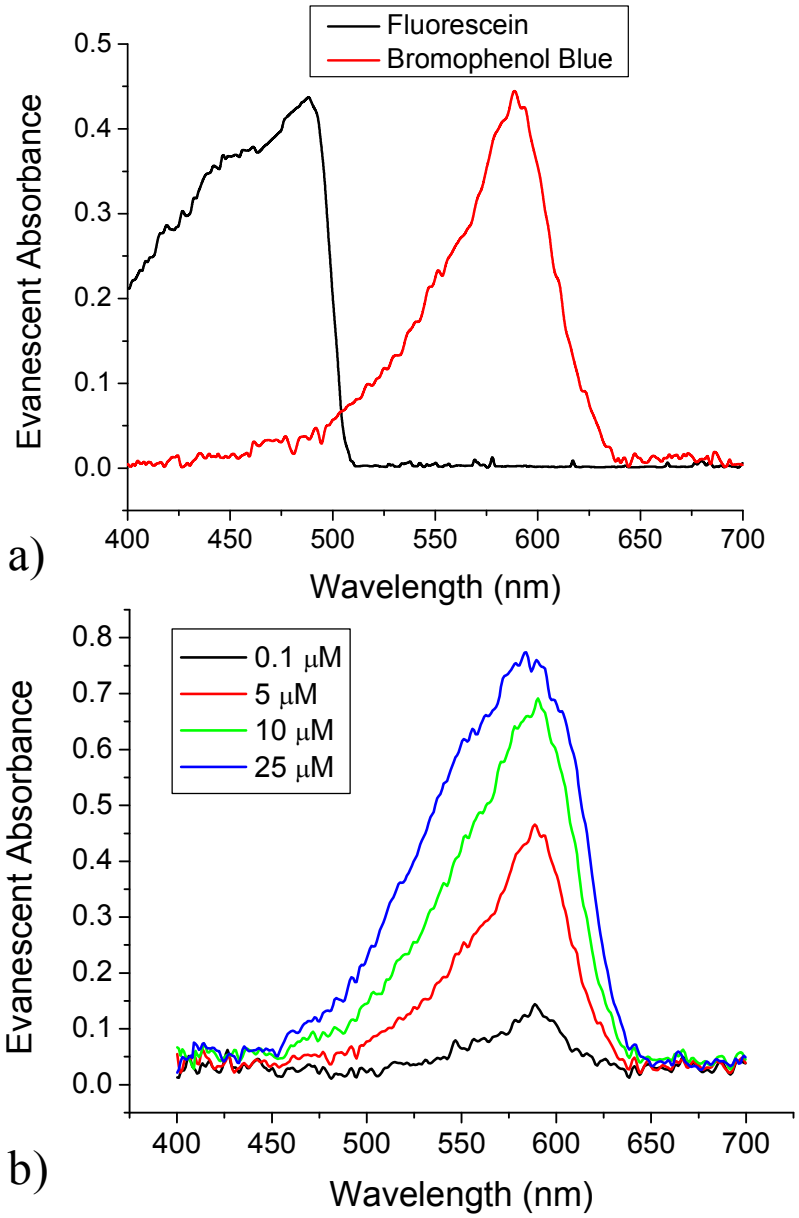

Figure 57: Evanescent field absorption spectra. (a) Fluorescein and bromophenol blue (b) Various concentrations of bromophenol blue.

From the spectra, the strong absorption peak of the Cy5 excitation can be observed at the 650 nm wavelength. As the biotin, streptavidin and oligonucleotide have no absorption in the visible light range; only the Cy5 dye can be detected and shown in the graph.

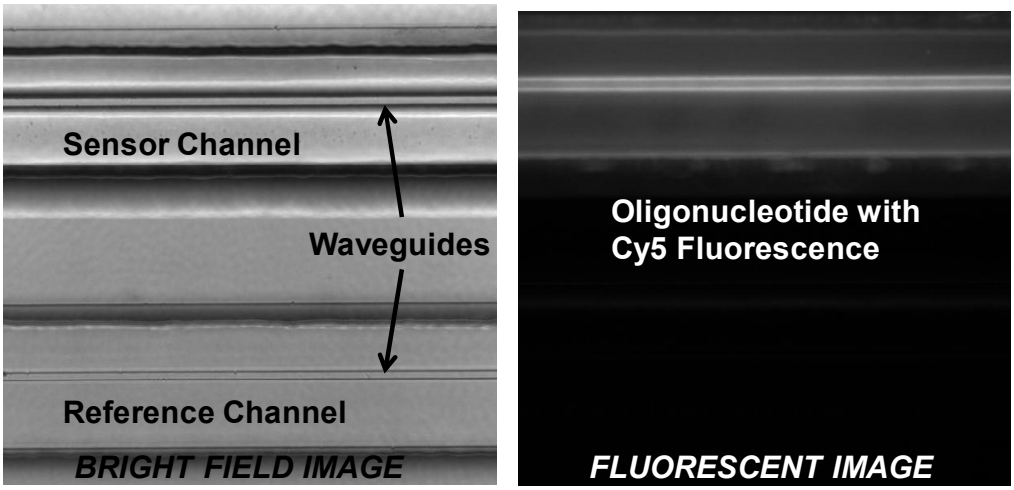

Figure 58: Microscope images of integrated PDMS waveguide with microfluidic for verification of successful immobilization of oligonucleotide.

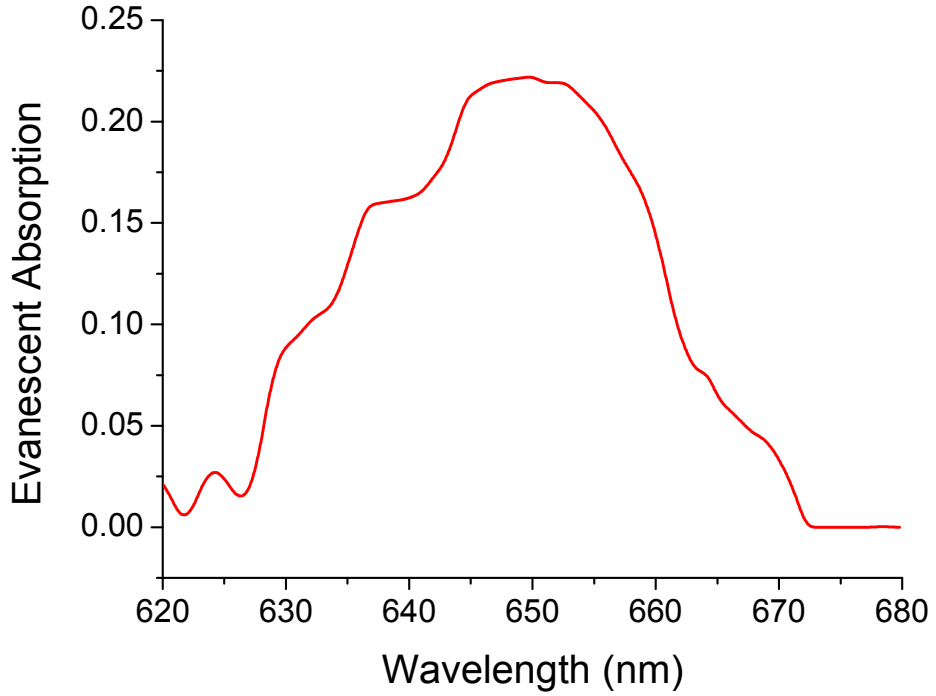

Figure 59: Absorption spectra of the oligonucleotide labeled with Cy5 fluorescent dye.

In this chapter, the performance of an integrated PDMS waveguide with microfluidics as a component of LOC microspectrometer was investigated. Different schemes of integration were proposed for multi-mode and single-mode waveguides to solve the respective issues.

The multi-mode waveguide was integrated by perpendicular arrangement of both waveguide and microfluidics for the absorbance measurement of Fluorescein. For 500 μm width microfluidic channel integrated with straight waveguide, the LOD was 9.9 μM with sensitivity of 1.14 $\times 10^{-3}$ AU/μM. The sensitivity was increased with a curved waveguide scheme to 2.36 $\times 10^{-3}$ AU/μM by reducing the stray light in the device. To further improves the sensitivity which is limited by the inherently short optical path-length as the device shrinks, multi-total internal reflection (MTIR) scheme was proposed and realized in PDMS microfluidic channel. At an incident angle greater than the critical angle of 44.7˚, total internal reflection occurs naturally in PDMS-air interface without additional metal coating. Up to 4 times of MTIR was demonstrated in the PDMS microfluidic channel and increased the sensitivity by 18 times.

The evanescent field absorption spectroscopy on a PDMS single-mode waveguide was proposed and demonstrated to circumvent the large diffraction loss as the light traverse across the channel in the direct integration of PDMS single-mode waveguide with microfluidics. Bromophenol blue was detected to a minimum concentration of 0.1 μM. Further evanescent field absorption spectroscopy was performed on oligonucleotide immobilized on the PDMS waveguide. Surface modification for the immobilization of oligonucleotide on the waveguide is presented and implemented for evanescent field absorption

spectroscopy. Evanescent field absorption spectroscopy on single-mode rib waveguide is useful for investigation of surface-associated chemistry in immunoassay and cell-based assay.

CHAPTER 6

CONCLUSIONS

6.1 Conclusions

The aims of this thesis were to achieve a compact microspectrometer LOC system with increased functionality at low cost for absorption spectroscopy applications. The low cost is achieved by implementing the disposable biochip using PDMS, a material of choice for microfluidics. For such a desired PDMS microspectrometer, the PDMS optical microcomponents for both wavelength discrimination and sensing are necessary to accomplish the specification required. Furthermore, the feasibility of integrating PDMS microoptical components together with the microfluidic system is highly essential. In this thesis, the PDMS waveguide has been investigated as a basic building block for the construction of arrayed waveguide gratings for wavelength discrimination – key component in a microspectrometer as well as the integration with microfluidic for effective biochemical sensing.

In this thesis, single-mode and multi-mode PDMS rib waveguides have been designed, fabricated and characterized. By selecting the appropriate geometrical parameters, single-mode propagation can be generated even in a large cross section PDMS rib waveguide (> 5 μm). Thus, single-mode PDMS rib waveguides was demonstrated for the first-time for building complex microphotonics devices such as Y-branch splitter and AWG. The fabrication process of single-mode PDMS rib waveguide was precisely controlled to produce the desired slab height and rib height to the accuracy of ±0.1 μm. Two steps curing process were performed to create the core and cladding layer of the

PDMS waveguide with SU-8 photoresist as master mold. Blading process and delicate spin coating step were used for the formation of the core layer to the desired thickness for the slab height. In addition, the modifications of the refractive index contrast Δ of the PDMS were proposed with three methods; silicone oil dilution, hexane dilution or employing PDMS material from two commercially available sources and vary from 1.408 to 1.429. The propagation loss of the single-mode waveguide measured at the wavelength of 635 nm was 0.48 dB/cm for low refractive index contrast waveguides (Δ=0.07%) and 0.2 dB/cm for high refractive index contrast waveguides (Δ=1.18%). For multi-mode waveguide, the propagation loss was measured to be 0.25 dB/cm. Transition loss of 1 dB was demonstrated for bending radius of 0.8 cm and radiation loss of 1 dB for bending radius of 0.4 cm.

Based on the proven single-mode PDMS rib waveguides, PDMS AWG was designed, fabricated and characterized for the implementation of microspectrometer's wavelength discrimination element. Two types of PDMS AWG were designed to meet the requirements of high resolution (~1nm) and large *FSR* (>300 nm) for a microspectrometer. The first conventional PDMS AWG has been designed with a resolution as high as 1 nm. The second non-conventional PDMS AWG with an S-shaped arrayed waveguides has been realized with large *FSR* of 275 nm. The fabrication-related error studies on the conventional PDMS AWG had shown high tolerance for refractive index contrast Δ variation up to 10% and sidewall slope angle of 2˚. The fabrication precision of the slab and rib heights with a uniformity of ± 0.1 μm was essential in ensuring a practical transmission spectrum very close to the simulated one. The measured transmission loss of the conventional PDMS AWG has shown an

insertion loss of 11.4 dB at 641 nm transmission peak and adjacent crosstalk of > 15dB with channel loss uniformity well within 0.6 dB. The polarization dependency of the transmission characteristic was measured to be around 0.01 nm which is caused by effective index fluctuation which resulted from the non-uniformities of the width and height of the rib waveguide and the inhomogeneity of the PDMS refractive index.

Lastly, the performance of PDMS waveguide integrated with microfluidics for LOC microspectrometer was investigated. Different schemes of integration were proposed for multi-mode and single-mode waveguides to solve the size-related issues of the waveguide. The multi-mode waveguide was integrated by perpendicular arrangement of both waveguide and microfluidic for the absorbance measurement of Fluorescein. For 500 μm width microfluidic channel integrated with straight waveguide, the LOD was 9.9 μM with a sensitivity 1.14 $\times 10^{-3}$ AU/μM. The sensitivity was increased with a curved waveguide scheme to 2.36 $\times 10^{-3}$ AU/μM by reducing the stray light in the device. To further improve the sensitivity which is limited by the inherently short optical path-length as the device shrinks, multi-total internal reflection (MTIR) was proposed and realized in PDMS microfluidic channel. At an incident angle greater than the critical angle of 44.7˚, total internal reflection occurs naturally in PDMS-air interface without additional metal coating. Up to 4 times of MTIR was demonstrated in the PDMS microfluidic channel and increased the sensitivity by 18 times. For smaller dimension single-mode waveguide, the evanescent field absorption spectroscopy on a PDMS single-mode waveguide was suggested and verified to circumvent the large diffraction loss as the light traverses across the channel in direct integration of waveguide

to microfluidic channel. The evanescent field sensing has shown that bromophenol blue could be detected to a minimum concentration at 0.1 μM. Further evanescent field absorption spectroscopy was performed on oligonucleotide immobilized on the PDMS waveguide. Surface modification for the immobilization of oligonucleotide on the waveguide was implemented for evanescent field absorption spectroscopy.

6.2 Future work

Both the conventional and S-shaped AWGs should be integrated in a cascaded configuration to tap on the advantages of both high resolution and large free spectral range. A broad band white light source can be used for the S-shaped AWG to produce a RGB output with 3 or more channels at the output that are then coupled to the conventional AWG. The conventional AWG further disperses and produces an output with a higher resolution.

As mentioned in chapter 2, many LOC microspectrometers have been demonstrated with various types of materials and different operation principles. Each type of microspectrometer has its own advantages and limitations. A Fabry Pèrot-based microspectrometer has high resolution but limited free spectral range while the Linear Variable Filter lacks high resolution. Although, a grating-based microspectrometer can overcome the free spectral range of a Fabry-Pèrot-based one, the limited optical path in available in a miniaturized realization puts a constraint on the resolution. The performance of our PDMS AWGs is comparable with that of the existing silica-on-silicon AWG microspectrometer. However, silicon-based microspectrometers are costly and require sophisticated fabrication technique. Table 7 summarizes the comparison

between the performances of the PDMS-based microspectrometer with existing microspectrometer in LOC system presented in chapter 2.

A conventional AWG can be designed to operate at high diffraction order to attain the high resolution needed for spectroscopy but this comes at the expense of the free spectral range. Hence, a non-conventional S-shaped AWG can be used to circumvent this problem by operating at a low diffraction order for large free spectral range. AWGs fabricated in PDMS offer the benefits of excellent optical properties in the visible light range and ease of integration with microfluidics.

Spectrometer Type	**Resolution**	**FSR**	**Material**	**Integration scheme**
Grating [14]	8.5 nm	N.A.	Silicon Grating on CCD device	Chip-to-chip
Fabry Pèrot Etalon [10]	6 nm	120 nm	Silicon-based Fabry-Pèrot Filter and photodetector. SU-8 microfluidic layer.	Chip-to-chip
Array Waveguide Grating [30]	12.5 nm	100 nm	Silica-on-silicon	Monolithically on silicon
Linear Variable Bandpass Filter [11]	N.A.	180 nm	A linear variable filter on top of 12 bit CMOS sensor	Chip-to-chip
Conventional PDMS AWG	1 nm	5 nm	PDMS	Monolithically in PDMS
S-shape PDMS AWG	80 nm	275 nm	PDMS	Monolithically in PDMS

Table 7: Comparison of the resolution, free spectral range, material (for cost evaluation) and integration scheme for various LOC microspectrometers.

Together with the rapid prototyping method by soft lithography, it enables large amounts of chips to be easily and quickly produced and used as disposable LOC analytical systems at a low cost.

The number of AWG output waveguides can be increased to 32 or 64 channel so that each AWG can cover a sufficient wavelength range for spectroscopy. Moreover, the output profile at the second FPR region can be designed to produce a flat focal point where direct integration of photodetector array can be implemented. The input coupling of light source to the waveguide is a strenuous task. Grating coupler can be integrated to allow easy coupling of light into waveguide for test and measurement.

Future work also includes the integration of AWG and microfluidics to demonstrate biochemical spectroscopy measurements to evaluate the performance of PDMS AWG microspectrometers for LOC. In addition, the integration of PDMS waveguide with microfluidic was examined for the application in absorption spectroscopy. The envisioned concept of such LOC microspectrometer is shown in Figure 60.

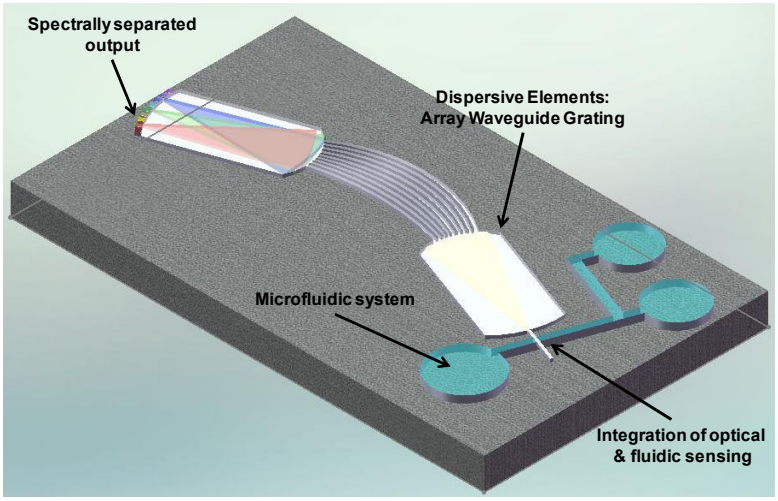

Figure 60: Conceptual drawing of an integrated PDMS microspectrometer for LOC.

AUTHOR PUBLICATIONS

LIST OF JOURNAL PUBLICATIONS

[1] J.S. Kee, D.P. Poenar, P. Neuzil, and L. Yobas, "Monolithic Integration of Poly(dimethylsiloxane) Waveguides and Microfluidics for On-Chip Absorbance Measurements," Sens. Actuators B 134, 532-538, 2008.

[2] J.S. Kee, D.P. Poenar, P. Neuzil, and L. Yobas, "Design and fabrication of Poly(dimethylsiloxane) single-mode rib waveguide," Optics Express 17, No. 14, pp. 11739-11746, 2009.

[3] D.P. Poenar, J.S. Kee, P. Neuzil, and L. Yobas, "The Design and Fabrication of Poly(dimethylsiloxane) Single Mode Rib Waveguides for Lab-on-a-chip Applications" Advanced Materials Research Vol. 74 pp 51-54, 2009.

[4] J.S. Kee, D.P. Poenar, P. Neuzil, and L. Yobas, Y. Chen "Design and fabrication of Poly(dimethylsiloxane) arrayed waveguide grating," Optics Express, Vol 18, No 21, pp. 21732-21742, 2010.

LIST OF CONFERENCE PUBLICATIONS

[1] J.S. Kee, D.P. Poenar, and L. Yobas, "Integrated Polydimethylsiloxane Waveguide for Optical Detection," *The 10th International Conference on Miniaturized Chemistry and Life Sciences, 2006, Japan*

[2] J.S. Kee, D.P. Poenar, P. Neuzil, and L. Yobas, "Multi-Total Internal Reflection in Polydimethylsiloxane Microfluidics for Enhanced Absorbance Detection," *The 11th International Conference on Miniaturized Chemistry and Life Sciences, 2007, France*

[3] J.S. Kee, D.P. Poenar, P. Neuzil, and L. Yobas, "Poly(dimethylsiloxane) Waveguides Integrated with Microfluidics for Absorbance Measurement," *IEEE Photonics Global Conference, 2008, Singapore*

[4] J.S. Kee, D.P. Poenar, P. Neuzil, and L. Yobas, "Evanescent Field Absorption Spectroscopy with Polydimethylsiloxane Single-mode Rib waveguide integrated with microfluidic," *The 14th International Conference on Miniaturized Chemistry and Life Sciences, 2010, The Netherlands.*

BIBLIOGRAPHY

[1] W. Schmidt, "Optical Spectroscopy in Chemistry and Life Sciences," Wiley-VCH Verlag GmbH & Co., Weinheim, (2005).

[2] J. Q. Brown, K. Vishwanath, G. M. Palmer and N. Ramanujam, "Advances in quantitative UV–visible spectroscopy for clinical and pre-clinical application in cancer," Current Opinion in Biotechnology, 20, 119-131, (2009).

[3] P. D. Tzanavaras and D. G. Themelis, "Review of recent application of flow injection spectrophotometery to pharmaceutical analysis," Anal. Chim. Acta, 588, 1-9, (2007).

[4] G. L. Cote´, "Noninvasive and Minimally-Invasive Optical Monitoring Technologies," J. Nutri., 131, 1596-1604, (2001).

[5] A. O. Beckman, W. S. Gallaway, W. Kaye, W. F. Ulrich, History of spectrophotometry at Beckman Instrument, Inc," Anal. Chem., 49, 280-300, (1977).

[6] H.H. Cary and A.O.Beckman, "A quartz photoelectric spectrophotometer," J. of Opt. Soc. of Am., 31, 681-689, (1941).

[7] C. P. Bacon, Y. Mattley, R. De Frecea, "Miniature spectroscopic instrumentation: Applications to biology and chemistry," Rev. Sci. Inst., 75, 1-16, (2004).

[8] http://www.oceanoptics.com

[9] R. F. Wolffenbuttel, "State-of-the-art in integrated optical microspectrometer," IEEE Trans. Instrum. Meas., 53, 197-202, (2004).

[10] R. F. Wolffenbuttel, "MEMS-based optical mini- and microspectrometers for the visible and infrared spectral range," J. Micromech. Microeng., 15, S145-S152, (2005).

[11] G. M. Yee, N. I. Maluf, P. A. Hing, M. Albin, and G. T. A. Kovacs, "Miniature spectrometers for biochemical analysis," Sens. Actuators A, 58,61-66, (1997).

[12] Z. H. Liang, N. Chiem, G. Ocvirk, T. Tang, K. Fluri and D. J. Harrison, "Microfabrication of a planar absorbance and fluorescence cell for integrated capillary electrophoresis devices," Anal. Chem., 68, 1040-1046, (1996).

[13] R. D. Reyes, D. Iossifidis, P. A. Auroux and A. Manz, "Micro Total Analysis Systems. 1. Introduction, Theory, and Technology," Anal. Chem., 2002, 74, 2623–2636

[14] E. Verpoorte, "Focus Chip Vision – optics for microchips," Lab Chip, 3, 42N - 52N, (2003).

[15] G. M. Whitesides, "The origins and future of microfluidics," Nature, 442, 368-373, (2006).

[16] J. C. McDonald, D. C. Duffy, J. R. Anderson, H. Wu, D. T. Chiu, O. J. A. Schueller, G. M. Whitesides, "Fabrication of microfluidic systems in poly(dimethylsiloxane)," Electrophoresis, 21, 27-40, 2000.

[17] J. M. K. Ng, I. Gitlin, A. D. Stroock, G. M. Whitesides, "Components for integrated poly(dimethylsiloxane) microfluidic systems," Electrophoresis, 23, 3461-3473, (2002).

[18] S. K. Sia and G. M. Whitesides, "Microfluidic devices fabricated in poly(dimethylsiloxane) for biological studies," Electrophoresis, 24, 3563-3576, (2003).

[19] S. Camou, H. Fujita, T. Fujii, "PDMS 2D optical lens integrated with microfluidic channels: principle and characterization," Lab Chip, 3, 40–45 (2003).

[20] K. Hosokawa, K. Hanada, R. Maeda, "A polydimethylsiloxane (PDMS) deformable diffraction grating for monitoring of local pressure in microfluidic devices," J. Micromech. Microeng., 12, 1-6, (2002).

[21] A. Llobera, R.Wilke, S. Buttgenbach, "Poly(dimethylsiloxane) hollow Abbe prism with microlenses for detection based on absorption and refractive index shift," Lab Chip 4, 24–27 (2004).

[22] O. Hofmann, X. H. Wang, A Cornwell, B. Stephen, A. Raja, D. Bradley, A. deMello and J. deMello, "Monolithically integrated dye-doped PDMS long pass filters for disposable on-chip fluorescence detection," Lab Chip, 6, 981-987, (2006).

[23] Q. Kou, I. Yesilyurt, V. Studer, M. Belotti, E. Cambril, Y. Chen, "On-chip optical components and microfluidic systems," Microelectron. Eng., 73, 876–880 (2004).

[24] D. A. Chang-Yen, R. K. Eich, and B.K. Gale, "A monolithic PDMS waveguide system fabricated using soft-lithography techniques," IEEE J. Lightwave Technol. 6, 2088-2093 (2005).

[25] T. Vo-Dinh, "Basic Instrumentation in Photonics," Chapter 6, Biomedical Photonics Handbook, CRC Press, (2003).

[26] M. Born and E. wolf, Principle of Optics, Pergamon, (1995).

[27] Marcuse, D, 1974, Theory of Dielectric Optical Waveguide, New York, Academic Press.

[28] J. H. Jerman, D. J. Clift and S. R. Mallinson, "A miniature Fabry-Pèrot interferometer with a corrugated silicon diaphragm support," Sensors and Actuators, Vol. 29, pp. 151-158, (1991).

[29] N. F. Raley, D. R. Ciarlo, J. C. Koo, B. Beiriger, J. Truijillo, C. Yu, G. Loomis and R. Chow, "A Fabry-Pèrot Microinterferometer for visible wavelengths," IEEE Solid-State Sensor and Actuator Workshop, pp. 170-173, (1992).

[30] K. Aratani, P. J. French, P. M. Sarro, D. Poenar, R. F. Wolffenbuttel, and S. Middelhoek, "Surface micromachined tuneable interferometer array," Sensors and Actuators A, 43, 17-23, 1994.

[31] J. H. Correia, M. Bartek, R. F. Wolffenbuttel, "Bulk-micromachined tunable Fabry-Pèrot microinterferometer for the visible spectral range," Sensors and Actuators A, 76, 191-196, (1999)

[32] J. H. Correia, G. de Graaf, S. H. Kong, M. Bartek, R. F. Wolffenbuttel, "Single-chip CMOS optical microspectrometer," Sensors and Actuators A, 82, 191-197, (2000).

[33] J. H. Correia, M. Bartek, R. F. Wolffenbuttel, "High-Selectivity Single Chip Spectrometer in Silicon for Operation at Visible Part of the Spectrum," IEEE Trans. Elec. Devices, 47. No. 3 553-559, (2000).

[34] G. Minas, R. F. Wolffenbuttel, and J. H. Correia, "An array of highly selective Fabry-Pèrot optical channels for biological fluid analysis by optical absorption using white light source for illumination," J. Opt. A: Pure Appl. Opt., 8272-278, (2006).

[35] G. Minas, R. F. Wolffenbuttel and J. H. Correia, "A lab-on-a-chip for spectrophotometric analysis of biological fluids," Lab Chip, 5, 1303–1309, (2005).

[36] O. Schmidt, M. Bassler, P. Kiesel, C. Knollenberg, and N. Johnson, "Fluorescence spectrometer-on-a-fluidic-chip," Lab Chip, 7, 626-629, (2007).

[37] D. S. Goldman, P. L. White and N. C. Anheier, "Miniaturized spectrometer employing planar waveguides and grating couplers for chemical analysis," Applied Optics, 29, 4583-4589, (1990).

[38] T. A. Kwa, and R. F. Wolffenbuttel, "Integrated grating/detector array fabricated in silicon using micromachining techniques," Sensors and Actuators A, 31, 259-266, (1992).

[39] G. M. Yee, N. I. Maluf, P. A. Hing, M. Albin, G. T. A. Kovacs, "Miniature spectrometers for biochemical analysis," Sensors and Actuators A, 58, 61-66, (1997).

[40] I. Avrutsky,K. Chaganti, I. Salakhutdinov, G. Auner, "Concept of a miniature optical spectrometer using integrated optical and micro-optical components," Applied Optics, 7811-7817, (2006).

[41] J. Mohr, B. Anderer, and W. Ehrfeld, "Fabrication of a planar grating spectrograph by deep etch lithography with synchrotron radiation," Sensors and Actuators A, 25-27, 571-575, (1991).

[42] D. Sander, O. Blume and J. Muller, "Microspectrometer with slab-waveguide transmission gratings," Applied Optics, 35, 21, 4096-4101, (1996).

[43] D. Sander, and J. Muller, "Selffocussing phase transmission grating for an integrated optical microspectrometer," Sensors and Actuators A, 88, 1-9, (2001).

[44] R. F. Wolffenbuttel, "State-of-the-art in integrated optical microspectrometers," IEEE Trans. Instrum. Meas., 53, 197-202, (2004).

[45] S. Grabanik, R. F. Wolffenbuttel, A. Emadi, M. Loktev, E. Sokolova, and G. Vdovin, "Planar double grating microspectrometer," Optic Express, 15, 3581, (2007).

[46] M. K. Smit, "New Focusing and Dispersive Planar Component based on an optical Phased Array," Electronics Letters, 24. 7, (1988).

[47] C. Dragone, "An N × N optical multiplexer using a planar arrangement of two star couplers," IEEE Photon. Technol. Lett., 3, 812, (1991).

[48] H. Takahashi, K. Oda, H. toba, and Y. Inoue, J. Lightwave Techn., 13, 447, (1995).

[49] K. Okamoto, K. Syuto, H. Takahashi, and Y. Ohmori, Electron. Lett. , 32, 1474, (1996).

[50] Y. Hibino, " ," IEEE J. Sel. Topics Quantum Electron. 8, 1090, (2002).

[51] P. Cheben, I. Powell, S. Janz, and D. X. Xu, "Wavelength-dispersive device based on a Fourier-transform Michelson-type array waveguide grating," Optics Letter, 30, 1824-1826, (2005).

[52] Y. Komai, H. Nagano, K. Kodate, K. Okamoto, and T. Kamiya, "Application of Arrayed-Waveguide Grating to Compact Spectroscopic Sensors," Japanese Journal of Applied Physics, 43, 5795–5799, (2004).

[53] K. Suzuki, Y. Hida, T. Shibata, Y. Inoue, H. Takahashi, and K. Okamoto, "Silica-based Arrayed-waveguide Gratings for the visible wavelength range," NTT Review, 6, 48-52, (2006).

[54] Y. Komai , H. Nagano, K. Okamoto and K. Kodate, “Compact Spectroscopic Sensor Using a Visible Arrayed Waveguide Grating,” Japanese Journal of Applied Physics, 45, 6742–6749, (2006).

[55] K. Kodate and Y. Komai, “Compact Spectroscopic sensor using an array waveguide grating,” Journal of Optics A:Pure Appl. Opt., 10, 044011, (2008).

[56] T. N. Woods, R. T. Wrigley III, G. J. Rottman, and R. E. Haring, "Scattered-light properties of diffraction gratings," Appl. Opt. 33, 4273-4285 (1994)

[57] M.A. Ordal, “Optical properties of the metals Al, Co, Cu, Au, Fe, Pb, Ni, Pd, Pt, Ag, Ti and W in the infrared and far infrared,” Appl. Opt., 22, 7, 1099-1119, (1983).

[58] H. A. Macleod, “Thin-film Optical Filters,” U.K. Adam Hilger, (1986).

[59] K. B. Mogensen, J. El-Ali, A. Wolff, J. P. Kutter, “Integration of Polymer Waveguides for Optical Detection in Microfabricated Chemical Analysis Systems,” Ap. Opt., 42, 4072-4078, (2003).

[60] P.V. Lambeck, “Integrated optical sensors for the chemical domain,” Meas. Sci. Technol., 17, 93-116 (2006).

[61] K. B. Mogensen, N. J. Petersen, J. Hubner and J. P. Kutter, “Monolithic integration of optical waveguides for absorbance detection in microfabricated electrophoresis devices,” Electrophoresis, 22, 3930-3938, (2001).

[62] N. J. Petersen, K. B. Mogensen, J.P. Kutter, “Performance of an in-plane detection cell with integrated waveguides for UV/Vis absorbance measurements on microfluidic separation devices,” Electrophoresis, 23, 3528-3536, (2002).

[63] K. B. Mogensen, J. El-Ali, A. Wolff, J. P. Kutter, "Integration of polymer waveguides for optical detection in microfabricated chemical analysis systems," Appl. Optics , 42, 4072-4079, (2003).

[64] D. A. Chang-Yen and Bruce K. Gale, "An integrated optical oxygen sensor fabricated using rapid-prototyping techniques," Lab Chip, 3, 297-301, (2003).

[65] J. M. Ruano-Lopez, M. Aguirregabiria, M. Tijero, M. T. Arroyo, J. Elizalde, J. Berganzo, I. Aranburu, F. J. Blanco and K. Mayora, "A new SU-8 process to integrate buried waveguides and sealed microchannels for a Lab-on-a-Chip," Sensors and Actuators B, 114, 542-551, (2006).

[66] S. K. Sia and G. M. Whitesides, "Microfluidic devices fabricated in poly(dimethylsiloxane) for biological studies," Electrophoresis, 24, 3563-3576, (2003).

[67] F. Schneider, J. Draheim, R. Kamberger, and U. Wallrabe, "Process and material properties of polydimethylsiloxane (PDMS) for Optical MEMS," Sens. & Actuators A, 151, 95-99, (2009).

[68] Y. Xia and G. M. Whitesides, "Soft Lithography," Annu. Rev. Mater. Sci., 28, 153-184, (1998).

[69] Q. Kou, I. Yesilyurt, V. Studer, M. Belotti, E. Cambril and Y. Chen, "On-chip optical components and microfluidic systems," Microelectronics Engineering, 73, 876-880, (2004).

[70] S. Camou, H. Fujita and T. Fujii, "PDMS 2D optical lens integrated with microfluidic channels: principle and characterization," Lab Chip, 3, 40-45, (2003).

[71] O. Hofmann, X. Wang, A. Cornwell, S. Beecher, A. Raja, D. D. C. Bradley, A. J. deMello and J. C. deMello, "Monolithically integrated dye-doped

PDMS long-pass filters for disposable on-chip fluorescence detection," Lab Chip, 6, 981-987, (2006).

[72] D. A. Chang-Yen, R. K. Eich, and B.K. Gale, "A monolithic PDMS waveguide system fabricated using soft-lithography techniques," J. Lightwave Technology, 6, 2088-2093, (2005).

[73] B. G. Splawn and F. E. Lytle, "On-chip absorption measurements using an integrated waveguide," Anal. Bioanal. Chem., 373, 519-525, (2002).

[74] D. B. Wolfe, R. S. Conroy, P. Garstecki, B. T. Mayers, M. A. Fischbach, K. E. Paul, M. Prentiss, and G. M. Whitesides, "Dynamic control of liquid-core/liquid-cladding optical waveguides," Proc. Nat. Acad. Sci. U. S. A. , 101, 12434-12438, (2004).

[75] A. Ymeti, J. Greve, P.V. Lambeck, T. Wink, S.W.F.M. van Hövell, T.A.M. Beumer, R.R. Wijn, R.G.. Heideman, V. Subramaniam, J.S. Kanger, "Fast, ultrasensitive virus detection using a Young interferometer sensor," Nano Lett. 7, 394-397 (2007).

[76] K. B. Mogensen and J. P Kutter, "Optical detection in microfluidic systems," Electrophoresis, 30, S92-S100, (2009).

[77] S. Kopetz, D. Cai, E. Rabe, and A. Neyer, "PDMS-based optical waveguide layer for integration in electricaloptical circuit boards," Int. J. Electron. Commun., 61, 163–167 (2007).

[78] D. Gallager, "Photonic CAD Matures," IEEE LEOS, 8, (2008).

[79] R. A. Soref, J. Schmidtchen, and K. Petermann, "Large Single-Mode Rib Waveguides in GeSi-Si and Si-on-SiO2," IEEE Journal of Quantum Electronics, 27, 8, (1991).

[80] S. P. Pogossian, L. Vescan, and A. Vonsovici, "The Single-Mode Condition for Semiconductor Rib Waveguides with Large Cross Section," IEEE Journal of Lightwave Technology, 16, 10, (1998).

[81] J. Lousteau, D. Furniss, A. B. Seddon, T. M. Benson, A. Vukovic, and P. Sewell, "The Single-Mode Condition for Silicon-on-Insulator Optical Rib Waveguides with Large Cross Section," IEEE Journal of Lightwave Technology, 22, 8, 1923-1929, (2004).

[82] S. P. Chan, C. E. Png, S. T. Lim, G. T. Reed, and V. M. N. Passaro, "Single-Mode and Polarization-Independent Silicon-on-Insulator Waveguides with Small Cross Section," IEEE Journal of Lightwave Technology, 23, 2103-2111, (2005).

[83] Nano™ SU-8 2000 Datasheet, *Microchem*

[84] K. S. Ryu, X. Wang, K. Shaikh, and C. Liu, "A Method for Precision Patterning of Silicone Elastomer and Its Applications," IEEE J. Microelectromech Syst., 13, 568-575 (2004).

[85] L. Novak, P. Neuzil, J. Pipper, Y. Zhang and S. Lee, "An integrated fluorescence detection system for lab-on-a-chip," Lab Chip, 7, 27-29, (2007).

[86] F. P. Payne and J. P. R. Lacey, "A theoretical analysis of scattering loss from planar optical waveguides," Opt. Quantum Electron., 26, 977-986 (1994).

[87] F. Ladouceur, "Roughness, Inhomogeneity, and Integrated Optics," IEEE J. Lightwave Technol., 15, 1020-1025 (1997).

[88] M. Diemeer, L.Hilderink, R. Dekker, and A.Driessen, "Low-cost and low-loss multimode waveguides of photodefinable epoxy," IEEE Photonics Tech. Elec. Lett., 18, 1624-1626, (2006).

[89] K. B. Mogensen, J. El-Ali, A. Wolff, J. P. Kutter, "Integration of polymer waveguides for optical detection in microfabricated chemical analysis systems," Appl. Optics, 42, 4072-4079, (2003).

[90] K. B. Mogensen, F. Eriksson, O. Gustafsson, R. P. H. Nikolajsen, and J. P. Kutter, "Pure-silica optical waveguides, fiber couplers, and high-aspect ratio submicrometer channels for electrokinetic separation devices," Electrophoresis, 25, 3788-3795, (2004).

[91] D. A. Chang-Yen, R. K. Eich, and B.K. Gale, "A monolithic PDMS waveguide system fabricated using soft-lithography techniques," J. of Lightwave Technology, 6, 2088-2093, (2005).

[92] I. Papakonstantinou, K. Wang, D. R. Selviah, and F. A. Fernandez, "Transition, radiation and propagation loss in polymer multimode waveguide bends," Optics Express, 15, 669-679, (2007).

[93] V. Subramaniam, G. N. De Brabander, D. H. Naghski and J. T. Boyd, "Measurement of mode field profiles and bending and transition losses in curved optical channel waveguides," J. of Lightwave Tech., 15, 990-997, (1997).

[94] B. Howley, X. Wang, R. T. Chen, and Y.Chen, "Experimental evaluation of curved polymer waveguides with air trenches and offsets," J. Appl. Phys., 100, 023114, (2006).

[95] M. K. Smit, "New focusing and dispersive component based on optical phased array," Electronics Letter, Vol. 24. pp. 385-386, 1988.

[96] H. Takahashi, S. Suzuki, K. Kato, and I. Nishi, "Arrayed-waveguide grating for wavelength division multi/demultiplexer with nanometer resolution," Electron. Lett. **26**, 87–88 (1990).

[3] Y. Hibino, "Recent Advances in High-Density and Large-Scale AWG Multi/Demultiplexers with Higher Inder-Contrast Silica-Based PLCs," IEEE Journal of Selected Topics in Quantum Electronics, Vol. 8, No. 6, pp. 1090-1101, 2002.

[98] H. Sanjoh, H. Yasaka, Y. Sakai, K. Sato, H. Ishii, and Y. Yoshikuni, "Multiwavelength light source with precise frequency spacing using a mode-locked semiconductor laser and an array waveguide grating," IEEE Photon. Technology Letter, vol. 9, pp. 818-820, June 1997.

[99] M. C. Parker and S. D. Walker, "Design of array-waveguide gratings using Fourier-Fresnel transform techniques," IEEE Journal of Selected Topics in Quantum Electronics, vol. 5, pp. 1379-1384, 1999.

[100] K. A. McGreer, "Array waveguide gratings for wavelength routing," IEEE Communication Magazine, Vol. 36, pp. 62-68, 1998.

[101] P. Cheben, J.H. Schmid, A. Delage, A Densmore, S. Janz, B. Lamontagne, J. Lapointe, E. Post, P. Waldron, and D.X. Xu, "A high resolution silicon-on-insulator arrayed waveguide grating microspectrometer with submicrometer aperture waveguides," Opt. Express, 15, 2299-2306 (2007).

[102] K. Okamoto, K. Moriwaki, S. Suzuki, "Fabrication of 64 × 64 arrayed waveguide grating multiplexer on Silicon," Electron. Lett., 31, 184-185 (1995).

[103] M. Diemeer, L. Spiekman, R. Ramsamoedj, and M.K. Smit, "Polymeric phased array wavelength multiplexer operating around 1550 nm," Electron. Lett., 32, 1132-1133 (1996).

[104] K. Kodate, Y. Komai, "Compact spectroscopic sensor using an arrayed waveguide grating," J. Opt. A:Pure Appl. Opt., 10, 044011-044018 (2008).

[105] H. Ma, A. K-Y. Jen, and L. R. Dalton, "Polymer-Based Optical Waveguides: Materials, Processing, and Devices," Adv. Mat., 14, 1339-1365 (2002).

[106] P. Cheben, "Wavelength dispersive planar waveguide devices: Echelle gratings and arrayed waveguide gratings," *Optical Waveguides: From Theory to Applied Technologies*, Chapter 5, Taylor & Francis, London (2007).

[107] M. K. Smit, "PHASAR-Based WDM-Devices: Principles, Design and Applications," IEEE J. Sel. Top. Quantum Electron. 2, 236-249 (1996).

[108] K. Okamoto, *Fundamental of Optical Waveguides*, (Academic Press, 2006), Chap. 9.

[109] R. Adar, C. H. Henry, C. Dragone, R. C. Kistler, and M. A. Milbrodt, "Broad-band Array Multiplexers Made with Silica Waveguides on Silicon," Journal of Lightwave Technology, 11, 212-219, (1993).

[110] K. Suzuki, Y. Hida, T. Shibata, Y. Inoue, H. Takahashi, and K. Okamoto, "Silica-based Arrayed-waveguide Gratings for the visible wavelength range," NTT Review, 6, 48-52, (2006).

[111] L. Vivien, S. Laval, B. Dumont, S. Lardenois, A. Koster, and E. Cassan, "Polarization-indepenedent single-mode rib waveguides on silicon-on-insulator for telecommunication wavelengths," Opt. Communication, 210, 43-49, (2002).

[112] C. R. Doerr and K. Okamoto, *Optical Fiber Telecommunications V A:Components and Subsystems*, (Elsevier Inc., 2008) , Chap. 9.

[113] K. Okamoto, and A. Sugita, "Flat spectral response arrayed-waveguide grating multiplexer with parabolic waveguide horns," *Electron. Lett.*, 32, 1661-1662, (1996).

[114] K. Okamoto, and H. Yamada, "Arrayed-waveguide grating multiplexer with flat spectral response," *Opt. Lett.* , 20, 43-45, (1995).

[115] K.B. Mogensen, H. Klank, J. P. Kutter, "Recent developments in detection for microfluidic systems," Electrophoresis, vol. 25, pp. 3498-3512, 2004.

[116] K. Swiney and D. J. Bornhop, "Detection in capillary electrophoresis," *Electrophoresis*, vol. 21, pp. 1239-1250, 2000.

[117] E. Verpoorte, "Chip vision-optics for microchips," Lab Chip, vol 3, pp. 42N-52N. 240, (2003).

[118] J. C. Roulet, R. Volkel, H.P. Herzig, E. Verpoorte, N. F. De Rooij and R. Dandliker, "Performance of an integrated microoptical system for fluorescence detection in microfluidic systems," Anal. Chem. , vol 74, 3400-3407, 2002.

[119] K. B. Mogensen, N. J. Petersen, J. Hubner and J. P. Kutter, "Monolithic integration of optical waveguides for absorbance detection in microfabricated electrophoresis devices," Electrophoresis, vol 22, pp. 3930-3938, 2001.

[120] B. G. Splawn and F. E. Lytle, "On-chip absorption measurements using an integrated waveguide," *Anal. Bioanal. Chem*., vol 373, pp. 519-525, 2002.

[121] D. B. Wolfe, R. S. Conroy, P. Garstecki, B. T. Mayers, M. A. Fischbach, K. E. Paul, M. Prentiss, and G. M. Whitesides, "Dynamic control of liquid-core/liquid-cladding optical waveguides," Proc. Nat. Acad. Sci. U. S. A. , vol 101, pp. 12434-12438, 2004.

[122] S. Götz, U. Karst, "Recent developments in optical detection methods for microchip separations," Anal. Bioanal. Chem., Vol. 387, pp. 183-192, 2007

[123] B. Kuswandi, Nuriman, J. Huskens, W. Verboom, "Optical Sensing Systems for Microfluidic Devices: A Review," Analytica Chimica Acta, Vol. 601, pp. 141-155, 2007

[124] N. J. Petersen, K. B. Mogensen, J. P. Kutter, "Performance of an in-plane detection cell with integrated waveguides for UV/Vis absorbance measurements on microfluidic separation devices," *Electrophoresis*, Vol. 23, pp. 3528, 2002

[125] E. Verpoorte, A. Manz, H. Ludi, A.E. Bruno, F. Maystre, B. Krattiger, H.M. Widmer, B.H. van der Schoot and N. F. Rooij A, "Silicon Flow Cell for Optical Detection in a Miniaturised Total Chemical Analysis Systems,", Sensors and Actuators, **6**, pp. 66-70, 1992.

[126] H. Salimi-Moosavi, Y. Jiang, L. Lestniers, G. McKinnon and D.J. Harrison, "A multireflection cell for enhanced absorbance detection in microchip-based capillary electrophoresis," Electrophoresis, Vol. 21 , 1291, 2000.

[127] G. Pandraud, T. M. Koster, C. Gui, M. Dijkstra, A. van den Berg and P. V. Lambeck, "Evanescent wave sensing: new features for detection in small volumes," Sens. Actuators A, Vol. 85, pp. 158, 2000.

[128] L. Novak, P. Neuzil, J. Pipper, Y. Zhang and S. Lee, "An integrated fluorescence detection system for lab-on-a-chip," *Lab Chip,* 7, pp. 27-29 2007.

[129] D. Snakenborg. K. B. Mogensen, J. P. kutter, "Optimization of signal-to-noise ratio in absorbance detection by integration of microoptical components," μTAS, pp. 841-844, 2003.

[130] K. B. Mogensen, J. El-Ali, A. Wolff, J. P. Kutter, "Integration of polymer waveguides for optical detection in microfabricated chemical analysis systems," *Appl. Optics* , vol 42, pp. 4072-4079, 2003.

[131] Z. H. Liang, N. Chiem, G. Ocvirk, T. Tang, K. Fluri and D. J.Harrison, "Microfabrication of a planar absorbance and fluorescence cell for integrated capillary electrophoresis devices," *Anal. Chem*. vol 68, pp. 1040-1046, 1996.

[132] J. T. Bradshaw, S. B. Mendes, S. S. Saavedra, "Planar integrated optical waveguide spectroscopy," Anal. Chem., 29-36, (2005).

[133] Hames, B.D., Higgings, S. J., *IRL Press*, Oxford, U.K. 1985